題目(和文)	
Title(English)	Exploration of new iron pnictide superconductors utilizing high pressure synthesis
著者(和文)	村場善行
Author(English)	Yoshinori Muraba
出典(和文)	学位:博士(工学), 学位授与機関:東京工業大学, 報告番号:甲第9505号, 授与年月日:2014年3月26日, 学位の種別:課程博士, 審査員:細野　秀雄,阿藤　敏行,須崎　友文,平松　秀典,松石　聡
Citation(English)	Degree:Doctor (Engineering), Conferring organization: Tokyo Institute of Technology, Report number:甲第9505号, Conferred date:2014/3/26, Degree Type:Course doctor, Examiner:,,,,
学位種別(和文)	博士論文
Type(English)	Doctoral Thesis

Exploration of new iron pnictide superconductors utilizing high pressure synthesis

Yoshinori Muraba

Department of Materials Science and Engineering
Interdisciplinary Graduate School of Science and Engineering
Tokyo Institute of Technology

2014

Contents

General introduction

High-pressure synthesis of the indirectly electron-doped 122 iron superconductor $Sr_{1-x}La_xFe_2As_2$ with a maximum T_c = 22 K

Hydrogen in layered iron arsenides: Indirect electron doping to induce superconductivity

Chapter 6 112

General conclusions

Chapter 1 General Introduction

1.1 Back ground of study

1.1.1 Histroy of superconductor

Figure 1-1 shows the history of representative superconductors and the development of the superconducting temperatures (T_c). Superconductivity was firstly discovered by Kamerlingh Onnes in 1911,[1] which was achieved in elemental Hg at ~4.2 K by the observation of the zero resistance. Then, he also demonstrated that many simple elements, such as Sn, Pb and so on exhibit superconductivity below 10 K.[2] Today, it has been confirmed that more than 30 species of simple elements show the superconductors at ambient pressure. In addition, many intermetallic compounds, especially containing Nb, exhibit comparatively high T_c.[3-6] The T_c gradually increased with further studies of intermetallic compounds and reached to ~25 K in Nb_3Ge in 1973.[6] Their superconductive properties and the mechanism can be explained by BCS theory proposed by Bardeen, Cooper, and Schrieffer in 1957,[7] assuming that the Cooper pairs are formed by the phonon-mediated attraction interaction. The theory predicts that the T_c would not exceed 30~40 K, and actually, the highest Tc of BCS-type superconductor is limited to ~39 K in MgB_2 discovered in 2000 so far.[8] In 1986, Bednorz and Muller suggested that La-Ba-Cu-O system exhibits the superconductivity at ~20 K.[9] however, many researchers did not care the results, regarding it as a minor or an experimental mistake. In November of the year, Tanaka group of Tokyo University examined the experimental results and confirmed that (La,Ba)CuO_{4-y} exhibits the superconductivity by demonstrating the zero resistance and the Meissner effect.[10] Then, so-called "superconductivity fever" was occurred and worldwide researches of Cu oxide superconductors were conducted. The T_c was drastically increased to ~ 93 K by the discovery of $YBa_2Cu_3O_7$ (YBCO) in the next year,[11] and the highest T_c record at ambient pressure was established in $HgBa_2Ca_2Cu_3O_x$ with T_c K,[12] which was further increased up to ~160 K by applying high pressure (~3 GPa).[13] Such the drastic increase of T_c sets our expectation that room-temperature superconductivity could be achieved in near future; however, no more T_c improvements in the Cu oxide system so far have been achieved for more than 15 years. Additionally, the mechanism of high-T_c superconductivity was discussed by many theorists for a long time, however, the theory is still controversial and has not been clarified yet. It would be one of the reasons for the theoretical stagnation that new superconductors with T_c exceeding 40 K have not been discovered excepting Cu-based superconductors. Therefore, the discoveries of new high-T_c superconductors are essential for the T_c developments and the theoretical progress of high- T_c superconductivity.

In January of 2008, it has been reported that F-substituted LaFeAsO exhibits the superconductivity at ~26 K.[14] This report attracted much interest of many researchers and induced the recurrence of a new superconductivity fever. Then, the T_c was immediately improved to ~55 K by the substitution of other rare-earth elements for the La site.[15-17] The Fe-based superconductors are the "second" high- T_c superconductors breaking the T_c limit of the BCS theory and the discoveries would be a breakthrough for the clarification of the mechanism and further improvements of the superconductive properties.

1.1.2 Crystal structures of iron-based superconductors

One of significant characteristics of iron-based superconductors is a variety of materials having various crystal structures commonly containing FeAs (or Fe*Ch*) layers, similar to that of *RE*FeAsO. *RE*FeAsO system is abbreviated as "1111-type" from the 1:1:1:1 ratio of four elements of their chemical composition. Several kinds of parent materials of iron-based superconductors and their superconductivities were reported at early stage in 2008, which include $AEFe_2As_2$ (*AE* = alkaline earth and Eu, so called as "122-type") with the $ThCr_2Si_2$-type structur,[18] *A*FeAs (*A* = alkali, so called as "111-type") with the CeFeSi-type structure[19] and Fe*Ch* with the anti-PbO type structure (so called as "11-type").[20] The crystal structures of these compounds are illustrated in Figure 1-2. They commonly have layered tetragonal lattices with alternately stacked FeAs / Fe*Ch* layers and several blocking layers along the *c*-axis. The Fe atoms form a square net and each is coordinated by four As or *Ch* atoms, resulting in layers of edge-shared $FeAs_4$ / $FeCh_4$ tetrahedra.

1.1.3 Superconductivity induced by various doping modes

Another feature of iron-based superconductors is a wide variety of ways in charge doping. Un-doped parent phases of iron-based superconductors are AFM metals and the AFM ordering along with structural phase transition from tetragonal to orthorhombic lattices occurred at 100–200 K. [21-24] Their superconductivities are induced by doping electrons or holes into the parent materials via chemical substitutions and large non-stoichiometry in chemical compositions as well as applying external pressure, accompanying with suppression of the AFM ordering and structural transition. Carrier doping via chemical substitution into these compounds is classified into 'indirect doping' by which impurity dopants are introduced into the insulating blocking layers (such as doping to the *RE* or O sites of *RE*FeAsO) and 'direct doping' by which impurity dopants into the carrier conduction layers (i.e., to the Fe sites). It is a unique feature of iron-based superconductors that both the indirect doping and the direct doping invoke superconductivity. Table 1 summarizes the relation between T_c values and dopant species reported for various type iron-based superconductors. The general carrier-doping methods for each system are described below.

(a) 1111-type *RE*FeAsO system

The chemical doping into *RE*FeAsO has been mainly performed by indirect electron-doping by replacing O^{2-} sites with monovalent F^- ions[14, 25-30] or RE^{3+} sites with quadrivalent Th4+ ions.[31-35] The maximum T_c at present are 55 K for $SmFeAsO_{1-x}F_x$[29] and 56 K for $Gd_{1-x}Th_xFeAsO$.[34] In addition, introduction of oxygen vacancies has been succeeded under high pressure conditions,[36-40] which induces maximum T_c =55 K for $SmFeAsO_{1-x}$.[38] On the other hand, direct electron-doping was performed mainly by substituting Co ions at Fe sites,[41-44] but the maximum T_c for direct doping is much lower value of 17 K for $SmFe_{1-x}Co_xAsO$[41] than that for indirect doping. Direct doping is considered to affect the carrier conduction and formation of Cooper pairs and, therefore, indirect doping is more favorable than direct doping in order to obtain higher T_c in this system. Meanwhile, isovalent substitution of As with P ions can induce superconductivity at maximum *T*c of 10 K in $LaFe(As_{1-x}P_x)O$.[45] Since this isoelectronic substitution formally does not dope charge carriers into the FeAs layer, the suppression of magnetism and emergence of superconductivity may be due to disruption of the magnetism, originating from a strong decrease in the density of state (DOS) at the Fermi level, and the resulting changes in the Fe-Fe magnetic interactions. In addition, the application of external pressure in un-doped LaFeAsO without intentional impurity-doping induced onset T_c = 21 K at 12 GPa, although clear zero resistivity was not observed.[46]

(2) 122-type $AEFe_2As_2$ system

For 122-type system, chemical doping with various elements has been reported. Indirect hole-doping with alkaline ions such as Na, K, Rb and Cs partially replacing the *AE* sites[19,47-53] and direct electron-doping with *TM* ions such as Co, Ni, Rh, Pd, Ir and Pt replacing the Fe sites[54-67] have been performed and induced the maximum T_c of 38 K in indirectly hole-doped $(Ba_{1-x}K_x)Fe_2As_2$[19] and 25 K in directly electron-doped $Ba(Fe_{1-x}Co_x)_2As_2$.[55] On the other hand, direct hole-doping into the Fe sites in $AEFe_2As_2$ was reported by use of Mn[68,69] and Cr ions.[70,71] However, this form of hole-doping leads to suppression of the AFM states without inducing superconductivity. In addition, isovalent substitution of As with P or Fe with Ru can induce superconductivity[72-77] at maximum Tc of 21 K for $Ba(Fe_{1-x}Ru_x)_2As_2$[77] and 30 K for $BaFe_2(As_{1-x}P_x)_2$,[75] respectively. In 122-type system, un-doped parent phases under an external high pressure exhibits clear zero-resistivity at high T_c of 34 K for $SrFe_2As_2$ at 3.5 GPa[78] and 35 K for $BaFe_2As_2$ at 3.0 GPa,[79] respectively.

1.1.4 General phase diagrams

Among iron-based superconductors, electronic phase diagrams (T_c vs. doping levels) of 1111-type *RE*FeAsO and 122-type $AEFe_2As_2$ systems have been mapped out for discussions about superconducting mechanisms.[61,80-84] Figures 1-3 show the typical phase diagrams for 1111-type system ($LaFeAsO_{1-x}F_x$ (a)[80] and $SmFeAsO_{1-x}F_x$ (b)[82]) and for 122-type system

($Ba_{1-x}K_xFe_2As_2$ (c)[84] and $Ba(Fe_{1-x}Co_x)_2As_2$ (d)[61]). When a certain amount of carriers are doped, the magnetic ordered (AFM) state is suppressed and structural transition temperature also decreased and then superconductivity appeared. Their superconducting phase boundaries with dome shapes are formed close to the disappearance of the AFM phase. The presence or absence of coexistence between superconductivity and AFM state is still under topic of discussion for *RE*FeAsO case. However, in case of *AE*Fe_2As_2, superconductivity coexists with AFM state and the maximum T_c appears immediately following the disappearance of AFM.[85,86]

1.1.5 Electronic structures

Figures 1-4 show the energy band-structures of parent phases of 1111-type LaFeAsO and 122-type $BaFe_2As_2$ along the high-symmetry directions of the Brillouin zone predicted by density functional theory calculations.[87] The bands around the Fermi level for both compounds are primarily formed by five bands of Fe-3*d* states, resulting in complicated hole- and electron-like Fermi surface sheets. The Fermi surface consists of 3 hole-pockets at Γ point and 2 electron-pockets at M point, as shown in Fig. 1-4 (c). The significant characteristic of band structure of 1111-type LaFeAsO is no band dispersion along Γ-Z line direction (Fig. 1-4 (a)), which basically substantiates the two-dimensional electronic nature. On the other hand, small band dispersion, indicating moderate three-dimensional Fermi surface, was observed in band structure of $BaFe_2As_2$, which was also experimentally confirmed by angle resolved photoemission spectroscopy (Fig. 1-5)[88]. These different band-structure characteristics of LaFeAsO and $BaFe_2As_2$ would originate from the difference of interlayer distance of Fe planes, i.e. 8.74 nm for LaFeAsO[23] and 6.65 nm for $BaFe_2As_2$,[19] respectively. Energy band structures of other systems are reported in ref. 89, which suggests that iron-based superconductors have overall similar band structures near the Fermi level.

1.1.6 *Comparison between Fe-based and Cu-based Superconductivity*

Fe-based superconductors could attract attention as high T_c superconductors which exceeded the limit of T_c (30~40 K) estimated by the BCS theory followed by Cu-based superconductors. They have some common points, for instance, including 3*d* metal, the layered structure, the superconductivity induced by carrier doping and so on. On the other hand, many differences can be found them. The main similarities and differences between Cu-based and Fe-based high T_c superconductors are summarized in Fig. 1-6. As the structural feature, each superconductor has layered structure, and the CuO_2 plane and FeAs layer work as the superconducting layers in each compound. In addition, their phase diagrams as a fuction of the carrier concentrations (Fig. 1-6) have many common features: Each parent material is antiferromagnetic phase, and carrier doping to the superconducting layer turns off the antiferromagnetic ordering and induces the superconductivity, which indicates that the magnetic properties of parent phase related with their high-T_c superconductivity. In each system, further carrier doping over the optimum concentration decrease the T_c and finally, it changes to the normal metallic phase. It is still controversial whether pseudogap phases of Fe-based superconductors exist or not. At any rate, these common features would provide insight into the mechanism of high-T_c superconductivity.

On the other hand, there are many differences between these superconductors. The valence band gap of Cu oxide is consisted of Cu $3d_{x2-y2}$ orbital and O $2p$ orbital, and strong electron-electron interaction of localized electrons on Cu site makes it Mott insulator in the parent phase. Such the band structure can be approximated by the single-band Hubbard model, which was supported by experimental results. In contrast to Cu oxide compounds, parent FeAs compounds show metallic behaviors, although it differs from the properties of normal metals. According to some band calculations and Angle-resolved Photoemission Spectroscopy (ARPES) measurements of FeAs compounds, the band structure near the Fermi level was consist of the deeply-interacted five Fe $3d$ orbitals, multiple electron- and hole- pockets exist in the Fermi surface. Theoretical studies suggest such unique band structure contributes the strong nesting of the Fermi surface and the appearance of the high-T_c superconductivity.

In addition, one of the most interesting differences between them is the substitution effect of 3d transition metal on the superconductivity. In the case of Cu-based superconductors, the superconductivity is induced by oxygen vacancies or element substitution of blocking layers separating the CuO_2 planes. However, the other transition metal substitution for Cu site in the superconducting CuO_2 planes strongly suppresses the superconductivity. On the other hand, the superconductivity of FeAs compounds is triggered by not only the oxygen vacancy or elemental substitution of blocking layer, but also the direct substitution of Co or Ni for the Fe in the FeAs-layer. Most of FeAs superconductors could be induce the superconductivity by the Co substitution for the Fe-site with the wide concentration range (5~20%). In addition, Ru, the 4d transition metal with the same valence number with Fe, is also effective as dopant for the Fe site. Such the contrasting substitution effect on the superconductivity reflects the different electronic characters between them: For the Cu-based superconductors, the Cu $3d^9$ configurations hybridized with the O $2p$ orbitals is essential for the superconductivity in the strongly-electron-correlated system, which leads to the sensitive character for substitution. In contrast, the Fe-based superconductivity is attributed to delocalized Fe $3d$ orbitals remotely related with As orbitals, which would cause the insensitive character for the transition-metal substitution. These facts set our expectation that the high T_c may be achieved by using the other transition metals other than Fe.

1.1.7 *Relation between structure in FeAs layer and superconducting temperature*

The relation in Fe based superconductor between the crystal structure and the superconductive property was suggested and discussed from the early stage of the study, and some papers so far evaluate the T_c based on some structural parameters. For example, some reports summarized the T_c as function of lattice parameter a (corresponding to √2 times the nearest Fe-Fe distance) and c, however, the most popular parameter used in many papers is As-Fe-As bond angle suggested by *Lee* et al. (There are two way to define the As-Fe-As angle, α- and β-angles (See the inset of Fig. 1-7), nevertheless, there is a definite relation between them due to the confinement of the space group. Therefore, the α-angle is adopted for the structural parameter in this paper. Moreover, some researchers use Fe-As-Fe angle for the parameter, but it is essentially same with the As-FeAs angle.) They demonstrated that the closer the α-angle of *Ln*FePO becomes to the regular tetrahedron angle (109.47°), the higher the T_c becomes. This result suggests that the shape of FeAs tetrahedron is important for the T_c. The tendency is likely to be applicable for 1111-type iron hydro-arsenide as mentioned later. (chapter 6).

The relation between T_c and α-angle seems to be applicable 122-type compounds. The α-angle of *Ae*$\mathrm{Fe_2As_2}$ (*Ae* = Ca, Sr, Ba, Eu), of which T_cs are higher than 20 K., are close to the regular tetrahedron angle. Especially, $\mathrm{Ba}_{1\text{-}x}\mathrm{K}_x\mathrm{Fe_2As_2}$ exhibit the maximum T_c with the 40% K substitution (x = 0.4) where the α-angle becomes closest to the regular tetrahedron angle. In addition, it is suggested that the structural changes induced by high pressure is related with the superconducting property: Kimber *et al.* demonstrated that structural changes of lattice constants and α-angle in $BaFe_2As_2$ induced by high pressure are very resemble to that induced by the substitution is more critical for the T_c increase than that of carrier doping. This suggestion is very interesting although further investigations and verifications are needed to conclude.

The empirical “regular tetrahedron rule” has been admitted by many researchers, however, how the effect of tetrahedron shape on the superconducting property has not elaborated from theoretical viewpoints yet. Assuming that the density of states (DOS) on the Fermi surface increases with the increase symmetry around Fe atom due to the degeneration of the Fe 3d orbitals, the FeAs tetrahedron would be important for superconducting properties. However, any theoretical papers discussed from such a viewpoint have not been published yet to my best knowledge. Recently, Kuroki *et al.* proposed new hypothesis which explains the relation between crystal structure and T_c from theoretical view point. They focused on the height of pnictogen height from Fe plane (h_{Pn}) and calculated the difference of the electronic structure by changing the as a parameter, considering all the five Fe-3*d* orbitals in the calculation. According to the results, appearance of Fermi surface around (π,π), which is very sensitive to the parameter h_{Pn}, leads to the nesting effect. Affect in T_c and symmetry of the superconducting gap. They concluded that the T_c increases with increasing h_{Pn}.

To examine the above -mentioned two hypotheses, the reported T_cs in Fe-based superconductor are plotted as a function of α-angle and h_{Pn} in the Fig 1-7. For comparison, the selected T_c values are the highest one of each superconductor, and theα-angle or h_{Pn} were those of the parent compounds at room temperature and ambient pressure. Note that plotted values more or less include errors because the T_c depends on how to take the value from measured data, and the refined structure also depends on the dopant species and concentration, the sample quality and so on.

In the case of the T_c-α plot (Fig 1-7), higher T_cs tend to concentrate on around the regular tetrahedron angle (109.47°), which is consistent with the "regular tetrahedron rule". Whereas, some T_cs are not so high even though their bond angles are close to the regular tetrahedron angle: As for the 1111, 122 and 21113-type compounds, the most cases are applicable to empirical rule, while the plots of 1111-type compound deviate from the rule. The angles of NaFeAs and LiFeP are close to the regular tetrahedron (~108.5), however, the T_cs are not so high (~9 K for NaFeAs, ~6 K LiFeP). Whereas, LiFeAs exhibit higher T_c (~18K) than other 111-type compounds although its α-angle (~103°) is deviate from the regular tetrahedron angle. The FeAs tetrahedron shape of LiFeAs is elongated to *c*-axis direction, which is same in the 11-type FeSe compounds. It should be reconsidered the "regular tetrahedron shapes are rare in the 1111- and 122-type compounds.

Whereas, according to the T_c-h_{Pn} plot (Fig. 1-7) it seems that the higher *Pn* position does not necessarily lead to the higher T_c if all the compounds were considered. However, this tendency could be applicable in each structure-type system, and the above-mentioned contradiction of 111-type compounds in the "regular tetrahedron rule" is resolved in this plot. Nevertheless, some contradiction could be pointed, for example, KFe_2As_2 exhibit lowest T_c (~4 K) even though it has the highest As position in the 122-type compounds. For the 11-type FeSe compounds, the T_c was improved up to 14 K by ~50% of Te substitution for the Se site, however, the further substitution decreases the T_c. According to the theory, the T_c is expected to be improved by the further Te substitution because of increase of the height; nevertheless, the actual results have not shown that. It may suggest that there is a limit to expect the T_c from FeAs structure without consideration of electronic structure or the other factors.

1.2. Objectives of this study

It is a unique feature of iron-based superconductors that both the indirect doping and the direct doping invoke superconductivity. This feature cannot be seen in the cuprate. Therefore, it is of interesting to compare the superconductivity in iron arsenide with indirect- and direct-doping. Moreover, indirectly electron doped 122-type iron-base superconductor and CaFeAsF have not been reported, although indirectly electron doped 1111-type $SmFeAsO_{1-x}F_x$ show the highest T_c (~ 55K) in the iron-based superconductors. Therefore, if indirectly doped 122-type iron-based superconductor, CaFeAsF and the new 1111-type compound were successfully synthesized, it can be expected to obtain high T_c superconductor and elucidate the relationship between these crystal structure, electronic structure and superconducting properties.

Based on the background described above, the following two objectives were established in this thesis:

(1) The first objective is to develop new doping method and synthesize new iron arsenide superconductors by using high pressure synthesis technique.

(2) The second objective is to clarify the effect of electron doping-mode, crystal structure and electric structure on superconducting properties.

1.3. Outline of this study

Chapter2: Indirectly electron-doped $Sr_{1-x}La_xFe_2As_2$ was synthesized by solid state reaction under pressures of 2-3 GPa. The optimal T_c was slightly higher than that for the indirectly electron (Co)-doped case, but much lower than that for the hole-doped case. No significant difference in the superconductivity range was observed between La- and Co-substitution. Both ranges were much narrower than that for the hole-doped case. It was concluded that the difference in electron-doping mode, either direct or indirect, was much smaller than that of polarity of the doped carrier.

Chapter 3: The 1111-type CaFeAsH were synthesized by the high-pressure technique with an excess hydrogen source. Substitution of H^- into the F^- site in CaFeAsF and the structural transition from tetragonal (space group: *P*4/*nmm*) to orthorhombic structure (space group: *Cmma*) was confirmed by NPD analysis. DFT calculation indicates that the most stable spin configuration in CaFeAsH is stripe-type antiferromagnetic ordering. In addition, energy bands located around the Fermi level are mainly composed of Fe-3*d* states. These behaviors are observed in parent compounds of 1111- and 122-type iron arsenides. Consequently, CaFeAsH is a possible candidate for a parent compound of the iron arsenide superconductors.

Chapter 4: Superconductivity was observed in $CaFe_{1-x}Co_xH$, and its properties were compared with those of $CaFe_{1-x}Co_xAsF$. The maximum T_c and width of the superconducting dome of $CaFe_{1-x}Co_xAsH$ are almost the same as those of $CaFe_{1-x}Co_xAsF$. The calculated electronic structure of CaFeAsH differs from that of CaFeAsF. The former has a 3D hole surface, with a highly 3D nature. This is caused by covalent bonding between energetically overlapped As 4*p* and H 1*s* bands. This 3D hole surface does not interfere with superconductivity. This is because poor nesting between this small hole surface and electron surfaces causes the unfavorable development of excitations, such as spin and/or charge. Hydrogen incorporated within the blocking layer acts as an indirect electron dopant, without interfering with the superconductivity.

Chapter 5: Indirect electron-doped $Ca_{1-x}La_xFeAsH$ was synthesized by the solid state reaction at 1173K under pressure of 2.5GPa. The maximum solubility of La in CaFeAsH was $x \sim 0.3$. Rietveld analysis revealed that La substitutes the Ca sites in the CaH layers and the site occupancy of La equals almost as the nominal x. The elemental composition analysis shows that La concentration was comparable to the nominal x and a small amount of oxygen (0.02-0.05) was incorporated in the samples. An anomaly derived from a structural and a magnetic transition in the ρ-T curve is suppressed by increasing La-substitution and superconductivity was observed at $x \geq 0.08$. A maximum T_c is 47.4K at $x = 0.23$ where $4\pi\chi$ is close to -1.0. The maximum T_c (47 K) in La-substituted CaFeAsH are much higher than that (23 K) of direct electron doped $CaFe_{1-x}Co_xAsH$. This is the first iron-based 1111-type superconductor except *Ln*FeAsO in which superconductivity is induced by indirect carrier doping.

Chapter 6: Finally, the summary of this study is described.

References

1. H. Kamerlingh Onnes, Akademia van Wetenncshappen (Amsterdam) **14**, 113 (1911).
2. H. Kamerlingh Onnes, Akademia van Wetenncshappen (Amsterdam) **14**, 673 (1913).
3. W. Meissner and H. Fraxz, Zeitschrift fur Physik **65**, 30 (1930).
4. G. Aschermann, E. Frmdrich, E. Justi and J. Krame, Phsikalische Zeitschrift **42**, 349 (1941).
5. B. T. Mattias, T. H. Geballe, S. Geller, and E. Corenzwit, Phys. Rev. **95**, 1435 (1954).
6. J. R. Gavaler, Appl. Phys. Lett, **23**, 480 (1973)
7. J. Bardeen, L. Cooper and J. R. Schrieffer, Phys Rev. **108**, 1175 (1957)
8. J. Nagamatsu, N. Nakagawa, T.Muranaka, Y. Zenitani and J.Akimitsu, Nature **410**, 63 (2001).
9. J. G. Bednorz and K. A. Muller, Zeitschrift fur Phsik B: Condensed matter **64**, 189 (1986).
10. H. Takagi, S. Uchida, K. Kitazawa and S. Tanaka, Jpn. J. Appl. Phys. **26**, L123 (1987).
11. M. K. Wu, J. R. Ashburn, C. J. Torng, P. H. Hor, R. L. Meng, L. Gao, Z. J. Huang, Y. Q. Wang and C. W. Chu, Phys. Rev. Lett. **58**, 908 (1987).
12. A. Schilling M. Cantoni J. D. Guo and H. R. Ott, Nature **363**, 56 (1993).
13. L. Gao, Y. Y. Xue, F. Chen, Q. Xiong, R. L. Meng, D. Ramirez and C. W. Chu, Phys. Rev. B **50**, 4260 (1994).
14. Y. Kamihara, T. Watanebe, M. Hirano, H.Hosono, J. Am. Chem. Soc. **130**, 3296 (2008).

15. G. F. Chen, Z. Li, D. Wu, G. Li, W.Z.Hu, L. Wang Phys. Rev. Lett. **100**, 247002 (2008)

16. X.H.Chen, T. Wu, G. Wu, D. F. Fang, Nature **453**, 761 (2008)

17. Z. A. Ren *et al.* Chin. Phys. Lett. **25**, 2215 (2008).

18. M. Rotter, M. Tegel, and D. Johrendt, Phys. Rev. Lett. **101** (2008) 107006.

19. X. C. Wang, Q. Q. Liu, Y. X. Lv, W. B. Gao, L. X. Yang, R. C. Yu, F. Y. Li, and C. Q. Jin, Solid State Commun. **148** (2008) 538.

20. F.-C. Hsu, J.-Y. Luo, K.-W. Yeh, T.-K. Chen, T.-W. Huang, P. M. Wu, Y.-C. Lee, Y.-L. Huang, Y.-Y. Chu, D.-C. Yan, and M.-K. Wu, Proc. Natl. Acad. Sci. USA **105** (2008) 14262.

21. C. de la Cruz, Q. Huang, J. W. Lynn, J. Li, W. R. II, J.L. Zarestky, H. A. Mook, G. F. Chen, J. L. Luo, N. L. Wang, and P. Dai, Nature **453** (2008) 899.

22. T. Nomura, S. W. Kim, Y. Kamihara, M. Hirano, P. V. Sushko, K. Kato, M. Takata, A. L. Shluger, and H. Hosono, Supercond. Sci. Technol. **21** (2008) 125028.

23. Q. Huang, Y. Qiu, W. Bao, M. A. Green, J. W. Lynn, Y. C. Gasparovic, T. Wu, G. Wu, and X. H. Chen, Phys. Rev. Lett. **101** (2008) 257003.

24. M. Rotter, M. Tegel, D. Johrendt, I. Schellenberg, W. Hermes, and R. Pöttgen, Phys. Rev. B **78** (2008) 020503.

25. G. F. Chen, Z. Li, D. Wu, G. Li, W. Z. Hu, J. Dong, P. Zheng, J. L. Luo, and N. L.

Wang, Phys. Rev. Lett. **100** (2008) 247002.

26. Z. A. Ren, J. Yang, W. Lu, W. Yi, G. C. Che, X. L. Dong, L. L. Sun, and Z. X. Zhao, Mater. Res. Innov. **12** (2008) 105.
27. Y. Qiu, W. Bao, Q. Huang, T. Yildirim, J. M. Simmons, M. A. Green, J. W. Lynn, Y. C. Gasparovic, J. Li, T. Wu, G. Wu, and X. H. Chen, Phys. Rev. Lett. **101** (2008) 257002.
28. X. H. Chen, T. Wu, G. Wu, R. H. Liu, H. Chen, and D. F. Fang, Nature **453** (2008) 761.
29. Z.-A. Ren, W. Lu, J. Yang, W. Yi, X.-L. Shen, Z.-C. Li, G.-C. Che, X.-L. Dong, L.-L. Sun, F. Zhou, and Z.-X. Zhao, Chin. Phys. Lett. **25** (2008) 2215.
30. J.-W. G. Bos, G. B. S. Penny, J. A. Rodgers, D. A. Sokolov, A. D. Huxley, and J.P. Attfield, Chem. Commun. (2008) 3634.
31. J. Prakash, S. J. Singh, S. Patnaik, and A. K. Ganguli, J. Phys.: Condens. Matter 21 (2009) 175705.
32. M. Xu, F. Chen, C. He, H.-W. Ou, J.-F. Zhao, and D.-L. Feng, Chem. Mater. 20 (2008) 7201.
33. N. D. Zhigadlo, S. Katrych, S. Weyeneth, R. Puzniak, P. J. W. Moll, Z. Bukowski, J. Karpinski, H. Keller, and B. Batlogg, Phys. Rev. B 82 (2010) 064517.
34. C. Wang, L. Li, S. Chi, Z. Zhu, Z. Ren, Y. Li, Y. Wang, X. Lin, Y. Luo, S. Jiang,

X. Xu, G. Cao, and Z. Xu, EPL 83 (2008) 67006.

35 . L.-J. Li, Y.-K. Li, Z. Ren, Y.-K. Luo, X. Lin, M. He, Q. Tao, Z.-W. Zhu, G.-H. Cao, and Z.-A. Xu, Phys. Rev. B 78 (2008) 132506.

36 . J. Yang, Z.-C. Li, W. Lu, W. Yi, X.-L. Shen, Z.-A. Ren, G.-C. Che, X.-L. Dong, L.-L. Sun, F. Zhou, and Z.-X. Zhao, Supercond. Sci. Technol. 21 (2008) 082001.

37. H. Kito, H. Eisaki, A. Iyo, J. Phys. Soc. Jpn. 77 (2008) 063707.

38. Z.-A. Ren, G.-C. Che, X.-L. Dong, J. Yang, W. Lu, W. Yi, X.-L. Shen, Z.-C. Li, L.-L. Sun, F. Zhou, and Z.-X. Zhao, EPL 83 (2008) 17002.

39. J. Yang, X.-L. Shen, W. Lu, W. Yi, Z.-C. Li, Z.-A. Ren, G.-C. Che, X.-L. Dong, L.-L. Sun, F. Zhou, and Z.-X. Zhao, New J. Phys. 11 (2009) 025005.

40. P. M. Shirage, K. Miyazawa, K. Kihou, C.-H. Lee, H. Kito, K. Tokiwa, Y. Tanaka, H. Eisaki, and A. Iyo, EPL 92 (2010) 57011.

41. C. Wang, Y. K. Li, Z. W. Zhu, S. Jiang, X. Lin, Y. K. Luo, S. Chi, L. J. Li, Z. Ren, M. He, H. Chen, Y. T. Wang, Q. Tao, G. H. Cao, and Z. A. Xu, Phys. Rev. B 79 (2009) 054521.

42. L.-D. Zhao, D. Berardan, C. Byl, L. Pinsard-Gaudart, and N. Dragoe, J. Phys.: Condens. Matter 22 (2010) 115701.

43. A. Marcinkova, D. A. M. Grist, I. Margiolaki, T. C. Hansen, S. Margadonna, and

J.-W. G. Bos, Phys. Rev. B 81 (2010) 064511.

44. P. M. Shirage, K. Miyazawa, H. Kito, H. Eisaki, and A. Iyo, Physica C 469 (2009) 898.
45. C. Wang, S. Jiang, Q. Tao, Z. Ren, Y. Li, L. Li, C. Feng, J. Dai, G. Cao, and Z. Xu, EPL 86 (2009) 47002.
46. H. Okada, K. Igawa, H. Takahashi, Y. Kamihara, M. Hirano, H. Hosono, K. Matsubayashi, and Y. Uwatoko, J. Phys. Soc. Jpn. 77 (2008) 113712.
47. P. M. Shirage, K. Miyazawa, H. Kito, H. Eisaki, and A. Iyo, Appl. Phys. Express 1 (2008) 081702.
48. K. Zhao, Q. Q. Liu, X. C. Wang, Z. Deng, Y. X. Lv, J. L. Zhu, F. Y. Li, and C. Q. Jin, J. Phys.: Condens. Matter 22 (2010) 222203.
49. C. Gen-Fu, L. Zheng, L. Gang, H. Wan-Zheng, D. Jing, Z. Jun, Z. Xiao-Dong, Z. Ping, W. Nan-Lin, and L. Jian-Lin, Chin. Phys. Lett. 25 (2008) 3403.
50. H. S. Jeevan, Z. Hossain, D. Kasinathan, H. Rosner, C. Geibel, and P. Gegenwart, Phys. Rev. B 78 (2008) 092406.
51. K. Sasmal, B. Lv, B. Lorenz, A. M. Guloy, F. Chen, Y.-Y. Xue, and C.-W. Chu, Phys. Rev. Lett. 101 (2008) 107007.
52. Y. Qi, Z. Gao, L. Wang, D. Wang, X. Zhang, and Y. Ma, New J. Phys. 10 (2008)

123003.

53. Z. Bukowski, S. Weyeneth, R. Puzniak, P. Moll, S. Katrych, N. D. Zhigadlo, J. Karpinski, H. Keller, and B. Batlogg, Phys. Rev. B 79 (2009) 104521.

54. A. S. Sefat, R. Jin, M. A. McGuire, B. C. Sales, D. J. Singh, and D. Mandrus, Phys. Rev. Lett. 101 (2008) 117004.

55. Y. Nakajima, T. Taen, and T. Tamegai, J. Phys. Soc. Jpn. 78 (2009) 023702.

56. A. Leithe-Jasper, W. Schnelle, C. Geibel, and H. Rosner, Phys. Rev. Lett. 101 (2008) 207004.

57. N. Kumar, R. Nagalakshmi, R. Kulkarni, P. L. Paulose, A. K. Nigam, S. K. Dhar, and A. Thamizhavel, Phys. Rev. B 79 (2009) 012504.

58. L. J. Li, Y. K. Luo, Q. B. Wang, H. Chen, Z. Ren, Q. Tao, Y. K. Li, X. Lin, M. He, Z. W. Zhu, G. H. Cao, and Z. A. Xu, New J. Phys. 11 (2009) 025008.

59. N. Kumar, S. Chi, Y. Chen, K. G. Rana, A. K. Nigam, A. Thamizhavel, W. Ratcliff, S. K. Dhar, and J. W. Lynn, Phys. Rev. B 80 (2009) 144524.

60. X. Zhu, F. Han, G. Mu, P. Cheng, J. Tang, J. Ju, K. Tanigaki, and H.-H. Wen, Phys. Rev. B 81 (2010) 104525.

61. N. Ni, A. Thaler, A. Kracher, J. Q. Yan, S. L. Bud’ko, and P. C. Canfield, Phys. Rev. B 80 (2009) 024511.

62. X. L. Wang, H. Y. Shi, X. W. Yan, Y. C. Yuan, Z.-Y. Lu, X. Q. Wang, and T.-S. Zhao, Appl. Phys. Lett. 96 (2010) 012507.

63. N. Ni, A. Thaler, J. Q. Yan, A. Kracher, E. Colombier, S. L. Bud'ko, P. C. Canfield, and S. T. Hannahs, Phys. Rev. B 82 (2010) 024519.

64. S. R. Saha, N. P. Butch, K. Kirshenbaum, and J. Paglione, Phys. Rev. B 79 (2009) 224519.

65. F. Han, X. Zhu, P. Cheng, G. Mu, Y. Jia, L. Fang, Y. Wang, H. Luo, B. Zeng, B. Shen, L. Shan, C. Ren, and H.-H. Wen, Phys. Rev. B 80 (2009) 024506.

66. Y. Nishikubo, S. Kakiya, M. Danura, K. Kudo, and M. Nohara, J. Phys. Soc. Jpn. 79 (2010) 095002.

67. Y. Qi, L. Wang, Z. Gao, D. Wang, X. Zhang, C. Wang, C. Yao, and Y. Ma, New J. Phys. 13 (2011) 033020.

68. J. S. Kim, S. Khim, H. J. Kim, M. J. Eom, J. M. Law, R. K. Kremer, J. H. Shim, and K. H. Kim, Phys. Rev. B 82 (2010) 024510.

69. Y. Liu, D. L. Sun, J. T. Park, and C. T. Lin, Physica C 470 (2010) S513.

70. A. S. Sefat, D. J. Singh, L. H. VanBebber, Y. Mozharivskyj, M. A. McGuire, R. Jin, B. C. Sales, V. Keppens, and D. Mandrus, Phys. Rev. B 79 (2009) 224524.

71. K. Marty, A. D. Christianson, C. H. Wang, M. Matsuda, H. Cao, L. H. VanBebber,

J. L. Zarestky, D. J. Singh, A. S. Sefat, and M. D. Lumsden, Phys. Rev. B 83 (2011) 060509.

72. Z. Ren, Q. Tao, S. Jiang, C. Feng, C. Wang, J. Dai, G. Cao, and Z. Xu, Phys. Rev. Lett. 102 (2009) 137002.

73. H. L. Shi, H. X. Yang, H. F. Tian, J. B. Lu, Z. W. Wang, Y. B. Qin, Y. J. Song, and J. Q. Li, J. Phys.: Condens. Matter 22 (2010) 125702.

74. S. Jiang, H. Xing, G. Xuan, C. Wang, Z. Ren, C. Feng, J. Dai, Z. Xu, and G. Cao, J. Phys.: Condens. Matter 21 (2009) 382203.

75. S. Chong, S. Hashimoto, and K. Kadowaki, Solid State Commun. 150 (2010) 1178.

76. W. Schnelle, A. Leithe-Jasper, R. Gumeniuk, U. Burkhardt, D. Kasinathan, and H. Rosner, Phys. Rev. B 79 (2009) 214516.

77. S. Sharma, A. Bharathi, S. Chandra, V. R. Reddy, S. Paulraj, A. T. Satya, V. S. Sastry, A. Gupta, and C. S. Sundar, Phys. Rev. B 81 (2010) 174512.

78. H. Kotegawa, H. Sugawara, and H. Tou, J. Phys. Soc. Jpn. 78 (2008) 013709.

79. F. Ishikawa, N. Eguchi, M. Kodama, K. Fujimaki, M. Einaga, A. Ohmura, A. Nakayama, A. Mitsuda, and Y. Yamada, Phys. Rev. B 79 (2009) 172506.

80. H. Luetkens, H.-H. Klauss, M. Kraken, F. J. Litterst, T. Dellmann, R. Klingeler, C. Hess, R. Khasanov, A. Amato, C. Baines, M. Kosmala, O. J. Schumann, M. Braden, J. Hamann-Borrero, N. Leps, A. Kondrat, G. Behr, J. Werner, and B. Buchner, Nat. Mater. 8 (2009) 305.

81. J. Zhao, Q. Huang, C. de la Cruz, S. Li, J. W. Lynn, Y. Chen, M. A. Green, G. F. Chen, G. Li, Z. Li, J. L. Luo, N. L. Wang, and P. Dai, Nat. Mater. 7 (2008) 953.

82. A. J. Drew, C. Niedermayer, P. J. Baker, F. L. Pratt, S. J. Blundell, T. Lancaster, R. H. Liu, G. Wu, X. H. Chen, I. Watanabe, V. K. Malik, A. Dubroka, M. Rossle, K. W. Kim, C. Baines, and C. Bernhard, Nat. Mater. 8 (2009) 310.

83. T. Hanna, Y. Muraba, S. Matsuishi, N. Igawa, K. Kodama, S. Shamoto, and H.Hosono, Phys. Rev. B 84 (2011) 024521.

84. M. Rotter, M. Pangerl, M. Tegel, and D. Johrendt, Angew. Chem. Int. Ed. 47 (2008) 7949.

85. D. K. Pratt, W. Tian, A. Kreyssig, J. L. Zarestky, S. Nandi, N. Ni, S. L. Bud'ko, P. C. Canfield, A. I. Goldman, and R. J. McQueeney, Phys. Rev. Lett. 103 (2009) 087001.

86. E. Wiesenmayer, H. Luetkens, G. Pascua, R. Khasanov, A. Amato, H. Potts, B. Banusch, H.-H. Klauss, and D. Johrendt, Phys. Rev. Lett. 107 (2011) 237001.

87. I. A. Nekrasov, Z. V. Pchelkina, and M. V. Sadovskii, JETP Letters 88 (2009) 144.

88. W. Malaeb, T. Yoshida, A. Fujimori, M. Kubota, K. Ono, K. Kihou, P. M. Shirage, H. Kito, A. Iyo, H. Eisaki, Y. Nakajima, T. Tamegai, and R. Arita, J.Phys. Soc. Jpn. 78 (2009) 123706.

89. T. Miyake, K. Nakamura, R. Arita, and M. Imada, J. Phys. Soc. Jpn. 79 (2010) 044705.

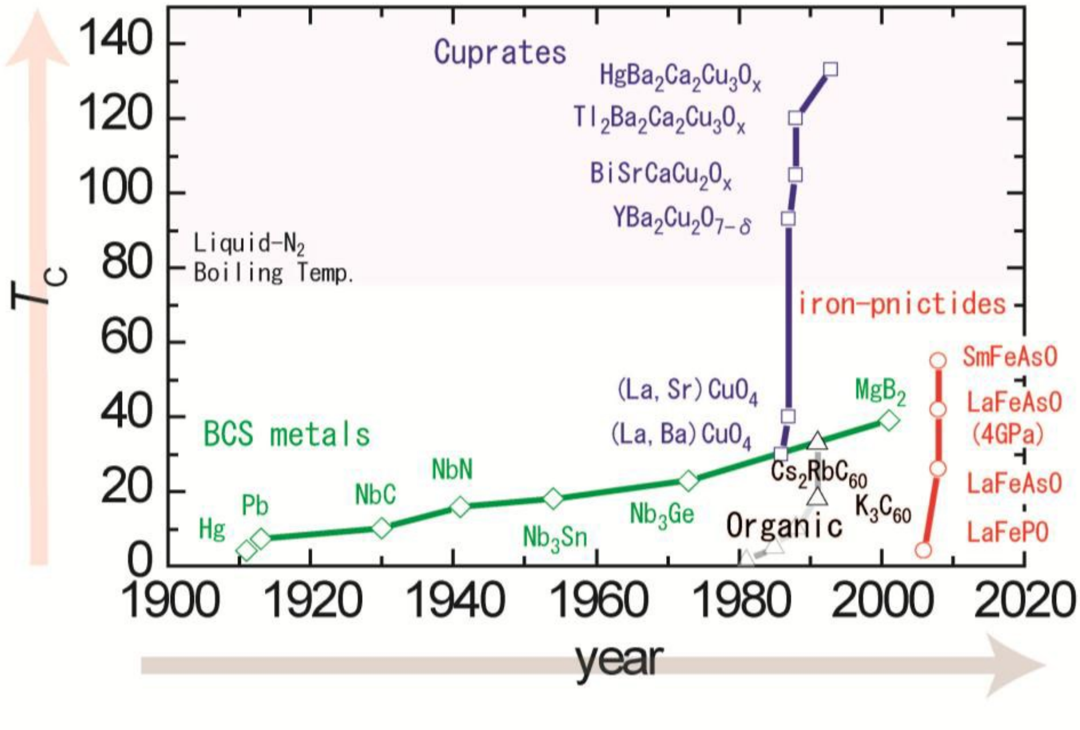

Figure 1-1 . History of superconductors and developments of the superconducting transition temperatures (T_c). The diamond, square, triangle and circle symbols indicate the T_c of BCS metals [47-52], cuprates [53-56], organics [102-105], and iron-based superconductors [84-89], respectively.

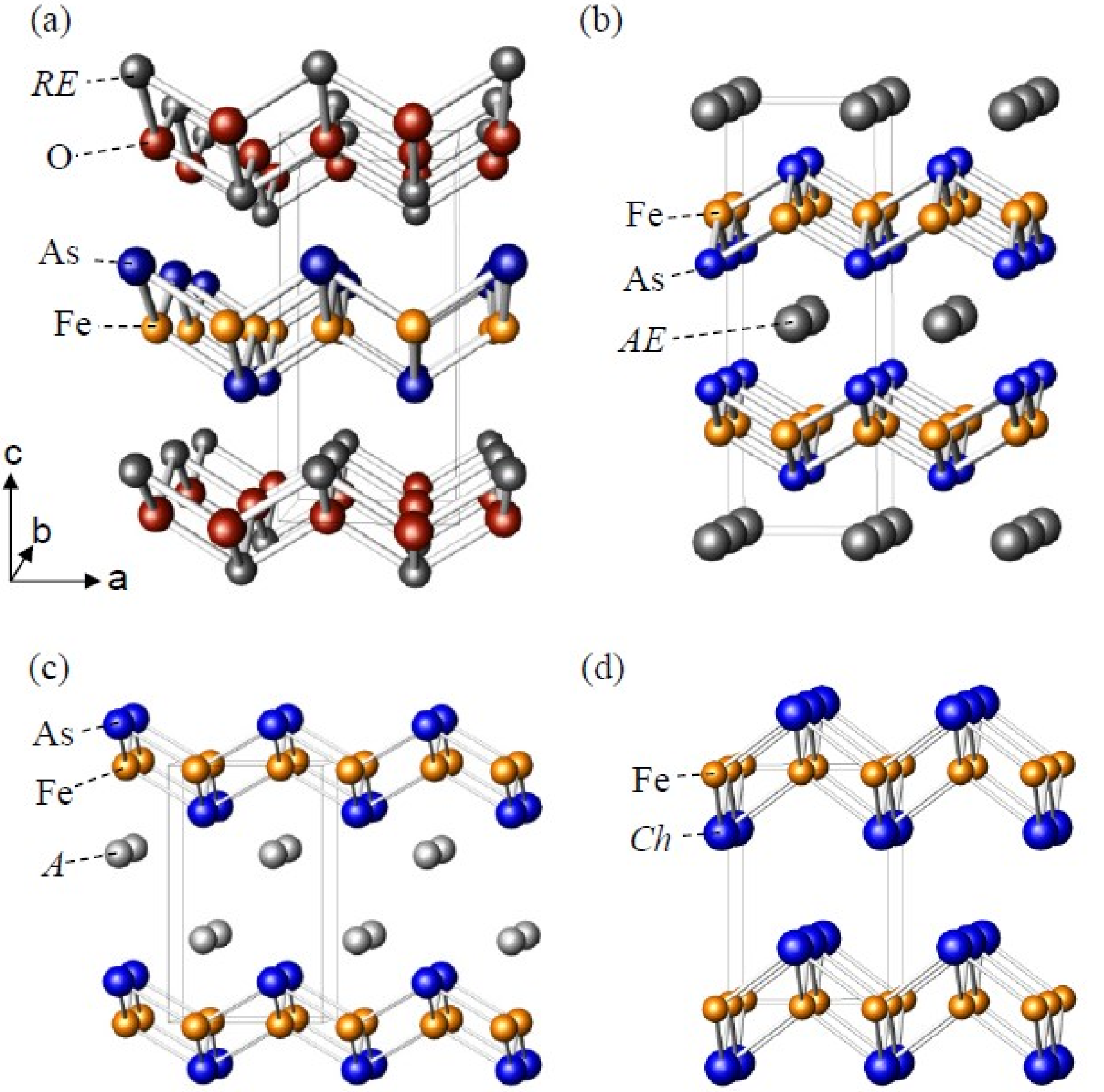

Figure 1-2. Crystal structures of representative iron-based superconductors of (a) 1111-type *RE*FeAsO (*RE* = rare earth), (b) 122-type *AE*Fe2As2 (*AE* = alkaline earth), (c) 111-type *A*FeAs (*A* = alkali), and (d) 11-type Fe*Ch* (*Ch* = chalcogen).

Table I. Structure, composition, dopant species, and T_c for representative iron-based superconductors.

Structure	Composition	Dopant (Site)	T_c (K)	References
1111	*RE*FeAsO (*RE*=La–Dy)	F(O)	26–55	[21, 43–48]
	*RE*FeAsO (*RE*=Y, La–Er)	Vacancy (O)	35–55	[61–65]
	*RE*FeAsO (*RE*=La, Nd, Sm, Gd, Tb)	Th (*RE*)	30–56	[56–60]
	*RE*FeAsO (*RE*=La, Ce, Pr, Nd, Sm)	Co (Fe)	13–17	[66–69]
	LaFeAsO	P (As)	10	[70]
122	*AE*Fe_2As_2 (*AE*=Ca, Sr, Ba, Eu)	*A* (*AE*) (*A*=Na, K, Rb, Cs)	23–38	[50, 72–78]
	AEFe_2As_2 (*AE*=Ca, Sr, Ba, Eu)	*TM* (Fe) (*TM*=Co, Ni, Rh, Pd, Ir, Pt, Ru)	17–25	[79–92, 101, 102]
	AEFe_2As_2 (*AE*=Ca, Sr, Ba, Eu)	P (As)	13–31	[97–100]
111	$Li_{0.8}FeAs$		18	[105, 106]
	$Na_{0.9}FeAs$		12–18	[107, 108]
11	$Fe_{1.01}Se$		8	[110]
	$FeSe_{0.5}Te_{0.5}$		15	[112]

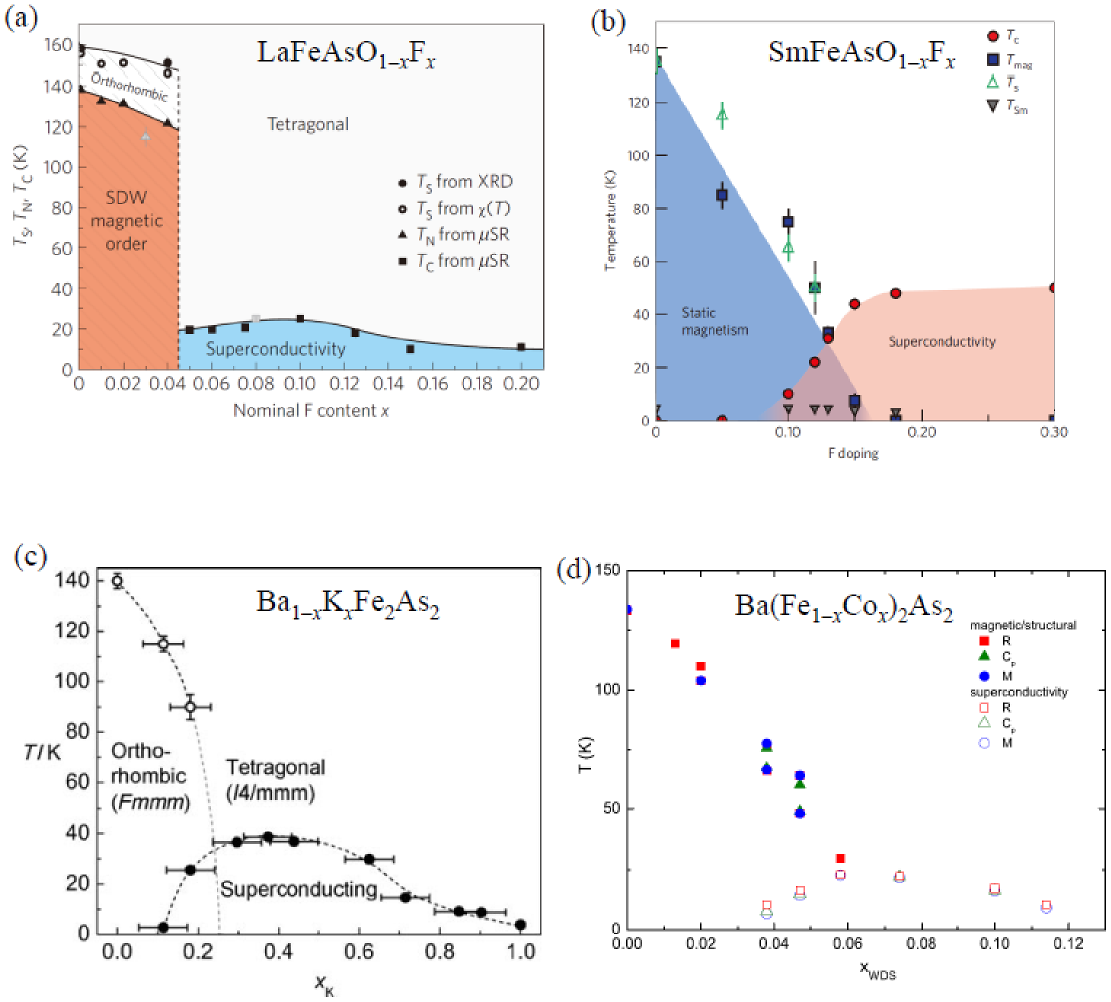

Figure 1-3. Representative electronic phase diagrams of (a) LaFeAsO1−xFx [113], (b) SmFeAsO$_{1-x}$F$_x$ [115], (c) Ba$_{1-x}$K$_x$Fe$_2$As$_2$ [117], and (d) Ba(Fe$_{1-x}$Co$_x$)$_2$As$_2$ [86].

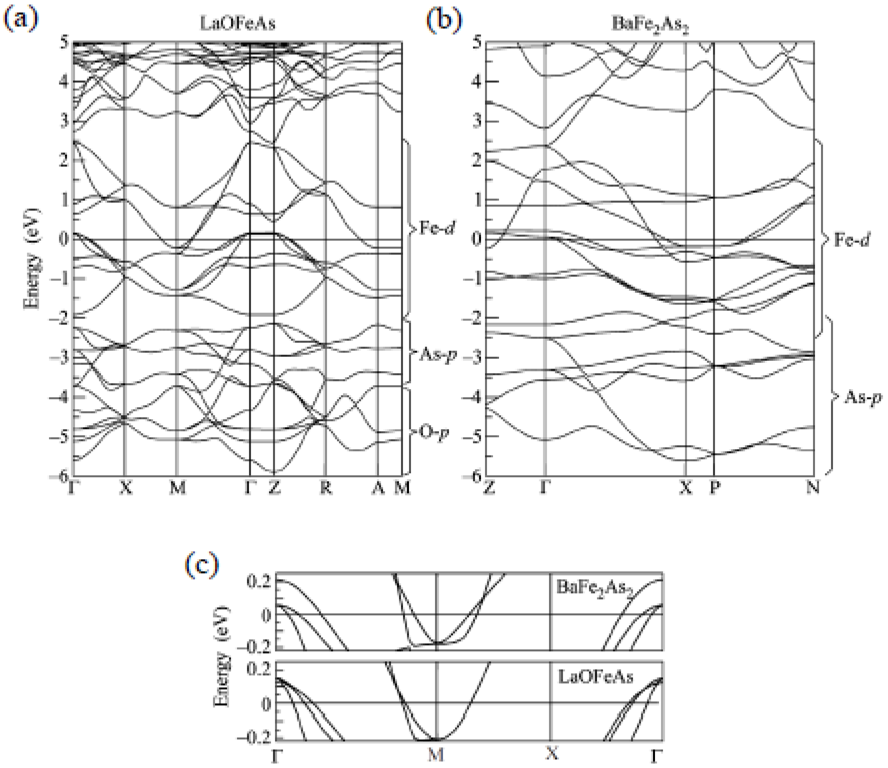

Figure 1-4. Energy band structures of LaFeAsO (a) and $BaFe_2As_2$ (b) calculated by density functional theory (DFT) calculations [120]. (c) The magnified band structures near Fermi level.

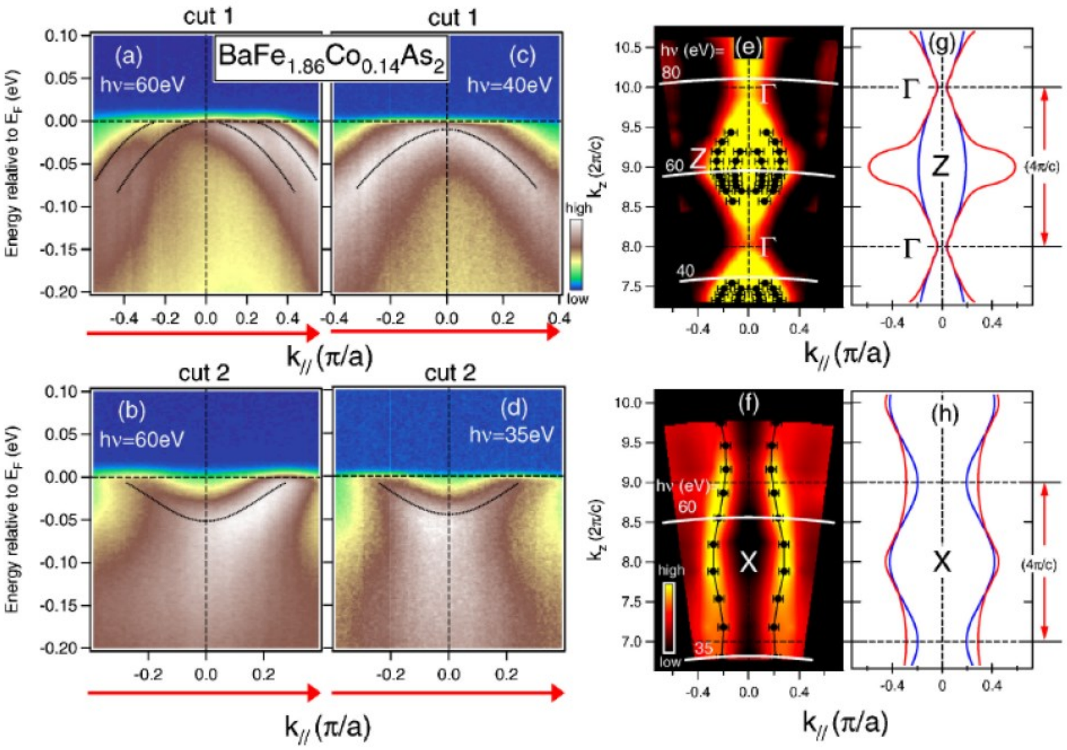

Figure 1-5. Energy band structures of $Ba(Fe_{1-x}Co_x)_2As_2$ measured by angle resolved photoemission spectroscopy [121].

	Cu-based SC	**Fe-based SC**
SC layer	CuO_2 plane	FeAs layer
Parent phase	Mott Insulater	Bad metal (semi-metal)
Band structure near Fermi level	Single-band $Cu3d_{x2-y2}$ and O2p orbital	Multi-band complicated Fe3d orbitals
Doping method	Oxygen vacancy, Indirect doping	+ Direct doping (Co, Ni substitution)
Phase diagram	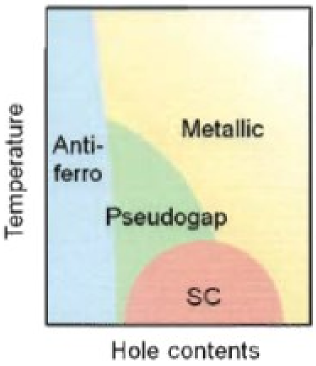	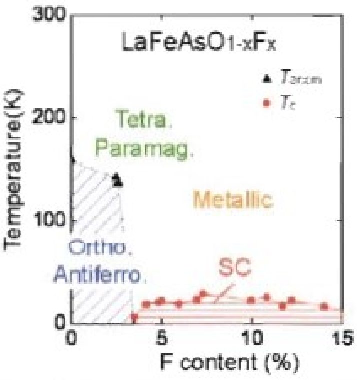

Fig 1-6. Similarities and differences between Cu-based and Fe-based superconductors (SC). The schematic phase diagram captured its typical characters are shown for Cu-based superconductors.

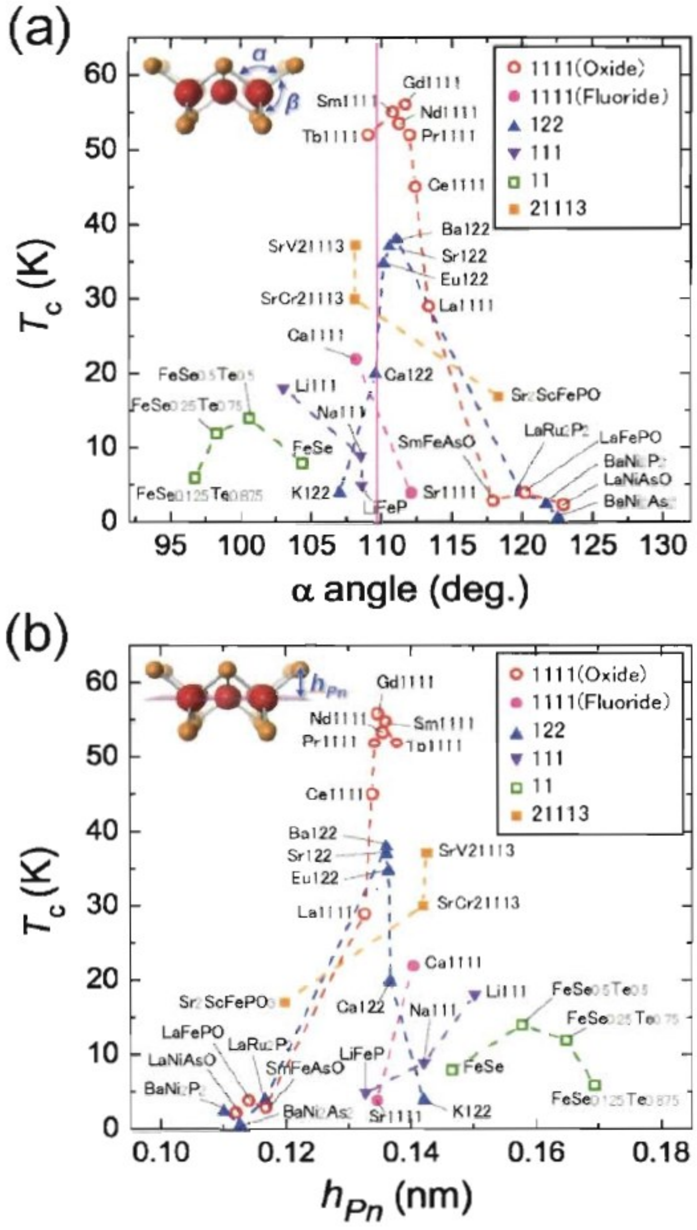

Fig 1-7. The T_c plots arranged as a function of As-Fe-As angle, α (a) and pnictgen height, h_{Pn} (b)

The insets show the explanation drawing of α-angle and h_{Pn}.

Chapter 2: High-pressure synthesis of the indirectly electron-doped 122 iron superconductor La-substituted $SrFe_2As_2$ with T_c = 22 K

2.1. Introduction

In the 1111 phase, it is established that electron-doping effectively works to induce superconductivity as exemplified by $LnFeAsO_{1-x}F_x$ (where *Ln*: lanthanide). However, the hole doping effect still remains unclear.[1] Information on both electron-doped and hole-doped cases in superconductivity is important for examining the modification of the Fermi surface by carrier doping. The 122 phase[2] is more favorable than the 1111 phase for examining this issue, because the phase forming reaction temperature is sufficiently low that sub-reactions within container vessels and/or selective vaporization of a component may be suppressed. Direct electron-doping to FeAs-layers by substituting the iron site with appropriate transition metals (e.g. Co^{2+}, Ni^{2+})[3,4] can be achieved and superconductivity was induced by the doping mode. However, to date there are no reports of superconductivity of 122 system induced by indirect electron-doping via aliovalent cation substitution to alkaline earth metal site. While G. Wu et al.[5] examined the La^{3+} substitution at the alkaline earth metal site, solid state reactions of the ingredient mixture for $Ba_{1-x}La_xFe_2As_2$ did not yield the La-substituted 122 phase by using the conventional glass-tube technique under ambient pressure. Leithe-Jasper *et al.*[6] reported density functional theory (DFT) calculations showing a distinct difference in phase instability and effect of magnetic moment, originating from the electronic structure between Co-doped and La-doped $SrFe_2As_2$. The La-substituted phase was electronically unstable, but no phase instability was induced by Co-doping. This prediction is consistent with the formation of $Sr_{1-x}La_xFe_2As_2$ phases having not been reported to date.

The ionic radius of La^{3+} (116 pm) is smaller than that of Sr^{2+} (126 pm), and so it is likely that a high pressure synthesis would be effective for obtaining La-substituted $SrFe_2As_2$. In this chapter, we report that $Sr_{1-x}La_xFe_2As_2$ ($x \leq 0.6$) compounds with negative Seebeck coefficients can be synthesized at high pressure (2-3 GPa), and superconductivity with a maximum T_c of 22 K was observed in the range of $0.2 \leq x \leq 0.5$.

2.2. Experimental

Samples of nominal chemical composition $Sr_{1-x}La_xFe_2As_2$ were synthesized by solid state reaction under high pressure. The starting materials were SrAs, LaAs and Fe_2As, each of them having been prepared from their respective metals. The mixture of these materials was sealed in a metal Ta tube with a Ta cap, by spot-welding in a glove box filled with a dry Ar gas. Tubes were then heated at 1273 K for 2 h under pressures of 2-4 GPa. A belt-type anvil cell was employed for the high pressure synthesis. Crystalline phases in the resulting samples were identified by powder X-ray diffraction (XRD) using a Bruker diffractometer model D8 ADVANCE (Cu rotating anode). The Rietveld analysis of XRD patterns was performed using RIETAN-FP code[7]. The 4-probe resistivity and magnetic susceptibility were measured in the temperature range of 300-2 K, using a PPMS (Quantum Design) with a VSM attachment. Thermopower was measured at 300 K to check the polarity of the major carrier in the resulting samples. Because solubility of La in $Ae\mathrm{Fe_2As_2}$ (Ae = Sr, Ba) is small, solid state reactions of the ingredient mixture for $Ae_{1-x}\mathrm{LaxFe_2As_2}$ did not yield the La-substituted 122 phase by using the conventional glass-tube technique under ambient pressure. LaAs and $SrFe_2As_2$ phases were identified by XRD, indicating segregation of La from the 122 phase. When a pressure of 2 GPa was applied during the reaction, the formation of LaAs was suppressed and an XRD peak shift was observed. When the applied pressure was increased to 3 GPa, the volume fraction of impurities increased. The target became a minority phase at 4 GPa, and so reaction conditions were fixed at 2 GPa and 1273 K for 2 h.

2.3. Results and Discussion

2.3.1. XRD and Rietveld refinement

Figure 1 (a) shows observed and calculated XRD patterns of samples synthesized at 2 GPa. Segregation of La was suppressed up to $x = 0.5$, but the LaAs phase was apparent for $x = 0.6$. A trace amount of LaFeAsO (< 3 vol %) was identified in all samples. The same amount of LaFeAsO phase was observed as for samples prepared by the glass-tube technique, thus the formation of LaFeAsO was attributed to oxygen contamination in ingredients during preparation and synthesis. Figure 1 (b) shows the variation of lattice constants (*a* and *b*), unit cell volume *V*, and the separation between Sr and As ions $r_{\text{Sr-As}}$ within the $Sr_{1-x}La_xFe_2As_2$ phase as functions of nominal *x*. The unit cell volume continuously decreased from $x = 0$ to 0.5, indicating that the solubility limit of La in $SrFe_2As_2$ was $x < 0.6$. Providing there was separation between Sr and As ions in the 122 phase, $r_{\text{Sr-As}}$, decreased with the mean size of the cations at the Sr-site, and the value of $r_{\text{Sr-As}}$ should decrease linearly with *x*. The difference in $r_{\text{Sr-As}}$ between $x = 0$ and $x = 1$ (extrapolated) should be the difference in the ionic radius between Sr^{2+} and La^{3+} (~10 pm). The observed trend and value (~10 pm) in Figure 1 (b) agrees with the above assumption, confirming that La^{3+} substitutes the site of Sr^{2+}. With an increase of nominal *x*, the broadening of diffraction peaks increased, especially for the 00*l* diffractions. The length of the *c*-axis was more sensitive to *x* variations than that of the *a*-axis (See Figure 1 (b)). A possible reason for the broadening was the modulation of lattice spacing, due to inhomogeneity in local La-concentration. The modulation of lattice spacing yielded the crystallographic strain. The degree of modulation as crystallographic strain was calculated from the line-broadening obtained by the Rietveld analysis of the XRD patterns. Figure 1 (c) shows isotropic and anisotropic crystallographic strains as a function of x. S_G and S_L^{iso} are the isotropic strains calculated from Lorentzian and Gaussian-type components of pseudo-Vogt functions, which describe line broadening for the Rietveld analysis. S_L^{aniso} is the anisotropic strain along the [001] axis, calculated from the Lorentzian component.[8] In this analysis, the value of parameter corresponding to crystallite size was fixed to that optimized for the sample of $x = 0$. Both isotropic and anisotropic lattice strains start to increase from $x = 0.1$, and then increase markedly when $x > 0.4$. Thus, it is presumed that the large strain induced in the crystallites by the La-substitution restricted the solubility limit of La^{3+} at the Sr^{2+} site.

2.3.2 Electron transport property

Figure 2 shows the temperature dependence of resistivity for samples with different x. An anomaly arising from the crystallographic transition[9] accompanied with the magnetic transition at around 200 K, and was suppressed with x. A sharp resistivity drop instead appeared from $x = 0.2$, and zero resistivity was observed at $x \geq 0.3$.

Figure 3 shows the temperature dependence of magnetic susceptibility χ for each sample. Pellets were obtained by sintering synthesized powders, and were used for the measurements. Samples all underwent demagnetization at 300 K before magnetic measurements were carried out. A distinct negative shift of χ was observed for $x = 0.2$-0.5 in the temperature range below

~22 K. The top of Figure 3 (b) shows *M-H* curves for the samples. The shielding volume fraction calculated from the slope of the *M-H* curve was ~10 % at x = 0.3, and reached a maximum of ~70 % at x = 0.4. It then dropped to ~5 % at x = 0.5. The precipitation of impurity phases was apparent from XRD patterns for the samples prepared at 3GPa, indicating that the La-concentration in the Sr-122 crystals was smaller than the nominal x. Since the c-axis length for samples prepared at 2 GPa was almost proportional to the nominal x, it could be used as a measure for the content of La substituting at the Sr sites. Figure 3 (c) shows the shielding volume fraction evaluated from *dM/dH* vs. lattice constant c for samples prepared at 2 and 3 GPa. The samples appeared to also display a maximum volume fraction of superconducting phase at the same c-axis length.

Figure 4 shows the Seebeck coefficients of $Sr_{1-x}M_xFe_2As_2$(M = K and La) at 300 K. It was evident that the sign of Seebeck coefficients for the La-doped samples was negative, and opposite to that observed for the K-doped samples.[10] This result substantiated that electrons were effectively doped to the FeAs layer by the La-substitution as intended, and that superconductivity was induced by electron-doping.

Analysis of XRD patterns indicated that La-substitution induced anisotropic strain along the c-direction. Saha et al. reported that the superconductivity of non-doped $SrFe_2As_2$ was promoted by internal strain, and caused by stress during crystal growth which disappeared during thermal annealing.[11] In the current study, we examined the annealing at 573 K of $Sr_{0.6}La_{0.4}Fe_2As_2$ prepared at 2 GPa, but found no significant changes in superconducting properties (T_c and shielding volume) or XRD profile. This indicated that the superconductivity of our samples was not due to mechanical stress like that reported by Saha et al.

The reason for T_c on the ρ-T profile not changing with La concentration was then investigated. The profile analysis of XRD patterns revealed that there is no indication of phase separation but distinct persistent crystalline strain are present in the $(Sr,La)Fe_2As_2$. This strain is attributed to inhomogeneous replacement of Sr ions with La ions in the $SrFe_2As_2$ phase. In each sample with the observable T_c, there was a portion in which the La-concentration was the same as $x = 0.4$ with a maximum $T_c \sim 22$ K and these portions are percolated throughout the bulk samples. Since the onset T_c is controlled by the highest-T_c region ($La_{0.4}Sr_{0.6}Fe_2As_2$), we may understand the obtained results that the shielding volume fraction changed with x, but T_c remained almost unchanged. Here, note that substitution between Sr and La is easy in cuprates even in conventional solid state reaction processes but impossible in Sr-122 iron arsenide. This makes a sharp contrast between these two representative superconductive systems.

2.3.3. Electron phase diagram

Figure 5 summarizes the electronic phase diagram for directly/indirectly, hole/electron-doped $SrFe_2As_2$. Onset T_c and anomaly temperature in ρ-T curves indicating structural/magnetic transition are plotted in this figure. Here, doped carrier numbers per Fe are plotted in place of compositions in the figure. It is of interest to compare the present results (indirect electron-doping) with those for $SrFe_{2-y}Co_yAs_2$ (direct doping).[6,9] Superconductivity in the latter system occurred at $0.2 \leq y \leq 0.5$. T_c had a maximum of 19 K at $y \sim 0.2$, at which point anti-ferromagnetic ordering decreased with x and disappeared at $y = 0.5$. In the present system, bulk superconductivity (shielding volume > ~10 %) was observed at $x = 0.3$ and 0.4 for samples prepared at 2GPa, and $x = 0.4$ and 0.5 for those prepared at 3 GPa.[12] The number of electrons injected into the FeAs layer was $x/2 = y$ per Fe ion. Superconductivity was induced for the La-substituted system if electron numbers of 0.15-0.25 per Fe for samples prepared at 2 GPa, and 0.2-0.25 per Fe ion for those prepared at 3 GPa, were doped to the parent phase. This range is narrower than that for the Co-substituted system, and both ranges are much narrower than that for the hole-doped case. In this case the range continues to the end member KFe_2As_2. The maximum T_c for the indirect (La)-doped system was slightly higher than that (19 K) for the direct(Co)-doped system,[6] but was lower than that (37 K) for the optimal hole-doped case.[10]

Recently, asymmetry in the electronic phase diagram upon electron and hole doping into Fe pnictide superconductors, was theoretically studied by Ikeda et al.[12] They constructed a five-band model using a combination of *ab initio* band calculations and fluctuation exchange

(FLEX) approximations, and examined the doping dependence of superconductivity. They found that superconductivity was stable over a wider range for hole doping than for electron doping. Electron doping filled the hole pockets, which in turn reduced the nesting between the hole pockets and electron pockets. The disappearance of the electron pockets did not occur by hole doping. The present experimental results on the carrier doped 122 system are consistent with this theoretical prediction.

2.4 Summary

In summary, indirectly electron-doped $Sr_{1-x}La_xFe_2As_2$ was synthesized by solid state reaction under pressures of 2-3 GPa. The optimal T_c was slightly higher than that for the indirectly electron (Co)-doped case, but much lower than that for the hole-doped case. No significant difference in the superconductivity range was observed between La- and Co-substitution. Both ranges were much narrower than that for the hole-doped case. It was concluded that the difference in electron-doping mode, either direct or indirect, was much smaller than that of polarity of the doped carrier.

References

1. (a)G. Mu, L Fang, H. Yang, X. Zhu, P. Cheng and H. H. Wen, Europhys. Lett. **82**, 17009 (2008), (b) G. Wu, H. Chen, Y. L. Xie, Y. J. Yan, T. Wu, R. H. Liu, X. F. Wang, D. F. Fang, J. J. Ying, and X. H. Chen, Phys. Rev. B **78**, 092503 (2008).
2. M. Rotter, M. Tegel, and D. Johrendt, Phys. Rev. Lett. **101**, 107006 (2008).
3. A. S. Sefat, R. Jin, M. A. McGuire, B. C. Sales, D. J. Singh, and D. Mandrus, Phys. Rev. Lett. **101**, 117004 (2008).
4. S. L. Bud’ko, N. Ni, and P. C. Canfield, Phys. Rev. B **79**, 220516(R) (2009).
5. G. Wu, R. H. Liu, H. Chen, Y. J. Yan, T. Wu, Y. L. Xie, J. J. Ying, X. F. Wang, D. F. Fang and X. H. Chen, Europhys. Lett. 84,27010 (2008)
6. A. Leithe-Jasper, W. Schnelle, C. Geibel, and H. Rosner, Phys. Rev. Lett. **101**, 207004 (2008).
7. F. Izumi and K. Momma, Solid State Phenom. **130**, 15 (2007).
8. A. C. Larson and R.B. Von Dreele, "General Structure Analysis System GSAS”, Report No.LAUR 86-748, Los Alamos National Laboratry, 158-166 (2000).
9. D.Kasinathan, A. Ormeci, K. Koch, U.Burkhardt, W. Schnelle, A. Leithe-Jasper and H. Rosner, New J. Phys. **11**, 025023 (2009).

10. B. Lv, M. Gooch, B. Lorenz, F. Chen, A. M. Guloy, and C. W. Chu, New J. Phys. **11**, 025013 (2009).
11. S. R. Saha, N. P. Butch, K. Kirshenbaum, Johnpierre Paglione and P.Y. Zavalij, Phys. Rev. Lett. **103**, 037005 (2009)
12. H. Ikeda, R. Arita, and J. Kuneš, Phys. Rev. B **81**, 054502 (2010).

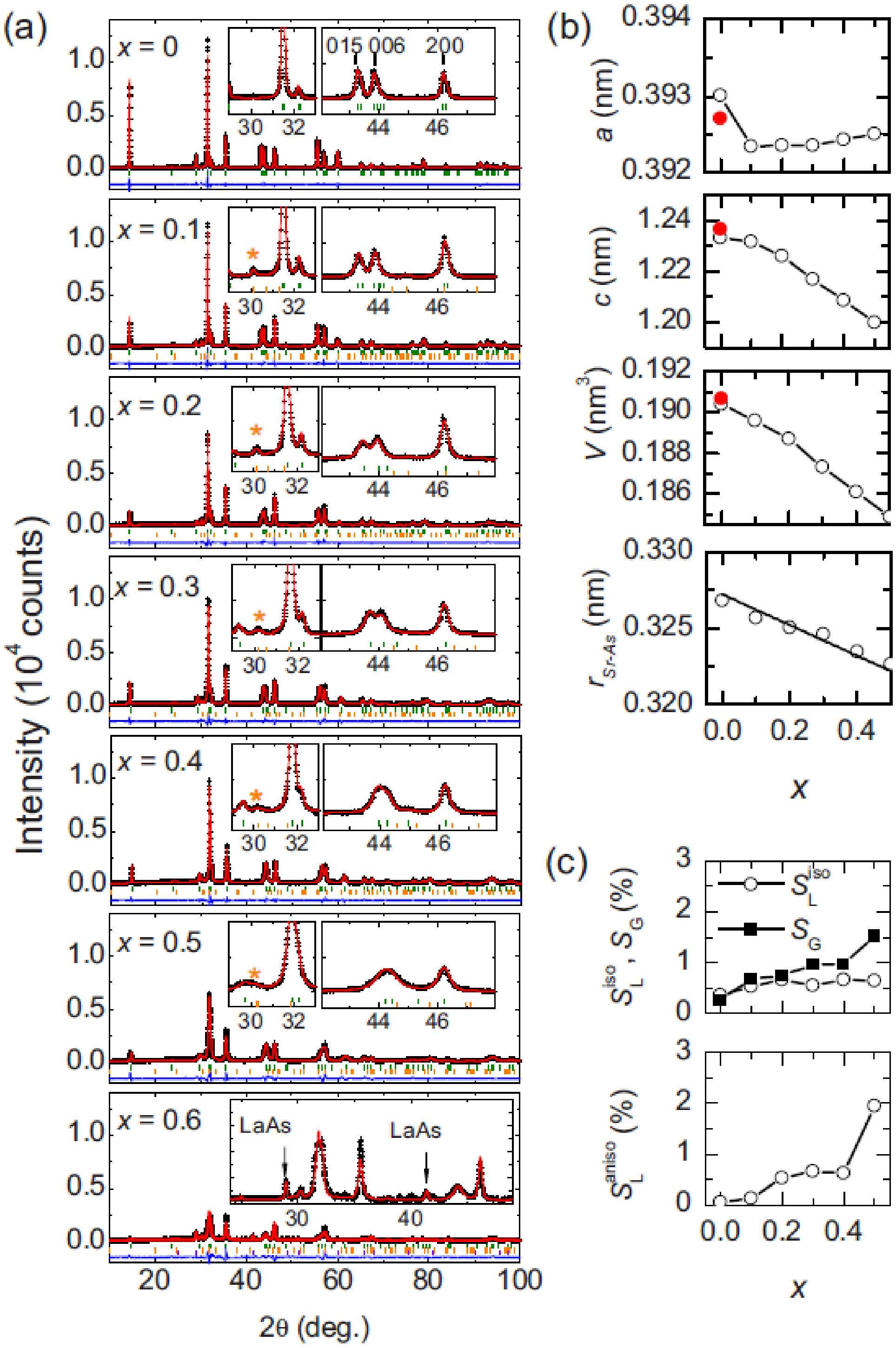

Fig.1. X-ray diffraction patterns and crystallographic data. (a) Powder X-ray diffraction (XRD) patterns of $Sr_{1-x}La_xFe_2As_2$ with x = 0.0-0.6. A small amount of LaFeAsO phase denoted by

asterisk (volume fraction ~ 3 %) almost independent of x, was seen for x = 0.1-0.5 samples. The remarkable line broadening of 00l reflections was observed upon La-substitution, indicating the presence of anisotropic strain along the c-axis. (b) Lattice constants a and c, unit cell volume V, and Sr-As distance $r_{\mathrm{Sr\text{-}As}}$ as a function of x: Data on the sample with $x = 0$ synthesized at an ambient pressure are indicated by the filled circles. (c) Crystallographic strains S_{G}, $S_{\mathrm{L}}^{\mathrm{iso}}$ and $S_{\mathrm{L}}^{\mathrm{aniso}}$ as a function of x: S_{G} and $S_{\mathrm{L}}^{\mathrm{iso}}$ are isotropic strains calculated from Lorentzian and Gaussian-type components of pseudo-Vogt function describing line broadening for Rietveld analysis. $S_{\mathrm{L}}^{\mathrm{aniso}}$ is the anisotropic strain along the [001] direction, also calculated from a Lorentzian-type component.

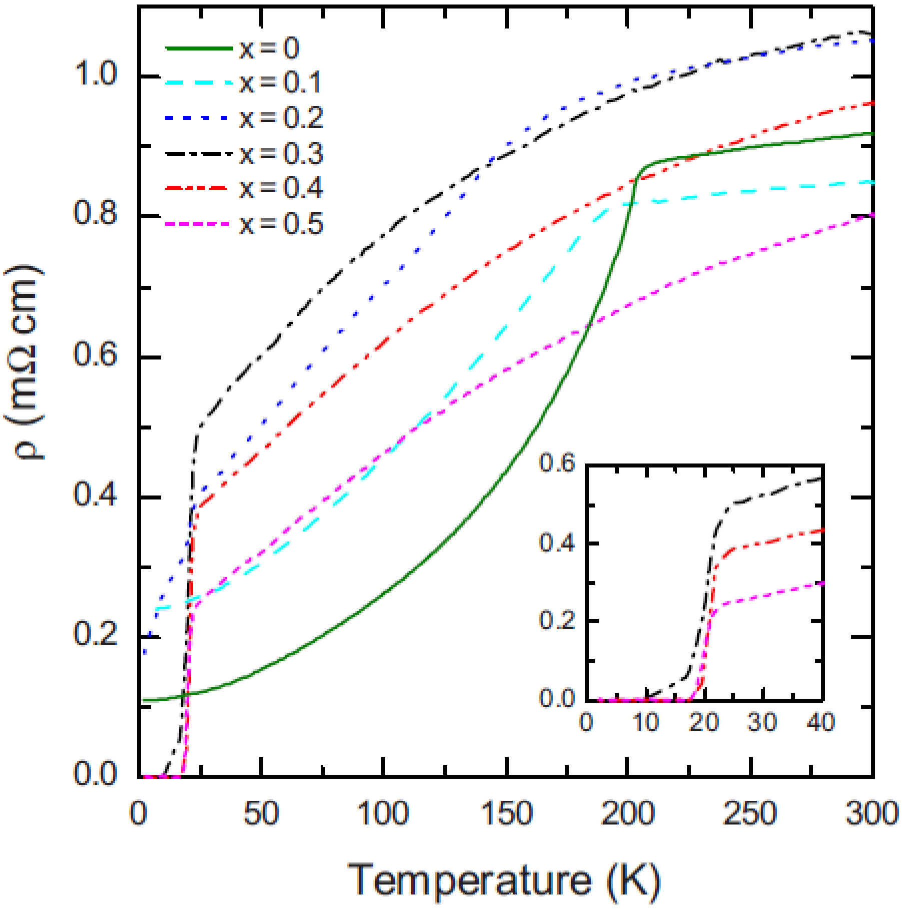

Fig.2. DC resistivity of $Sr_{1-x}La_xFe_2As_2$ as a function of temperature. The inset is the enlarged region around T_c.

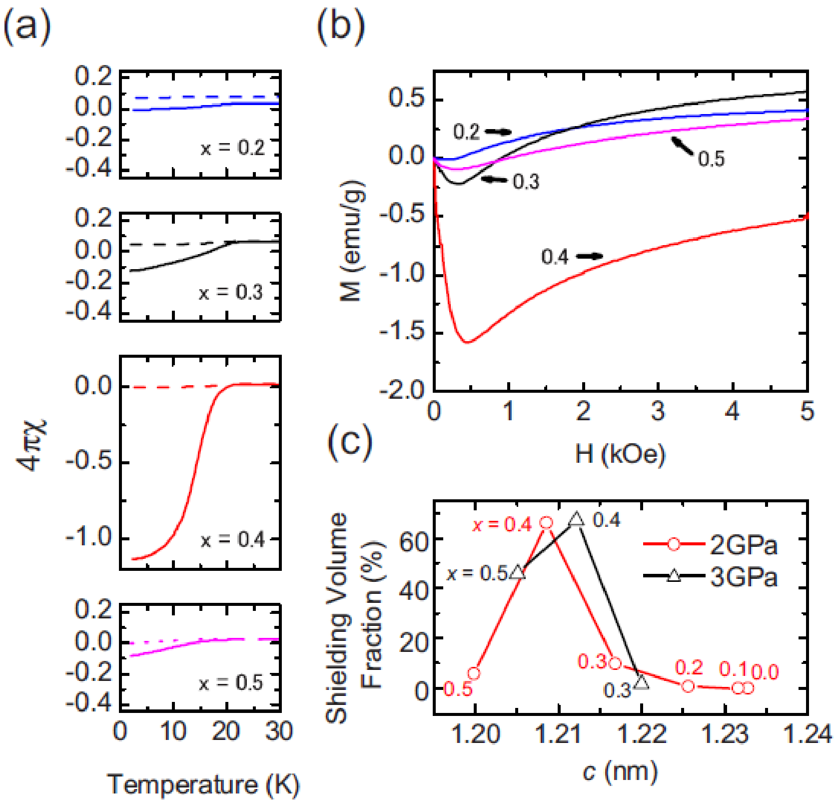

Fig.3. Magnetic properties of Sr$_{1-x}$La$_x$Fe$_2$As$_2$. (a) Temperature dependence of magnetic susceptibility χ of the samples subjected to zero field cooling (bold trace) or field cooling. (dotted trace). (b) Magnetic moment vs magnetic field at 2 K. Bottom is the shielding volume fraction evaluated from dM/dH vs lattice constants *c* of the samples prepared under pressures of 2 and 3 GPa. The shielding volume fraction trend was almost the same for both series of samples.

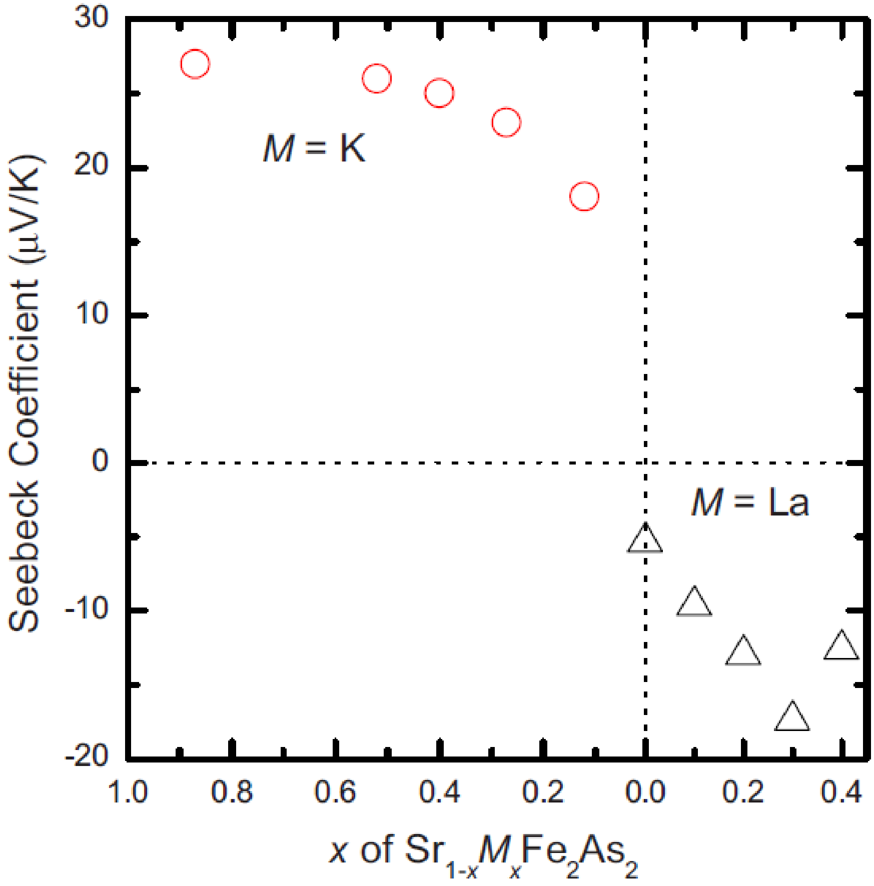

Fig.4. Seebeck coefficients at 300 K in aliovalent cation-substituted $SrFe_2As_2$. Data on the K-substituted samples were taken from ref.16.

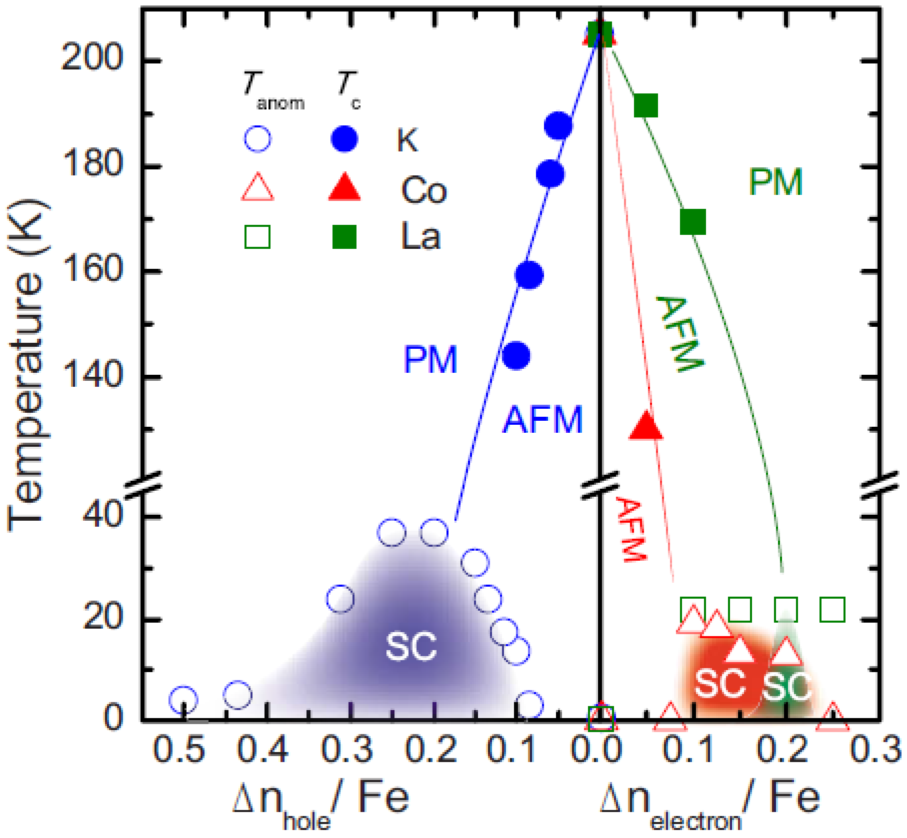

Fig.5. Electronic phase diagrams for hole/electron-doped $SrFe_2As_2$. This diagram was drawn based on the data reported in Refs. 12, 16 and present work. $\Delta n_{electron}$ /Fe is the injected number of electrons per Fe site and Δn_{hole} /Fe is the number of holes. Observed data (□) on T_c in $Sr_{1-x}La_xFe_2As_2$ is almost constant ~22 K for $\Delta n_{electron}$ /Fe = 0.1–0.25. Thus, we attribute intrinsic superconducting region to a narrow range around 0.2 on the basis of the presence of persistent crystallographic strain, shielding volume fractions, and onset T_c-x relation.

Chapter 3: 1111-type hydro arsenide CaFeAsH: a possible candidate for a parent compound of iron-based superconductors

3.1. Introduction

In preceding chapter, indirectly electron-doped $Sr_{1-x}La_xFe_2As_2$[1] were synthesized by high pressure synthesis and its T_c is comparable to that of directly electron-doped $SrFe_{2-x}Co_xAs_2$.[2] Therefore, to achieve higher T_c superconductor, indirectly electron doped 1111-type iron arsenide compound is required. *Dv*FeAsF (*Dv* = Ca, Sr, Eu)[3–5] is other 1111-type iron arsenide compound and the indirect doping to these material are expected to be a promising route to update the T_c record of iron arsenide superconductors. Although the indirect doping to *Dv*FeAsF by *Ln*-substitution to the *Dv*-site already has been reported,[6,7] a notable amount of impurity phase containing *Ln* segregation in the samples complicates any decisive evidence for Ln^{3+}–substitution to the *Dv*-site, e.g., the XRD profiles in their were unchanged with increasing *Ln*-substitution. To further extend the series of 1111-type iron arsenides, I attempted other combinations of ions which could form an insulating layer and selected H^- anion in place of F^- in CaFeAsF. Actually, some 1111-type hydrides, *LnMX*H (*M* = Mn, Fe, Co, Ru; *X* = Si, Ge)[8–14] already have been reported and these materials have been synthesized by the inserting hydrogen into *LnMX* having CeFeSi-type structure.[15] *LnMX* is transformed to *LnMX*H under heated high pressure hydrogen gas at about 600K. However this method is not adequate to the synthesis of *Dy*FeAsH, since 111-type *Dy*FeAs compounds have not been reported to exist.

In this chapter, by using a high-pressure synthesis method with an excess hydrogen source, CaFeAsH, an analog of *Ln*FeAsO, and the solid solution between CaFeAsF and CaFeAsH ($CaFeAsF_{1-x}H_x$ where $0 < x < 1$) have been synthesized. While these compounds nonsuperconducting like *Ln*FeAsO, these results indicate the anion site in the blocking layer can be substituted with H^-. Moreover, the structural transition from tetragonal (space group: *P*4/*nmm*) to orthorhombic structure (space group: *Cmma*) was confirmed by NPD analysis. DFT calculation indicates that stripe-type antiferromagnetic ordering is the most stable spin configuration and Fermi level are mainly composed of Fe-3*d* states just like *Ln*FeAsO. These results propose that CaFeAsH is a possible candidate for a parent compound of the iron arsenide superconductors.

3.2. Experimental

CaFeAsH was synthesized by the solid-state reaction of CaAs, Fe_2As, and CaH_2 with $LiAlH_4$ as an excess hydrogen source, at 1000 °C and 2 GPa ($CaAs + Fe_2As + CaH_2 \rightarrow 2CaFeAsH$). A belt-type anvil cell was employed for the high-pressure synthesis. Powders of CaAs and Fe_2As were prepared from their respective metals (Ca: 99.99% Sigma-Aldrich, Fe:

99.9% Kojyundo Chemical Laboratory Co., Ltd., and As: 99.9999% Kojyundo Chemical Laboratory Co., Ltd.) and CaH_2/CaD_2 were synthesized by heating calcium metal in an H_2/D_2 atmosphere. The solid solution of fluoride and hydride, $CaFeAsF_{1-x}H_x$, was obtained over the full x range by adding CaF_2 to the starting mixture in the high-pressure synthesis, $CaAs + Fe_2As + (1 - x)\ CaF_2 + x\ CaH_2 \rightarrow 2CaFeAsF_{1-x}H_x$. All starting materials and precursors for the synthesis were prepared in a glove box (Miwa Mfg. Co.,Ltd.) filled with purified Ar gas (H_2O, O_2 < 1 ppm). The mixture of starting materials was placed into a BN capsule. Following the internal hydrogen source technique developed by Fukai and Okuma,[16,17] $LiAlH_4$ (98%, Tokyo Kasei Kogyo Co., Ltd.) was also placed in the capsule with a BN separator as a supplementary hydrogen source. The deuterated analog, CaFeAsD, was also prepared using CaD_2 and $LiAlD_4$ (90% CP, 98% D, Tokyo Kasei Kogyo Co., Ltd.).

The resulting crystalline phases were identified by powder x-ray diffraction (XRD) using a Bruker AXS GmbH diffractometer model D8 ADVANCE (Cu-rotating anode). Rietveld analysis of XRD patterns was performed using the TOPAS code.[18] The amount of hydrogen incorporated in the resulting samples was evaluated by thermogravimetry and mass spectroscopy (TG-MS) performed using a Bruker AXS GmbH TG-DTA/MS9610 equipped with a gas feed port to inject the standard H_2 gas into the sample chamber. 20 mg of sample were heated to 800 °C with a heating rate of 20 $Kmin^{-1}$ under a helium gas flow. Hydrogen released from the sample, in the form of an H_2 molecule was ionized and was detected by a quadrupole mass spectrometer as an ion with mass-to-charge ratio (m/z) = 2.

Neutron powder diffraction (NPD) of CaFeAsD was measured on ~3 g of sample by the high-resolution powder diffractometer installed at the JRR-3 reactor of the Japan Atomic Energy Agency (beam collimation of 30’–40’-(sample)-6’ with neutron wavelength λ = 0.182391 nm). Rietveld analyses of the NPD patterns were performed using the RIETAN-FP code.[19] The dc resistivity and magnetic susceptibility were measured in the temperature range of 2–300 K, using a physical properties measurement system (Quantum Design, Inc.) with a vibrating sample magnetometer attachment. To investigate the electronic structure of CaFeAsH, density functional theory calculations were performed using the generalized gradient approximation Perdew-Burke-Ernzerhof functional[20] and the projected augmented plane wave method[21] implemented in the Vienna *ab initio* simulation program (VASP) code,[22] following Refs. 23 and 24. A $\sqrt{2}a \times \sqrt{2}b \times \sqrt{2}c$ supercell containing eight chemical formulas was used for the calculation, and the plane-wave basis set cutoff was set to 600 eV. For Brillouin-zone integrations to calculate the total energy and density of states (DOS), 4 × 4 × 2 Monkhorst-Pack grids of *k* points were used. To obtain the projected DOS, the charge density was decomposed over the atom-centered spherical harmonics with a Wigner-Seitz radius r = (3Vcell/4πN)1/3, where Vcell and N are the unit-cell volume and the number of atoms in a unit cell, respectively.

3.3. Results and discussion

3.3.1 XRD and Rietveld refinement

Figure 1 shows powder XRD patterns of the resulting products at room temperature (RT). Except for several minor peaks due to metal Fe and $Ca(OH_2)$/$Ca(OD_2)$ phases (< 5 wt%), all the peaks could be indexed to a tetragonal ZrCuSiAs-type structure(space group:*P*4/*nmm*) with lattice constants $a = 0.3878$ and $c = 0.8260$ nm for CaFeAsH and $a = 0.3876$ and $c = 0.8257$ nm for CaFeAsD (See Table I). The differences in the lattice constants between the hydride and the deuteride versions were less than 0.05%. Rietveld analysis indicates that the observed XRD pattern is well explained by assuming a model structure composed of alternate layers of FeAs and CaH (CaD). However, the site position and occupancy of hydrogen cannot be determined by XRD because the x-ray atomic scattering factor of H^-/D^- is too small.

3.3.2 TG-MS measurement

As shown in Figure 2, weight loss involving the emission of the H_2 molecule was observed from 200 °C to 600 °C. The TG-MS measurement continued to 800 °C, where the sample decomposed into a mixture of $CaFe_2As_2$, FeAs, and unknown phases probably consisting of Ca with O_2, N_2, and/or H_2O gas from the He gas flow. The amount of released H_2 was estimated to be 3.08 mmol/g from the integration of the mass peak m/z = 2. This quantity was almost equal to that expected for the decomposition of CaFeAsH ($2CaFeAsH \rightarrow Ca + CaFe_2As_2 + H_2\uparrow$, 2.91 mmol/g).

3.3.3 NPD and Rietveld refinement

Since the coherent neutron scattering cross section of deuterium (5.592 b) is comparable to that of Ca (2.78), Fe (11.22), or As (5.44),[25] the atomic position and site occupancy of deuterium can be determined by NPD. Figure 3 shows NPD patterns observed at RT and 10 K. Rietveld analyses revealed that the anion site in the block layer is occupied by deuterium, with the site occupancy of 0.935 (See Table II). Taking the isotopic purity of the LiAlD4 and the inclusion of hydrogen from other starting materials into account, we conclude that the remaining fraction (0.065) of the anion site is primarily occupied by hydrogen. The NPD pattern observed at 10 K was attributed to an orthorhombic phase, space group: *Cmma*, $a = 0.549\,213(16)$, $b = 0.545\,660(16)$, and $c = 0.821154(24)$ nm. This crystal symmetry change is the same as in other 1111-type iron arsenides with tetragonal to orthorhombic transitions reported in the range of 120-180 K. High pressure synthesis appears to be essential for the formation of CaFeAsH because no such phase could be prepared at ambient pressures.

3.3.4 Electric, magnetic and thermodynamic properties

Figure 5(a) shows the temperature dependence of dc electrical resistivity (ρ) in CaFeAsH and CaFeAsD measured from 300 to 2 K. Figure 5(b) shows temperature dependence of molar magnetic susceptibility (χ_{mol}) for CaFeAsH. With a decrease in temperature, both ρ–T and χ_{mol}–T curves exhibit sudden decreases at ~100 K. This anomaly has also been observed in 1111- and 122- type iron arsenides and has been attributed to a tetragonal to orthorhombic transition. Figure 5(c) shows the temperature–dependent heat–capacity data for CaFeAsH. Structural and magnetic transitions occur at the almost same temperature because an only one peak was shown in the *Cp*-*T* curve.

3.3.5 Electronic structure calculation

Magnetic structure was not determined by NPD analysis because magnetic moment of the Fe in CaFeAsH is small and NPD intensity was weak. To obtain a closer insight into the magnetic interaction in CaFeAsH, I performed a structural optimization procedure with structure parameter refined by NPD at 10 K as starting structure parameter and six different magnetic structures in the Fe square lattice, which include NM, FM, and two antiferromagnetic (ST and CB) configurations: (NM: nonmagnetic, nonspin-polarized calculation; FM: ferro-magnetic ordering; ST: stripe-type antiferromagnetic ordering CB: checkerboard-type antiferromagnetic ordering) Similar to 1111-type iron arsenides, the lowest total energy among the four different configurations for CaFeAsH was found for ST, in which stripe-type antiferromagnetic ordering was present. The magnetic moment calculated for each Fe ion in the ST configuration is 1.72 μ_B, which is very close to the results calculated for 1111-type iron arsenides with the same AFM configuration.[ref] From the calculated results listed in Table III, the total energie for ST is far lower than that of the other magnetic structures. These results indicate that stripe type is energetically advantageous to CaFeAsH. Moreover, optimized crystal structure for ST is orthorhombic (*Cmma*) with a small orthorhombicity [defined as (a − b)/(a + b)]. For the Fe square lattice (in tetragonal symmetry), stripe-type spin configuration is frustrated. This frustration can be removed to decrease the system energy by structural distortion thorough the shrinkage and extension of the distance between the two nearest antiparallel and parallel Fe spins, which yields the orthorhombic structure. This structural distortion has been found in parent material of iron pnictides and it is well interpreted to have a magnetic origin. Figure 6 shows the calculated total DOS and PDOS of CaFeAsH. The total energy was minimized with respect to both the coordinates of all atoms and the lattice parameters. Then, the stripe-type antiferromagnetic ordering of the Fe spins, commonly observed for 1111-type Fe arsenides below T_{anom} was obtained as the most stable magnetic structure. Total DOS and Fe PDOS profiles revealed the semimetallic nature of CaFeAsH, with Fe 3d up-spin and down-spin bands overlapped at the Fermi level (E = 0). Hydrogen 1s levels were located at ~2 eV below the Fermi level and were fully occupied. It is evident from these results that hydrogen is incorporated as H^- ($1s^2$) in CaFeAsH. This finding is consistent with the similarities in the ρ-T curves of CaFeAsH and CaFeAsF, indicating that the replacement of F sites with H^- ions does not seriously affect the electronic structure of the FeAs conduction layer. Based on the similarity of the charge and size of the hydride and fluorine ion, the formation of the solid solution $CaFeAsF_{1-x}H_x$ was expected.

3.3.6 $CaFeAsH_{1-x}F_x$

Figure 7 shows the lattice parameters *a* and *c* as a function of *x*. The value of *x* in the resulting $CaFeAsF_{1-x}H_x$ was evaluated by TG-MS measurement. While the lattice parameter *a* was almost independent of *x*, the value of *c* was proportional to *x*, indicating that the geometry of the $CaF_{1-x}H_x$ layer is determined by the weighted average of the ionic radius of F^- (r_F) and H^- (r_H). From the F-Ca distance ($r_F + r_{Ca} = 233.7$ pm) and the H-Ca bond length ($r_H + r_{Ca} = 230.2$ pm) evaluated from Rietveld analysis, the ionic radius of H^- was estimated for 1111-type iron arsenides. On the assumption that an F− coordinated by four Ca^{2+} ions retains Shannon's ionic radius ($r_F = 131$ pm),[26] then, the ionic radius of Ca^{2+} was calculated to be 102.7 pm. The radius of H^- calculated from the H-Ca bond length (230.2 pm) in CaFeAsH is 127.5 pm, which is smaller than that of F^- by 2.8%. These results indicate the existence of 1111-type hydro-arsenides and the high resemblance of hydride and fluoride ions in 1111-type iron arsenides. Furthermore, these similarities between fluorine and hydrogen in $CaFeAsH_{1-x}F_x$ propose that hydrogen could be an alternative dopant anion to induce superconductivity of *Ln*FeAsO.

3.4. Summary

The 1111-type CaFeAsH were synthesized by the high-pressure technique with an excess hydrogen source. Substitution of H^- into the F^- site in CaFeAsF and the structural transition from tetragonal (space group: *P*4/*nmm*) to orthorhombic structure (space group: *Cmma*) was confirmed by NPD analysis. DFT calculation indicates that the most stable spin configuration in CaFeAsH is stripe-type antiferromagnetic ordering. In addition, energy bands located around the Fermi level are mainly composed of Fe-3*d* states. These behaviors are observed in parent compounds of 1111- and 122-type iron arsenides. Consequently, CaFeAsH is a possible candidate for a parent compound of the iron arsenide superconductors.

References

[1] Y. Muraba, S. Matsuishi, S.-W. Kim, T. Atou, O. Fukunaga, and H. Hosono, Phys. Rev. B **82**, 180512 (2010).

[2] G. Wu, R.H. Liu, H. Chen, Y.J. Yan, T. Wu, Y.L. Xie, J.J. Ying, X.F. Wang, D.F. Fang, and X.H. Chen, EPL Europhys. Lett. **84**, 27010 (2008).

[3] S. Matsuishi, Y. Inoue, T. Nomura, H. Yanagi, M. Hirano, and H. Hosono, J. Am. Chem. Soc. **130**, 14428 (2008).

[4] S. Matsuishi, Y. Inoue, T. Nomura, M. Hirano, and H. Hosono, J. Phys. Soc. Jpn. **77**, 113709 (2008).

[5] X. Zhu, F. Han, P. Cheng, G. Mu, B. Shen, L. Fang, and H.-H. Wen, EPL Europhys. Lett. **85**, 17011 (2009).

[6] G. Wu, Y.L. Xie, H. Chen, M. Zhong, R.H. Liu, B.C. Shi, Q.J. Li, X.F. Wang, T. Wu, Y.J. Yan, J.J. Ying, and X.H. Chen, J. Phys. Condens. Matter **21**, 142203 (2009).

[7] S.V. Chong, S. Hashimoto, H. Yamaguchi, and K. Kadowaki, J. Supercond. Nov. Magn. **23**, 1479 (2010).

[8] B. Chevalier and S.F. Matar, Phys. Rev. B **70**, 174408 (2004).

[9] B. Chevalier, M. Pasturel, J.-L. Bobet, and O. Isnard, Solid State Commun. **134**, 529 (2005).

[10] J.-L. Bobet, M. Pasturel, and B. Chevalier, Intermetallics **14**, 544 (2006).

[11] B. Chevalier, S.F. Matar, J. Sanchez Marcos, and J. Rodriguez Fernandez, Phys. B Condens. Matter **378–380**, 795 (2006).

[12] B. Chevalier, E. Gaudin, S. Tencé, B. Malaman, J.R. Fernandez, G. André, and B. Coqblin, Phys. Rev. B **77**, 014414 (2008).

[13] S. Tencé, G. André, E. Gaudin, and B. Chevalier, J. Phys. Condens. Matter **20**, 255239 (2008).

[14] B. Chevalier, S. Tencé, G. André, S.F. Matar, and E. Gaudin, J. Phys. Conf. Ser. **200**, 032012 (2010).

[15] O.I. Bodak, E.I. Gladyshevskii, and P.I. Kripyakevich, J. Struct. Chem. **11**, 283 (1970).

[16] Y. Fukai and N. Okuma, Jpn. J. Appl. Phys. **32**, L1256 (1993).

[17] Y. Fukai and N. Okuma, Phys. Rev. Lett. **73**, 1640 (1994).

[18] TOPAS (Bruker AXS GmbH, Karlsruhe, Germany, 2009).

[19] F. Izumi and K. Momma, Solid State Phenomena **130**, 15 (2007).

[20] J. P. Perdew, K. Burke, and M. Ernzerhof, Phys. Rev. Lett. **77**, 3865

(1996); **78**, 1396(E) (1997).

[21] P. E. Bl¨ochl, Phys. Rev. B 50, 17953 (1994).

[22] G. Kresse and J. Furthm¨uller, Phys. Rev. B **54**, 11169 (1996).

[23] T. Nomura, S. W. Kim, Y. Kamihara, M. Hirano, P. V. Sushko, K. Kato, M. Takata, A. L. Shluger, and H. Hosono, Supercond. Sci. Technol. **21**, 125028 (2008).

[24] P. V. Sushko, A. L. Shluger, M. Hirano, and H. Hosono, Phys. Rev. B **78**, 172508 (2008).

[25] V. F. Sears, Neutron News **3**, 26 (1992).

[26] R. D. Shannon, Acta Crystallogr., Sect. A: Cryst. Phys., Diffr., Theor. Gen. Crystallogr. **32,** 751 (1976).

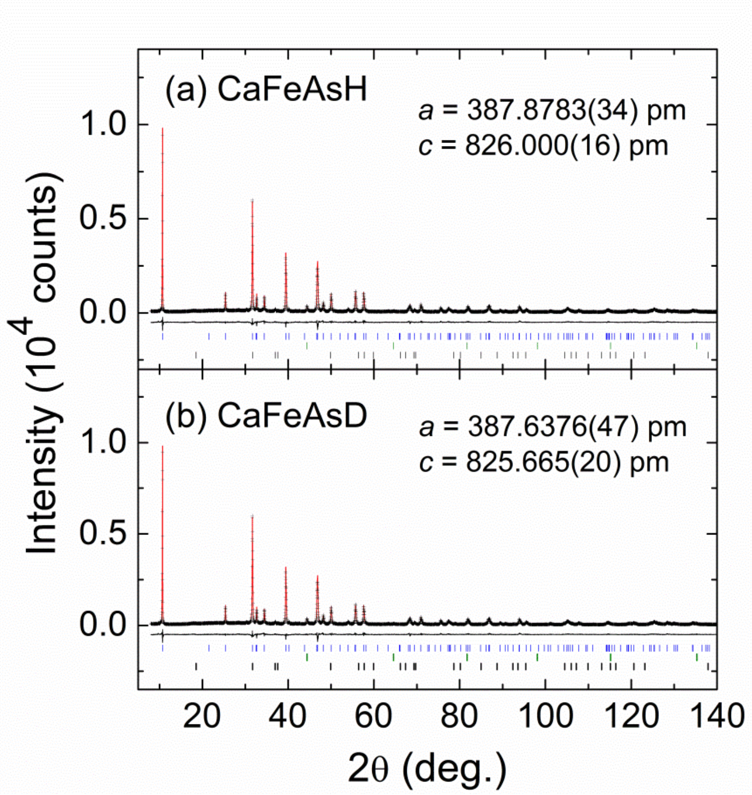

Fig.1. Powder XRD patterns of (a) CaFeAsH and (b) CaFeAsD at room temperature (RT).

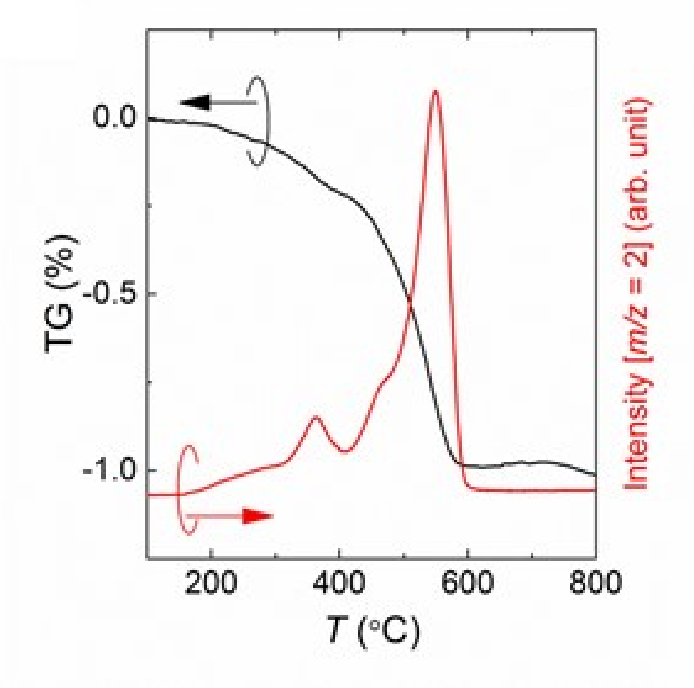

Fig. 2. TG-MS (m/z = 2 corresponds to the H_2 molecule) profiles of CaFeAsH. Weight loss due the decomposition of the sample with hydrogen emission was observed from 200 °C to 600 °C. Hydrogen concentration was estimated to be 1.05 molecules per unit cell by integration of the MS trace curve.

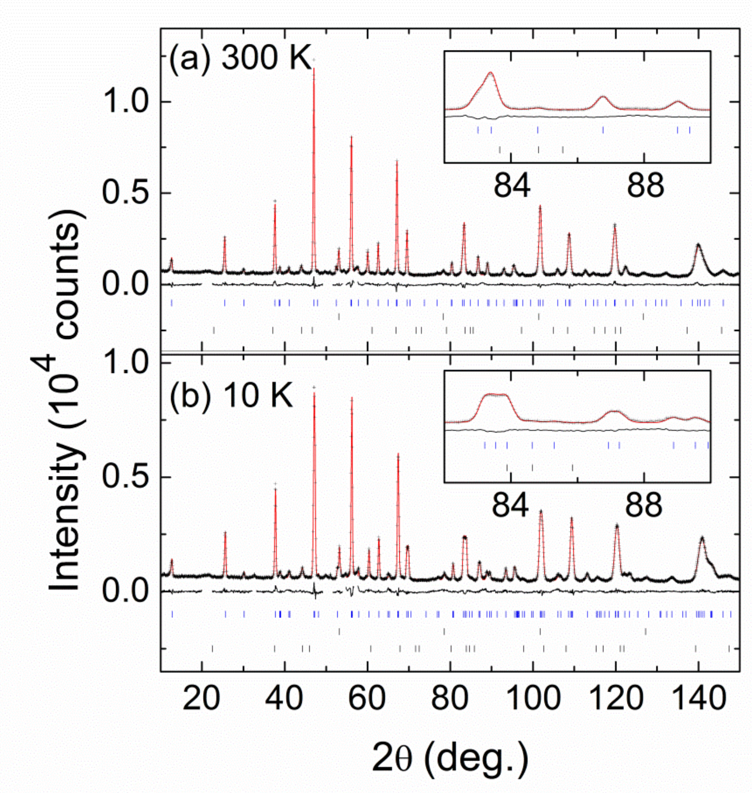

Fig. 3. NPD pattern of CaFeAsD observed at (a) 300 and (b) 10 K.

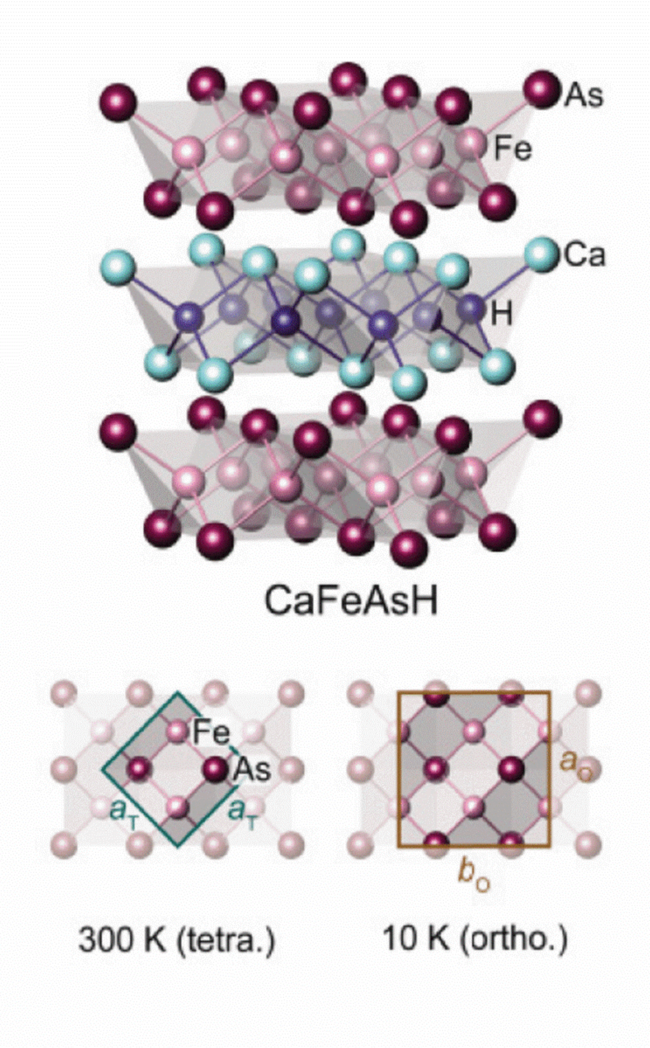

Fig. 4. Crystal structure of CaFeAsH at 300 K (tetragonal) and 10 K (orthorhombic).

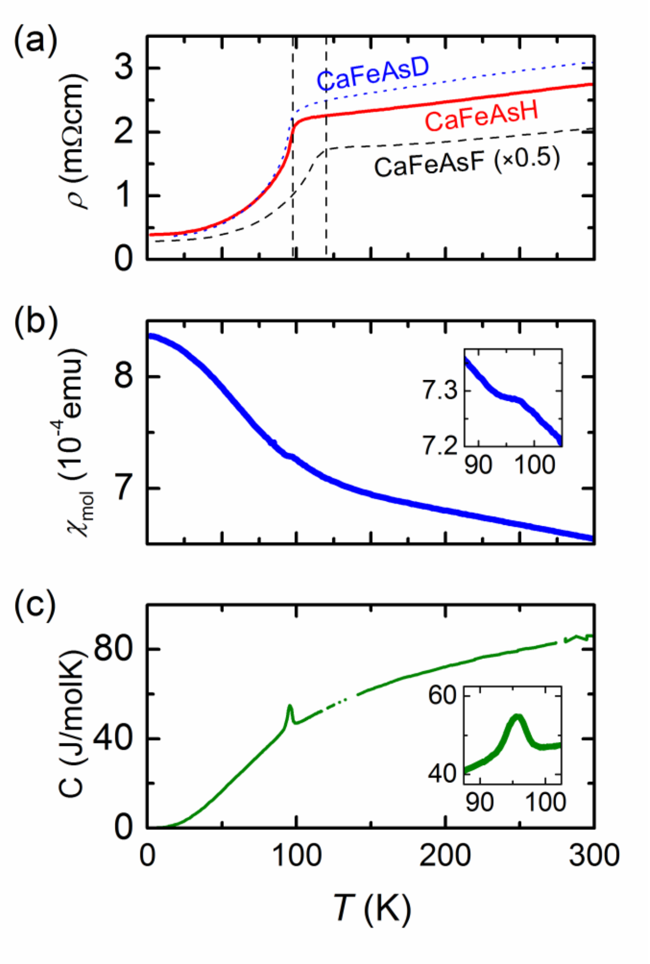

Fig. 5 (a) ρ-T profile of CaFeAsH and CaFeAsD compared with CaFeAsF. (b) Susceptibility per mol (χ_{mol}) at a fixed magnetic field of 5T as a function of temperature for CaFeAsH. (c) The measured heat capacity of CaFeAsH.

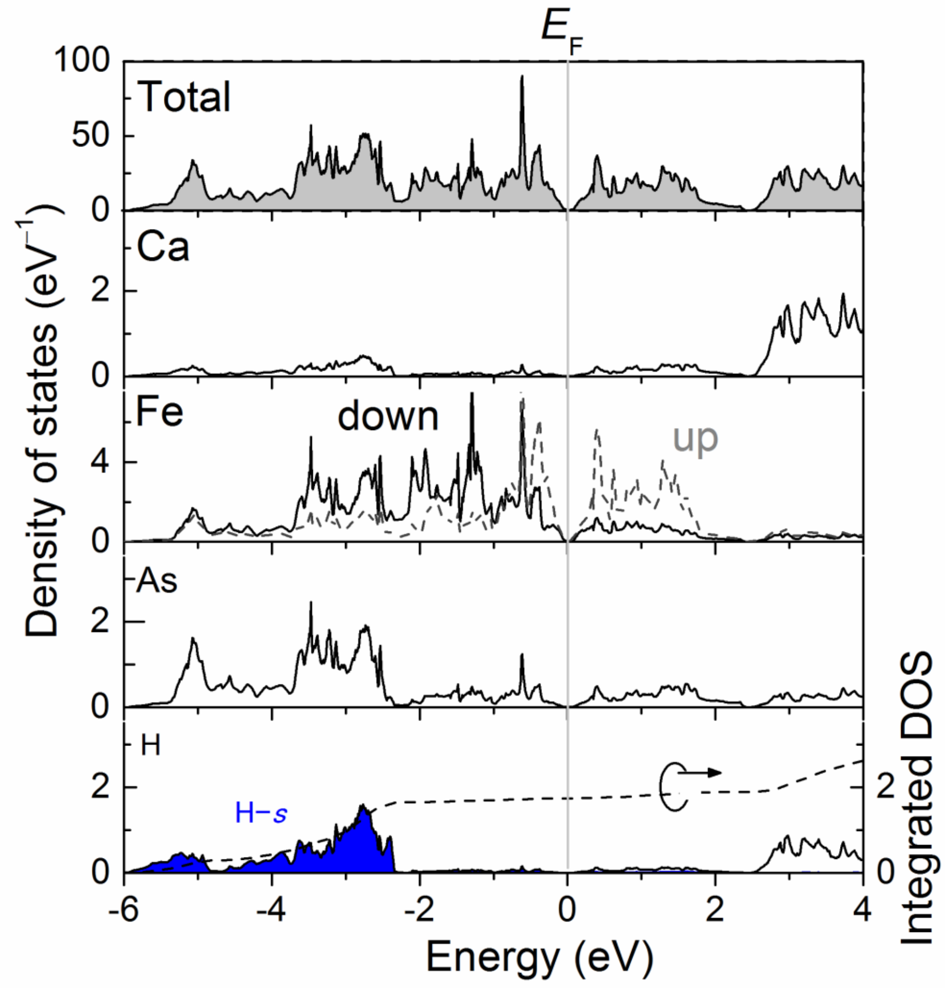

Fig. 6. Total DOS and atomic projected density of states (PDOS) of CaFeAsH obtained by density functional calculation using the VASP code. The origin was set at the Fermi level.

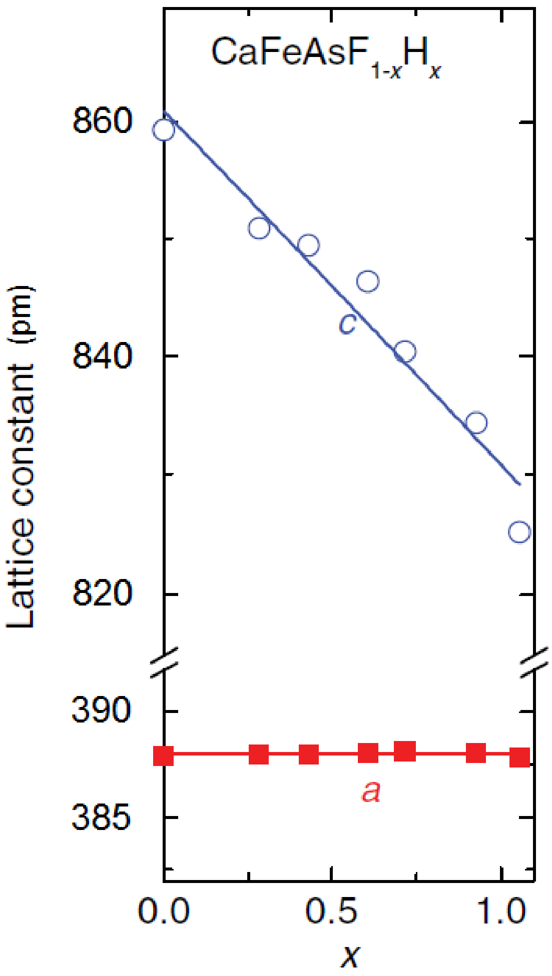

Fig. 7. Variation of lattice constants (a, c) as a function of x in the solid solution CaeAsF$_{1\text{-}x}$H$_x$. Hydrogen content (x) was estimated by the TG-MS method.

Table I. Structure parameters for CaFeAsH and CaFeAsD from XRD Rietveld refinement.

(a) CaFeAsH at RT (*P* 4/*nmm* , Z = 2)
a = 387.8783(34) pm, c = 826.0000(16) pm

Atom	Site	Occ.	*x*	*y*	*z*	*Beq* (Å^2)
Ca	2*c*	1	1/4	1/4	0.15045(24)	0.885(37)
Fe	2*b*	1	3/4	1/4	1/2	0.589(28)
As	2*c*	1	1/4	1/4	0.67114(14)	0.595(31)
H	–	–	–	–	–	–

(b) CaFeAsD at RT (*P* 4/*nmm* , Z = 2)
a = 387.5295(53) pm, c = 825.392(19) pm

Atom	Site	Occ.	*x*	*y*	*z*	*Beq* (Å^2)
Ca	2*c*	1	1/4	1/4	0.15039(35)	0.815(34)
Fe	2*b*	1	3/4	1/4	1/2	0.541(26)
As	2*c*	1	1/4	1/4	0.67190(22)	0.632(29)
D	–	–	–	–	–	–

Table II. Structure parameters for CaFeAsD from NPD Rietveld refinement.

(a) CaFeAsD at RT (*P* 4/*nmm* , Z = 2)
a = 387.629(08) pm, c = 825.494(20) pm

Atom	Site	Occ.	*x*	*y*	*z*	*Beq* (Å^2)
Ca	2*c*	1	1/4	1/4	0.14806(36)	1.102(72)
Fe	2*b*	1	3/4	1/4	1/2	0.812(37)
As	2*c*	1	1/4	1/4	0.67187(26)	0.592(40)
D	2*a*	0.9347(54)	3/4	1/4	0	1.367(64)

(b) CaFeAsD at 10 K (*Cmma* , Z = 4)
a = 387.8783(34) pm, c = 826.0000(16) pm

Atom	Site	Occ.	*x*	*y*	*z*	*Beq* (Å^2)
Ca	4*g*	1	0	1/4	0.14720(37)	0.825(71)
Fe	4*b*	1	1/4	0	1/2	0.378(40)
As	4*g*	1	0	1/4	0.67183(26)	0.159(43)
D	4*a*	0.9182(59)	1/4	0	0	1.162(72)

Table III. Optimized crystal structure for CaFeAsH with various magnetic configurations.

Magnetic structures	Z	a (pm)	b (pm)	c (pm)	α (°)	β (°)	γ (°)	Pa (%)	ΔEb (meV)	μ (μB)
NM	4	548.3	548.4	801.2	90.00	90.00	89.99	0.00	0.0	0.00
FM	4	547.8	547.9	802.5	90.00	90.00	90.00	0.01	20.3	0.09
ST	4	544.2	554.6	811.9	90.00	90.00	90.00	0.94	-264.5	1.72
CB	4	550.2	550.3	802.8	90.00	90.00	90.00	0.01	1.0	1.23

[a] *P* is orthorombicity defined as $(a - b) / (a + b)$.

[b] ΔE is total energy pew formula unit relative to nonmagnetic (NM) structure, and μ is local magnetic moment of Fe.

Chapter 4: Superconductivity of CaFe$_{1-x}$Co$_x$AsH: Enhancement of 3-dimensionality in 1111-type iron arsenide via hydrogen substitution

4.1. Introduction

In the preceding chapter, I synthesized 1111-type hydro arsenide CaFeAsH in which anion site in block layer is fully occupied by hydrogen and proposed that hydrogen could be alternative dopant anion to induce superconductivity of *Ln*FeAsO (*Ln* = Lanthanide). This hydrogen-substituted 1111-type compounds *Ln*FeAsO$_{1-x}$H$_x$ (x = 0.0–0.5) was reported by T. Hanna *et al*,[1] S. Matsuishi *et al.*[2] and S. Iimura *et al.*[3] Hydrogen is incorporated as H$^-$ at F$^-$ or O^{2-} sites, in the blocking layers of CaFeAsF or *Ln*FeAsO, respectively. The high solubility of hydrogen ($x < 0.5$) in 1111-type oxyarsenides results in a wide superconducting dome of $0.05 < x < 0.4$–0.5. The valence state and ionic radius of hydrogen are close to those of fluorine. However, their solubility toward oxygen and their pressure dependence of T_c are rather different.[4] This implies that the large spatial spread and softness of hydride electrons lead to different chemical bonding states in 1111-type iron pnictides and the fluoride-1111 material.

In this chapter, we report the superconductivity of 1111-type CaFeAsH, which is induced by Co-substitution at the Fe site. The maximum T_c = 23 K and the extent of the superconductivity (SC) region in the x-T diagram are similar to those of Co-substituted CaFeAsF. The effect of hydrogen on 1111-type iron pnictides is discussed, by comparing the electronic structures of $CaFe_{1-x}Co_xAsH$ and $CaFe_{1-x}Co_xAsF$.

4.2. Experimental

$CaFe_{1-x}Co_xAsH$ was synthesized by the solid-state reaction of CaAs, CaH_2, Fe_2As and Co_2As, using a belt-type high-pressure anvil cell. The specific reaction was:

$$CaAs + CaH_2 + (1-x)\,Fe_2As + xCo_2As \rightarrow 2CaFe_{1-x}Co_xAsH \qquad (1)$$

CaH_2, CaAs, Fe_2As and Co_2As were prepared from their respective metals. CaH_2 was synthesized by heating metallic Ca in a H_2 atmosphere. All starting materials and precursors were prepared in a glove box under a purified Ar atmosphere (H_2O and O_2 < 1 ppm). The starting material mixture was placed in a BN capsule, with a mixture of $Ca(OH)_2$ and $NaBH_4$ acting as an excess hydrogen source.[5] The mixture was heated at 1273 K under 2 GPa for 30 min. The crystal phase and structure were identified by powder X-ray diffraction (XRD), using Mo K_α radiation at room temperature. The sample was first ground into a fine powder, and placed in a glass capillary (ϕ 0.5 mm). XRD measurements were recorded in transmission mode, to reduce the effects of preferential crystallite orientation. Rietveld refinement of XRD patterns was performed using TOPAS software.[6] The chemical composition was determined by an electron-probe micro analyzer (EPMA; JEOL model JXA-8530F), equipped with a field-emission-type electron gun and wavelength dispersive X-ray detectors. Micron-scale compositions within the main phase were probed at ten individual focal points, and the results were then averaged. The temperature dependence of the DC electrical resistivity (ρ) at 2–200 K was measured using the conventional four-probe method, using Ag paste as the electrodes. Magnetization (M) measurements were recorded with a vibrating sample magnetometer (Quantum Design). Non-spin-polarized density functional theory (DFT) calculations with Perdew-Burke-Ernzerhof functional[7,8] and the projected augmented plane-wave method[9] were implemented in the Vienna *ab initio* Simulation Program (VASP) code.[10] A conventional cell containing two chemical formula units, and structural parameters obtained by the interpolation of experimental values, were used. The effect of partial Co-substitution at the Fe site was taken into account through the virtual crystal approximation. The plane-wave basis-set cutoff was 600 eV. For Brillouin-zone integrations to calculate the total energy and DOS, 20×20×10 Monkhorst-Pack grids of k points were used. The projected density of states (PDOS) was obtained by decomposing the charge density over the atom-centered spherical harmonics with the same Wigner-Seitz radius $r = (3V_{\mathrm{cell}}/4\pi N)^{1/3}$, where V_{cell} and N are the unit-cell volume and number of atoms per unit cell, respectively.

4.3. Results

4.3.1. Crystal structure

Figure 1(a) shows the powder XRD pattern of $CaFe_{1-x}Co_xAsH$, with a nominal x value (x_{nom}) of 0.07. Except for minor peaks arising from Fe metal and unknown impurities, most peaks can be indexed to a ZrCuSiAs-type structure of $P4/nmm$ symmetry, as shown inset in Fig. 1(a). Figure 1(b) shows the analyzed x value in $CaFe_{1-x}Co_xAsH$, as a function of (x_{nom}) in the starting mixture. The analyzed x value is proportional to x_{nom}, and its deviation from x_{nom} indicates the segregation of a Co-rich impurity phase. The EPMA analysis indicates the existence of an impurity of composition $CaFe_{1.85\pm0.12}Co_{1.03\pm0.11}As_{1.82\pm0.05}$, in addition to Fe metal. Figure 1(c) and (d) show variations in the $CaFe_{1-x}Co_xAsH$ lattice parameters a and c, respectively, as a function of analyzed x. These parameters for $CaFe_{1-x}Co_xAsF$ are also shown for comparison.[11] The $CaFe_{1-x}Co_xAsH$ a-axis length increases with increasing Co-substitution, whereas the c-axis length decreases. The a-axis dimensions of $CaFe_{1-x}Co_xAsH$ are comparable to those of $CaFe_{1-x}Co_xAsF$, whereas the c-axis lengths are ≈35 pm shorter than those of $CaFe_{1-x}Co_xAsF$. Figure 1(e), (f) and (g) show the As distance from the Fe plane (h_{As}), the Ca distance from the H/F plane (h_{Ca}), and the distance between the Ca and As planes ($d_{Ca\text{-}As}$), respectively. While h_{Ca} and $d_{Ca\text{-}As}$ remain largely constant, h_{As} decreases with increasing x. This indicates that the monotonic decrease of c-axis length with increasing x originates from the decrease in h_{As}. The different h_{As} (< 2 pm), h_{Ca} (≈7 pm) and $d_{\mathrm{Ca\text{-}As}}$ (≈12 pm) values of $\mathrm{CaFe}_{1-x}\mathrm{Co}_x\mathrm{AsH}$ and $\mathrm{CaFe}_{1-x}\mathrm{Co}_x\mathrm{AsF}$ are independent of Co-substitution. This also supports the conclusion that the different *c*-axis lengths originate from the decrease in $d_{\mathrm{Ca\text{-}As}}$.

4.3.2. Superconducting Properties

Figure 2(a) and (b) show the temperature dependence of the electrical resistivity (ρ) for $\mathrm{CaFe}_{1-x}\mathrm{Co}_x\mathrm{AsH}$, with $x = 0.04$–0.12 and 0.17–0.31, respectively. The anomaly in the ρ-T curves due to structural or magnetic transitions is observed at $T_{\mathrm{anom}} \approx 80$ K for $x = 0.02$. T_{anom} decreases to ≈55 K at $x = 0.04$. These samples exhibit a small ρ decrease at ≈20 K, but zero resistivity is not observed. Figure 2(c) shows the shielding volume fraction (SVF) evaluated from the gradient of the M vs. magnetic field (H) curve at 2 K. The absence of a SVF for $x = 0.02$ and 0.04 indicates that the ρ decrease of these samples arises from the local inhomogeneity of Co. As x increases ≥ 0.09, zero resistivity is attained and the onset T_{c} reaches a maximum ($T_{\mathrm{c}}^{\max}$) of 23 K at $x = 0.07$. Further Co-doping causes a monotonic decrease in T_{c}. Superconductivity is eventually suppressed at $x = 0.31$. The SVF value of >15% for samples of $0.07 \leq x \leq 0.26$ indicates bulk superconductivity. Figure 2(d) shows T_{anom} and $T_{\mathrm{c}}^{\mathrm{onset}}$ values from the ρ-T curves, as a function of x. These values for $\mathrm{CaFe}_{1-x}\mathrm{Co}_x\mathrm{AsF}$ are also shown for comparisoin.[12] T_{c}-dome values for $\mathrm{CaFe}_{1-x}\mathrm{Co}_x\mathrm{AsH}$ are in the range 0.07–0.26, with $T_{\mathrm{c}}^{\max} = 23$ K. The $T_{\mathrm{c}}^{\max}$ and the extent of the SC region are comparable to those of $CaFe_{1-x}Co_xAsF$. This implies that the superconducting properties are not significantly changed by replacing the blocking layer anion from F^- to H^-.

4.3.3. Electronic structures

Figure 3(a) compares the calculated DOS of CaFeAsF and CaFeAsH. Energy bands located around the Fermi level (E_F) are mainly composed of Fe-3*d* states. The DOS of these two compounds are comparable at $-2 < E < 2$ eV. Below the Fe-3*d* bands, the energy bands are mainly composed of As-4*p* states, which are located at $-6 < E < -2$ eV. In CaFeAsF, fluorine 2*p* states form further bands at $-7.5 < E < -5.5$ eV, without admixing with the orbitals of other atoms. On the other hand, in CaFeAsH, hydrogen 1*s* states energetically overlap well with As-4*p* states. Ca orbitals contribute at $-2 < E < -5$ eV, which suggests that they admix with the H 1*s* orbital. Figure 3(b) shows band dispersion and the contribution of Fe-3*d* orbitals. In CaFeAsF, there are three hole pockets around the Γ point, and two electron pockets around the M-point. The dispersion and orbital contribution of the electron-pockets and two of the three hole-pockets are comparable with those of CaFeAsH. However, one hole-like band in CaFeAsH crosses the E_F in the Γ-Z path, as shown by the red line in Fig. 3(b) (which corresponds to the crystallographic *c*-axis). As a consequence, the dominant orbital nature in the hole pocket changes from Fe-3*dyz/zx* in CaFeAsF, to Fe-$3d_{x^2-y^2}$ and $3d_{z^2}$ in CaFeAsH. Figure 3(c) shows the Fermi surfaces of CaFeAsH and CaFeAsF. They each have two hole pockets (denoted as α_2 and γ) and two electron pockets with the same orbital nature. The primary difference between them is the shape of the smallest hole pocket (denoted as α_1) around the Γ to Z line, which is indicated by the red line. A sandglass-shaped pocket exists in CaFeAsH, compared with a cylinder-shaped pocket in CaFeAsF. Figure 4 shows the Fermi surfaces of $CaFe_{1-x}Co_xAsH$ and $CaFe_{1-x}Co_xAsF$, with $x = 0.10$ which corresponds to the optimal electron doping level. As described in the supplementary information (Figs. S1 and S2), a rigid band model is valid for Co-substitution. That is, the band structure of $CaFe_{1-x}Co_xAs$(H, F) is similar to that of CaFeAs(H, F), with the E_F shift corresponding to the number of electron supplied from Co. The E_F shift results in the smallest hole-pockets in both systems remaining largely unchanged by Co-doping. However, two hole pockets diminish and two electron pockets slightly enlarge with increasing Co content. This robustness of the α_1 hole pocket against Co-doping is attributed to the dispersion of the band producing the α_1 hole pocket being larger than that of the electron, α_2 or γ hole pocket.

4.4. Discussion

The difference in the electronic structures of CaFeAsH and CaFeAsF is first discussed. The differences in the calculation are the structural parameters (a, c, z_{As} and z_{Ca}) and the anion species within the blocking layer (H^- or F^-). However, the band structure calculated for CaFeAsF using the structural parameters for CaFeAsH does not reproduce the Fe-3*d* band crossing the E_{F} in the Γ-Z path (Fig. S3). Therefore, the three-dimensional (3D) nature originates from the contribution of the hydrogen 1*s* state, despite it being located far from the E_{f}. Figure 3(a) shows that the hydrogen 1*s* states energetically overlap well with As 4p, and slightly overlap with the Ca components. The fluorine 2*p* states do not energetically overlap with the Ca components. This overlap results in the formation of weak covalent bonding. The covalency of energetically overlapped H 1*s* and As 4*p* states is investigated next. Figure 5(a) shows the contribution of As 4*p* and H 1*s* to the band dispersion. In CaFeAsH, hybridization of As 4*p* with the H 1*s* orbital is apparent in some parts of the bands. This indicates the presence of covalent bonding between them, despite that they are separated by 334 pm. No such covalency is observed in CaFeAsF, because each orbital contribution is distinctly separated between F 2*p* and As 4*p* states.

The effect of this covalent bonding on the Fermi surface is discussed next. The change in the band structure of CaFeAsH near the E_{F} is explained by the schematic orbital configuration shown in Fig. 5(b). The H 1*s* orbital covalently bonds with the As $4p_z$ orbital, the latter which is overlapped with the lobes of the Fe-$3d_{x^2-y^2}$ and $3d_{z^2}$ orbitals. The H 1*s* orbital weakly covalently bonds with Ca^{2+}. The As 4p orbitals mediate the inter-layer bonding of the Fe-3$d_{x^2-y^2}$ and 3d_{z^2} orbitals in adjacent FeAs layers. This results in the 3D electronic structure observed in Fig. 3(b). The dispersion of As 4p_z-derived bands along the Γ-Z direction depends on the dimensionality of the crystal structure.[12] For example, the band width along Γ-Z is ≈0 eV in $Ca_4As_2O_6Fe_2As_2$ with its thick blocking layer, while it is 0.4 and 2 eV in LaFeAsO and $BaFe_2As_2$, respectively. In $BaFe_2As_2$, the energy band with Fe-3d_{z^2} character crosses the E_F, forming the 3D hole pocket. The 3D electronic nature of $BaFe_2As_2$ is apparent from its electron transport properties.[13] In CaFeAsH, the 3D electronic nature is caused by bonding passing through the As-H-Ca bond. Covalent bonding between H and As is also reflected in the crystal structure of CaFeAsH: the shorter $d_{\mathrm{Ca\text{-}As}}$ distance in $CaFe_{1-x}Co_xAsH$ in Fig. 1(e) results from the decreased As-H separation. Electrons in the As 4p_z orbital are partly utilized in bond formation. Thus, the Fe-As bond in CaFeAsH weakens and lengthens relative to that in CaFeAsF, as shown in Fig. 1(g).

Spin fluctuations arising from the Fermi surface nesting between the hole and electron pockets are a plausible explanation for the mediation of superconductivity in iron pnictides.[14,15] The primary difference in the Fermi surfaces of CaFeAsH and CaFeAsF is the dimensionality of the α_1 hole pocket around the Γ-Z line, as indicated by red line. The former is 3D and the latter is two-dimensional (2D). Both hole pockets are smaller, and their curvatures are much larger than those of the electron pockets. This means the α_1 hole pocket does not contribute effectively to the nesting, *i.e.*, the development of spin fluctuation. The size and shape of the α_1 hole pocket remain largely unchanged up to $x = 0.1$, indicating that its contribution to superconductivity is small.

This hydrogen effect leads us to further consider its role in hydrogen-substituted *Ln*FeAsO. Hydrogen substitution effectively forms 3D Fermi surfaces, even for materials with 2D crystal structures. However, this change in Fermi surface does not affect their superconducting properties. Hydrogen is an effective dopant for electron generation via oxygen site substitution, similarly to fluorine in *Ln*FeAsO. This indicates that incorporating hydrides enhances the 3D nature of 1111-type compounds, without suppressing their superconductivity.

4.5. Summary

Superconductivity was observed in $\mathrm{CaFe_{1-x}Co_xH}$, and its properties were compared with those of $\mathrm{CaFe_{1-x}Co_xAsF}$. The maximum T_c and width of the superconducting dome of $\mathrm{CaFe_{1-x}Co_xAsH}$ are almost the same as those of $\mathrm{CaFe_{1-x}Co_xAsF}$. The calculated electronic structure of CaFeAsH differs from that of CaFeAsF. The former has a 3D hole surface, with a highly 3D nature. This is caused by covalent bonding between energetically overlapped As 4*p* and H 1*s* bands. This 3D hole surface does not interfere with superconductivity. This is because poor nesting between this small hole surface and electron surfaces causes the unfavorable development of excitations, such as spin and/or charge. Hydrogen incorporated within the blocking layer acts as an indirect electron dopant, without interfering with the superconductivity.

References

[1] T. Hanna, Y. Muraba, S. Matsuishi, N. Igawa, K. Kodama, S. Shamoto, and H. Hosono, Phys. Rev. B **84**, 024521 (2011).

[2] S. Matsuishi, T. Hanna, Y. Muraba, S.W. Kim, J.E. Kim, M. Takata, S. Shamoto, R.I. Smith, and H. Hosono, Phys. Rev. B **85**, 014514 (2012).

[3] S. Iimura, S. Matuishi, H. Sato, T. Hanna, Y. Muraba, S.W. Kim, J.E. Kim, M. Takata, and H. Hosono, Nat. Commun. **3**, 943 (2012).

[4] H.Soeda, H.Takahashi, T.Tomita, S.Matsuishi, T.Hanna, Y.Muraba, H.Hosono, in JPS Fall Meeting 2012, 29aPS-123.

[5] Y. Fukai and N. Ōkuma, Jpn. J. Appl. Phys. **32**, L1256 (1993).

[6] TOPAS, Version4.2 (Bruker AXS, Karlsruhe, Germany, (2009).

[7] J.P. Perdew, K. Burke, and M. Ernzerhof, Phys. Rev. Lett. **77**, 3865 (1996).

[8] J.P. Perdew, K. Burke, and M. Ernzerhof, Phys. Rev. Lett. 78, 1396 (1997).

[9] P.E. Blöchl, Phys. Rev. B **50**, 17953 (1994).

[10] G. Kresse and J. Furthmüller, Phys. Rev. B **54**, 11169 (1996).

[11] $CaFe_{1-x}Co_xAsF$ were prepared by solid state reaction of CaF_2, CaAs, Fe_2As and Co_2As in an evacuated silica tube at 1273K. The samples were ground into a powder and placed in a glass capillary (ϕ 0.5 mm) and XRD using Mo K_α radiation at room temperature was

measured by transmission mode. Their structure parameters were obtained by the rietveld analysis of XRD patterns.

[12] H. Usui, K. Suzuki, and K. Kuroki, Supercond. Sci. Technol. **25**, 084004 (2012).

[13] T. Katase, S. Iimura, H. Hiramatsu, T. Kamiya, and H. Hosono, Phys. Rev. B **85**, 140516 (2012).

[14] I.I. Mazin, D.J. Singh, M.D. Johannes, and M.H. Du, Phys. Rev. Lett. **101**, 057003 (2008).

[15] K. Kuroki, S. Onari, R. Arita, H. Usui, Y. Tanaka, H. Kontani, and H. Aoki, Phys. Rev. Lett. **101**, 087004 (2008).

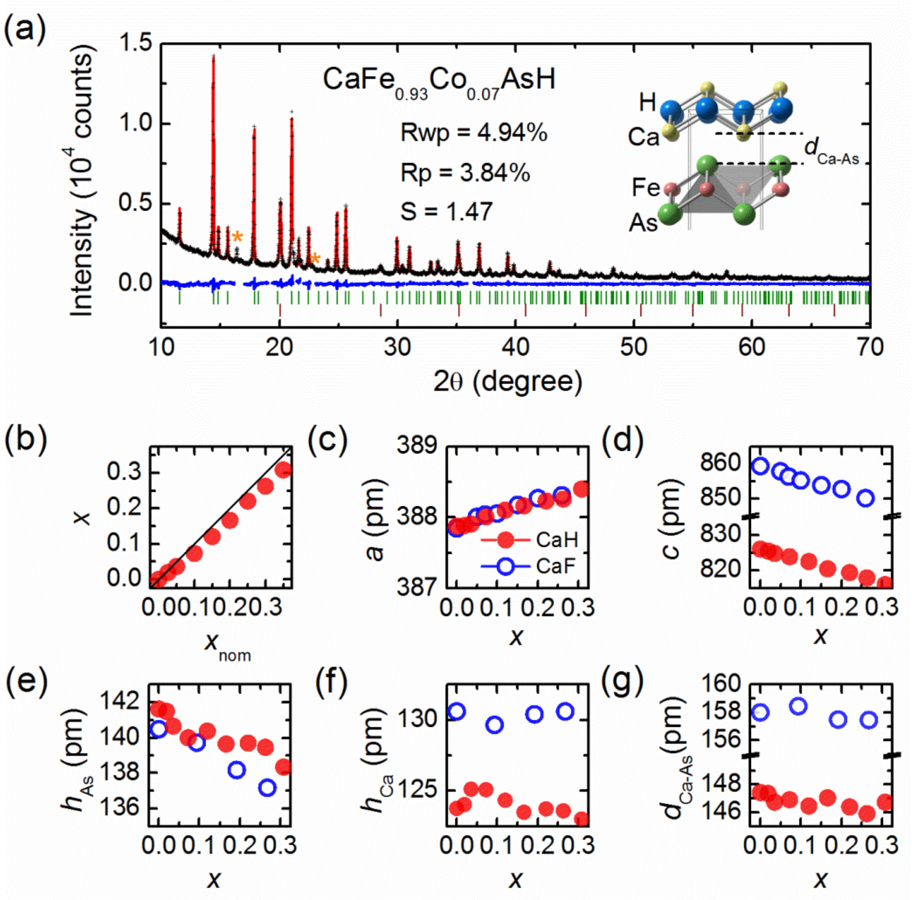

FIG. 1. Structural details of $CaFe_{1-x}Co_xAsH$. (a) Powder XRD pattern of $CaFe_{0.934}Co_{0.066}AsH$. Red and black traces indicate observed and Rietveld-fitted patterns, respectively. The differences between them (blue) and Bragg positions of the main phase (green) and Fe impurity (wine-red) are also shown. Reflections from unknown phases are denoted by orange asterisks. (b) Analyzed x content as a function of x_{nom}. (c) and (d) Lattice parameters a and c, respectively, as a function of x. (e), (f) and (g) Fe-As bond length, Ca-(H,F) bond length and distance between the FeAs and blocking layer ($d_{Ca\text{-}As}$), respectively, as a function of x.

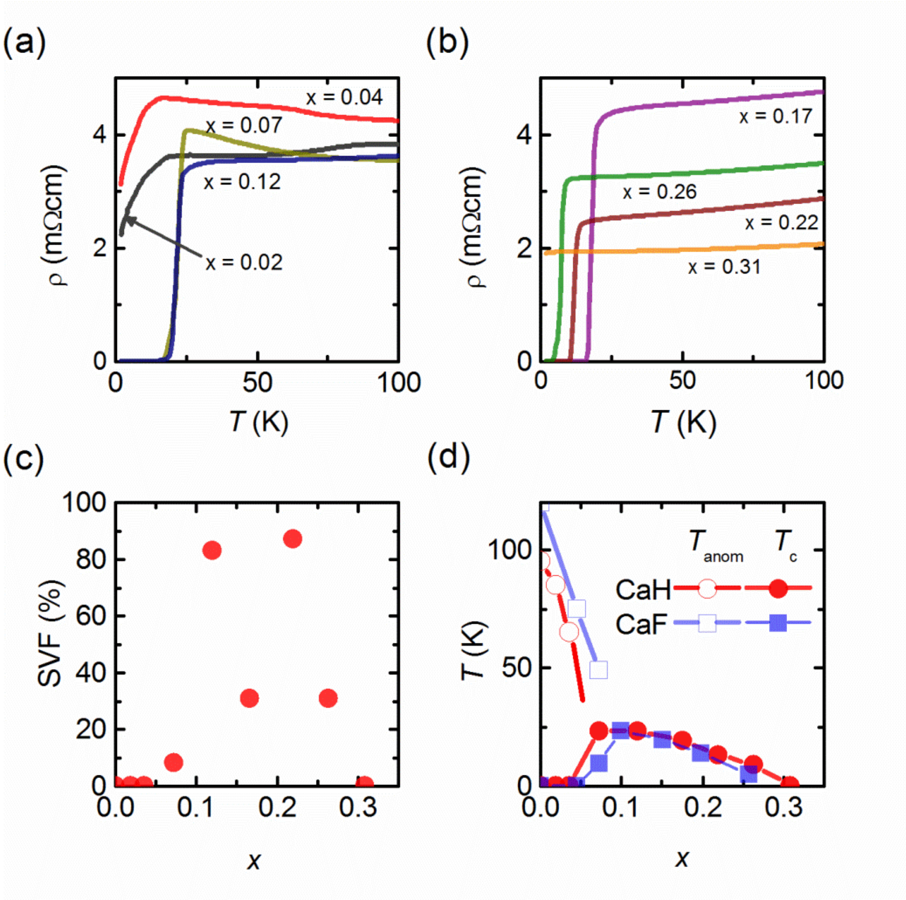

FIG. 2. Electronic and magnetic properties of CaFe$_{1-x}$Co$_x$AsH. (a) and (b) ρ-T profiles for x = 0.04–0.12 and 0.17–0.31, respectively. (c) SVF estimated from M-H curves at 2 K and 10 Oe. (d) x-T diagram of CaFe$_{1-x}$Co$_x$AsH compared with date reported for CaFe$_{1-x}$Co$_x$AsF.[28]

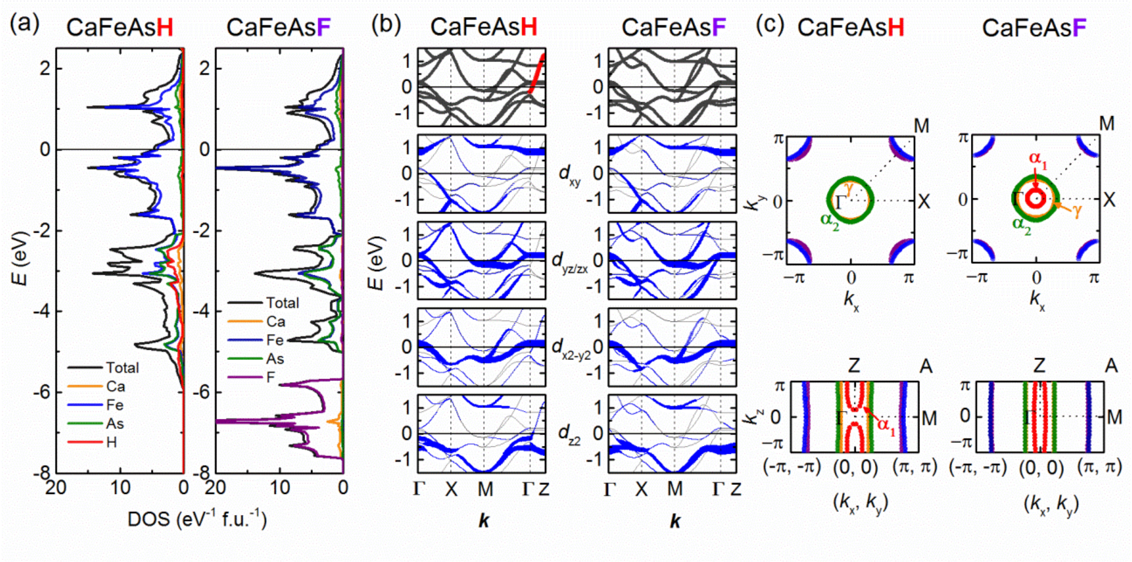

FIG. 3. Calculated electronic structures of CaFeAsH and CaFeAsF. (a) Total DOS and PDOS of CaFeAsH (left) and CaFeAsF (right). (b) Band structures along directions of high symmetry in the Brillouin zone. Thick bands (blue) show the amounts of Fe-d_{xy}, $d_{yz/zx}$, $d_{x^2-y^2}$ and d_{z^2} character. (c) Cross sections of Fermi surfaces in the $k_z = 0$ (top) and $k_x = k_y$ (bottom) planes.

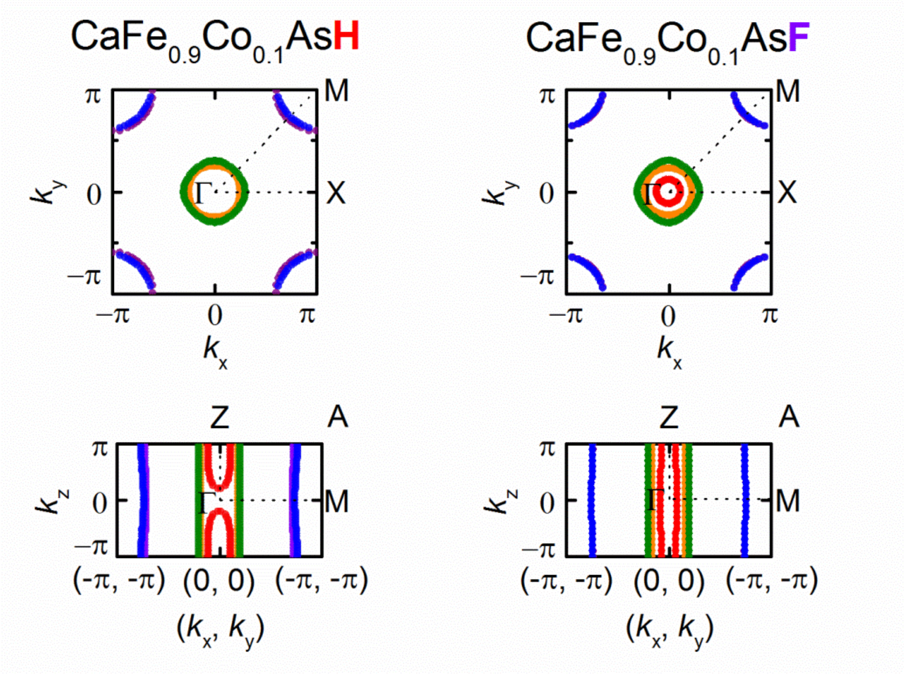

FIG. 4. Cross sections of Fermi surfaces of $CaFe_{0.9}Co_{0.1}AsH$ and $CaFe_{0.9}Co_{0.1}AsF$, in the $k_z = 0$ (top) and $k_x = k_y$ (bottom) planes.

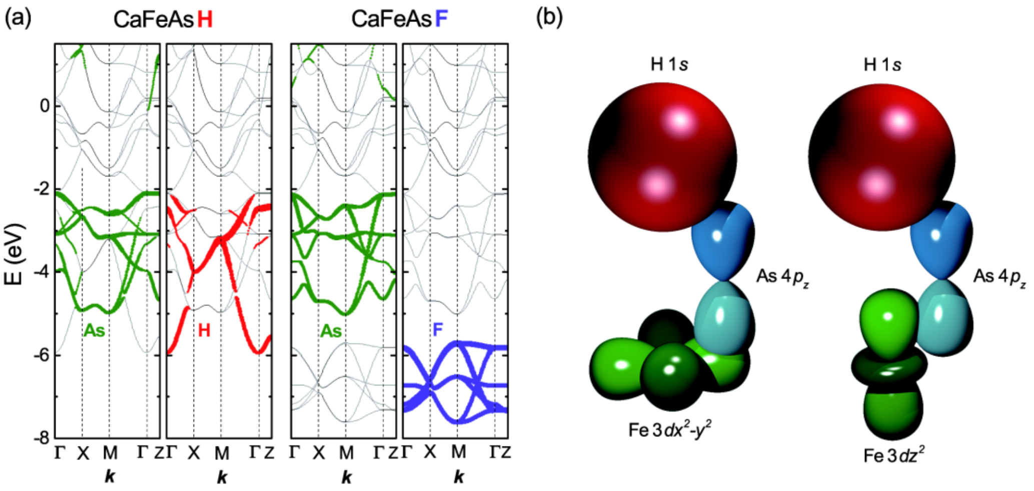

FIG. 5. Contribution of arsenic, hydrogen and fluorine atomic orbitals to the electronic structures of CaFeAsH and CaFeAsF. (a) Thickness of bands shows the amounts of As-*p* (green), H-*s* (red) and F-2*p* (purple) character. (b) and (c) Schematics showing the configurations of the H-1s, As-4*p*, Fe-3$d_{x^2-y^2}$ and -3d_{z^2} orbitals.

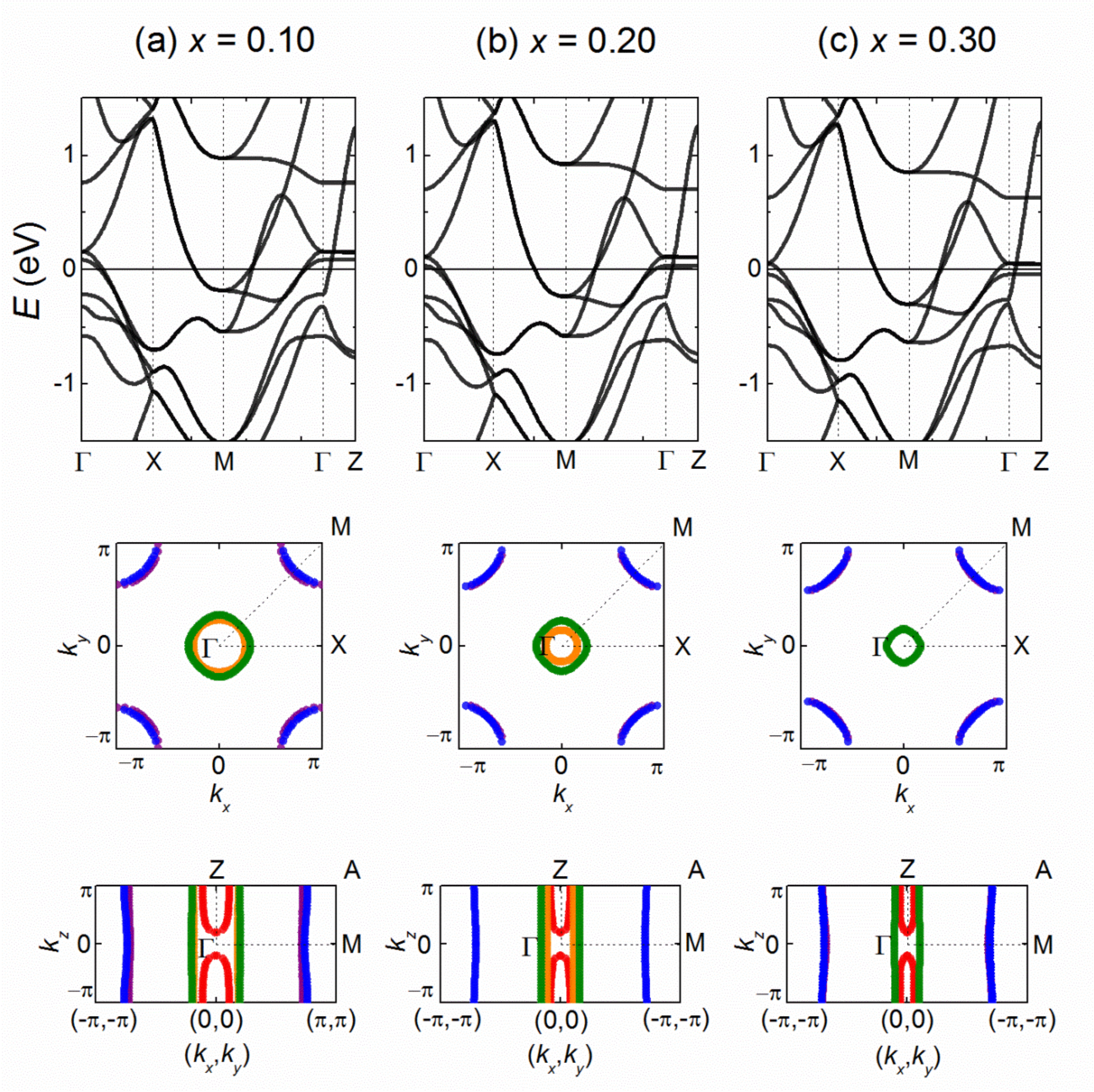

FIG. S1. Calculated electronic structure of $CaFe_{1-x}Co_xAsH$ for x = (a) 0.1, (b) 0.2 and (c) 0.3. Band structures along directions of high symmetry in the Brillouin zone (top). Cross sections of Fermi surfaces in the $k_z = 0$ (middle) and $k_x = k_y$ (bottom) planes.

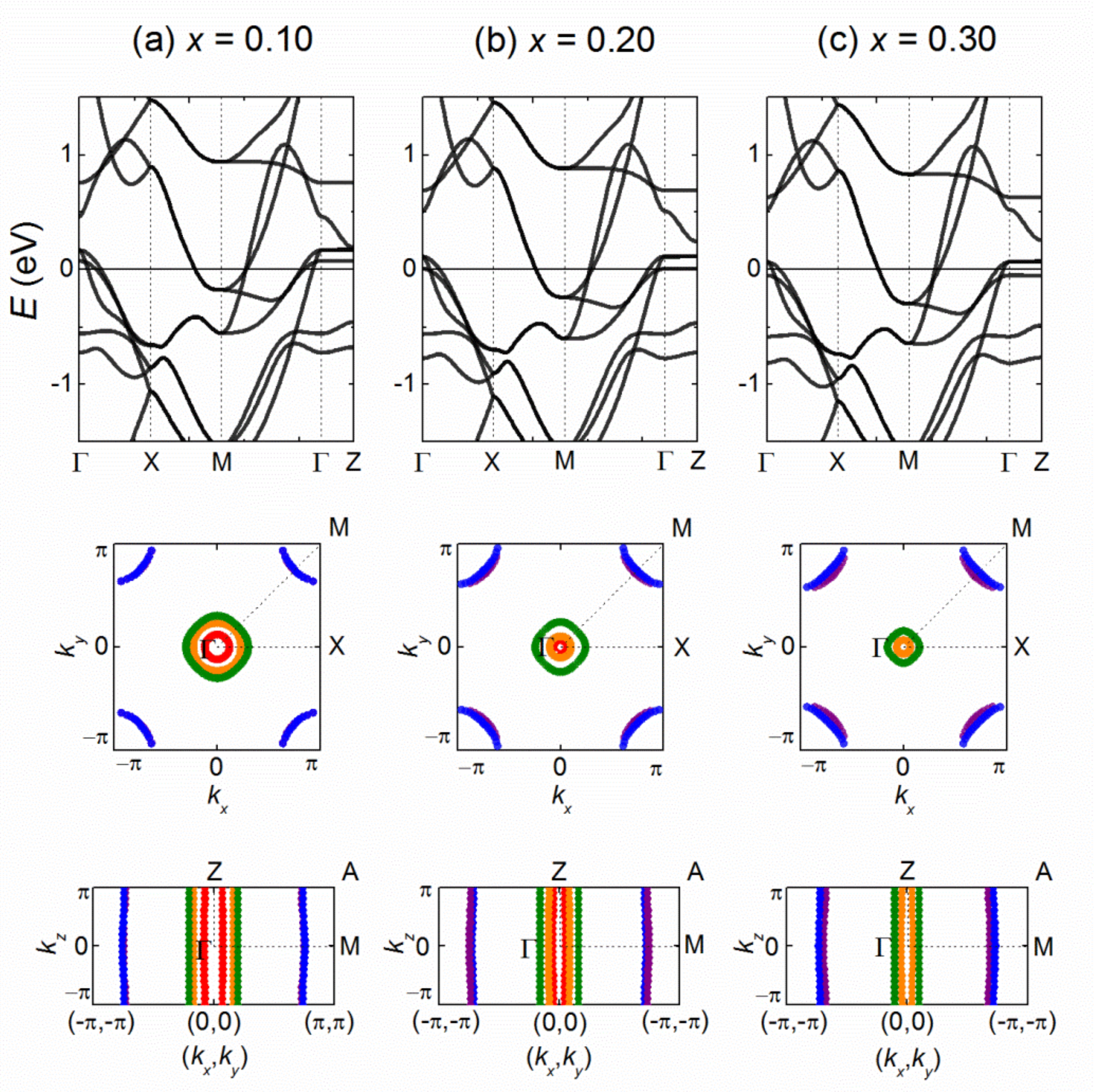

FIG. S2. Calculated electronic structure of $\mathrm{CaFe}_{1-x}\mathrm{Co}_x\mathrm{AsF}$ for x = (a) 0.1, (b) 0.2 and (c) 0.3. Band structures along directions of high symmetry in the Brillouin zone (top). Cross sections of Fermi surfaces in the $k_z = 0$ (middle) and $k_x = k_y$ (bottom) planes.

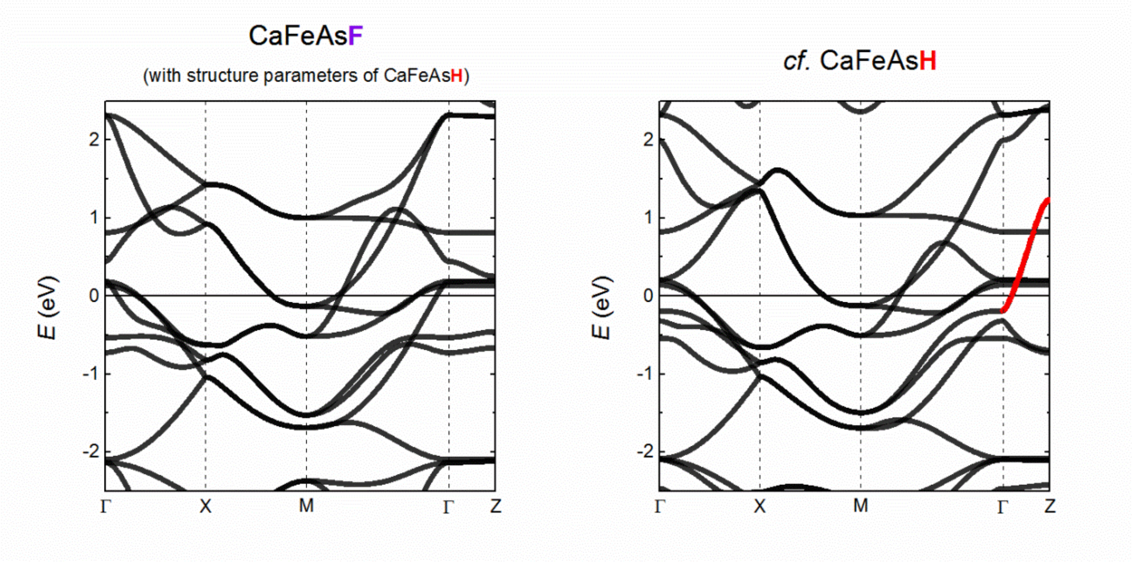

FIG. S3. Calculated band structures of CaFeAsF using the observed structural parameters (a, c, z_{As} and z_{Ca}) of CaFeAsH (left), and using those of CaFeAsH (right) for comparison. A band crossing the E_{F} in the Γ-Z direction (red line) in the right panel is not reproduced in the left panel.

Chapter 5: La-substituted hydro arsenide CaFeAsH superconductor with T_c = 47 K

5.1. Introduction

In the preceding chapter, I reported the superconductivity of directly electron-doped $CaFe_{1-x}Co_xAsH$.[1] Its T_c is comparable to that of Co-substituted CaFeAsF and these compounds exhibit the highest T_c ~ 23 K among Co-substituted 1111-type iron arsenides.[1,2] Therefore, the indirect doping to these compounds is expected to be a promising pathway to renew the T_c record of iron-based superconductors. Although the indirect doping to *Ae*FeAsF by *Ln*-substitution to the Ca-site was already reported in earlier papers,[3–5] a notable amount of impurity phase containing *Ln* segregated in the samples complicates any conclusive evidence for Ln^{3+}-substitution to the Ca^{2+} site, e.g. peak shift and change in peak intensity ratio of XRD due to *Ln*-substitution were not confirmed. However, it is reported that a large amount of H^- ion can substitute for oxygen in *Ln*FeAsO instead of F- by using high pressure synthesis.[6,7] In this chapter, I performed the indirect electron doping to 1111-type CaFeAsH by La-substitution of the Ca-site and confirmed the bulk superconductivity with maximum T_c = 47 K.

5.2. Experimental

$Ca_{1-x}La_xFeAsH$ was synthesized by the solid-state reaction of LaH_2, CaH_2 and FeAs,

$(1\text{-}x)\ CaH_2 + (1-x)\ LaH_2 + FeAs \rightarrow Ca_{1-x}La_xFeAsH + 1/2H_2\uparrow$,

using a belt-type high pressure anvil cell. CaH_2, LaH_2 and FeAs were prepared from their respective metals, and CaH_2 or LaH_2 was synthesized by heating Ca or La metal in a H_2 atmosphere. All starting materials and precursors for the synthesis were treated in a glove box filled with purified Ar gas (H_2O, $O_2 < 1$ ppm). The mixture of starting materials was placed in a BN capsule with a mixture of $Ca(OH)_2$ and $NaBH_4$ as an excess hydrogen source. This hydrogen source generates the H_2 via following reaction accompanying decomposition of $Ca(OH)_2$ to CaO and H_2O at ~573 K,

$NaBH_4 + 2Ca(OH)_2 \rightarrow NaBH_4 + 2CaO + H_2O \rightarrow NaBO_2 + 2CaO + 4H_2\uparrow$.

A BN capsule was put in a stainless capsule with a stainless cap to isolate the starting materials from an external atmosphere. The capsules were heated at 1173 K and 2.5 GPa for 30 min. The crystal structure of the resulting materials was examined by powder X-ray diffraction (XRD: Bruker D8 Advance TXS) using Cu K_α radiation with the aid of Rietveld refinement using Code TOPAS4.[8] The elemental composition except hydrogen was determined by an electron-probe micro analyzer (EPMA; JEOL Inc. model JXA-8530F) equipped with a field-emission-type electron gun and wavelength dispersive x-ray detectors. The micrometer-scale compositions within the main phase were probed on ten focal points and results were averaged. The amount of hydrogen incorporated in the samples was measured by thermal desorption spectrometry

(TDS; ESCO Inc., TDS-1000 S/W). The dc resistivity (ρ) and magnetic susceptibility (χ) were measured in the temperature range of 2 – 200 K, using a physical properties measurement system (Quantum Design Inc.) with a vibrating sample magnetometer attachment.

5.3. Results and Discussion

5.3.1 XRD and Rietveld refinement

Figure 1(a) shows XRD patterns of $Ca_{1-x}La_xFeAsH$ with nominal x (x_{nom}) = 0.1−0.4. For x_{nom} up to 0.3, major peaks were indexed as reflections from a ZrCuSiAs-type phase with *P*4/*nmm* space group. Some minor peaks were identified as reflections from BN (1.9 wt. %) and $CaFe_2As_2$ (5.1 wt. %) for x_{nom} = 0.1 and LaAs (0.5 wt. %) for x_{nom} = 0.3. The LaAs impurity content increased up to 8.5 wt. % at x_{nom} = 0.4, indicating that the solubility limit of La in CaFeAsH was $x \sim 0.4$. With increase of x_{nom}, the 012 reflection of $Ca_{1-x}La_xFeAsH$ at $2\theta \sim 30°$ was enhanced and exceeded the 001 reflection at $2\theta \sim 10°$. This observation is understood as an effect of increase in atomic scattering factor of the Ca-site, *i.e.*, La-substitution to the Ca-site. Figure 1(b) shows the lattice parameters as a function of x_{nom}. Such a lattice expansion is natural since the ionic radius of La^{3+} (116 ppm) is larger than that of Ca^{2+} (112 ppm). Rietveld refinement was performed with a structure model in which La replaces Ca sites in the 1111-type structure. The values of the temperature factors (B_{eq}) for Ca, Fe and As were fixed at those in

CaFeAsF,[9] and the values of B_{eq} for La and O were fixed at those of LaFeAsO.[10] Figure 1(c) shows the site occupancy of La^{3+} in the Ca^{2+} site as a function of x_{nom}. Those results indicate that La^{3+} occupies the Ca^{2+} site and the site occupancy is comparable to x_{nom}. Figure 1 (d) shows the As-Fe-As bond angle α as a function of x_{nom}, which slightly increased with x_{nom} to approach the regular tetrahedron angle (~109.5°).

5.3.2 Elemental analysis

Figure 2 (a) shows La concentration x analyzed by EPMA and normalized by the molar content of iron in $Ca_{1-x}La_xFeAsH$ as function of x_{nom}. The analyzed x is proportional to x_{nom} and its standard deviation increases with x_{nom}. Figure 2 (b) shows oxygen concentration analyzed by EPMA and normalized by the molar content of iron (smaller blue closed circle and line) and hydrogen concentration determined by TDS (green closed triangle and line). The oxygen concentration is 0.06 at $x = 0$ and increases up to 0.10 with x. The hydrogen concentration is 1.00 at $x = 0$ and decreases down to 0.94 with increasing x. This deviation occurs only in the 1111-type main phase because there are no impurity phases bearing hydrogen in $Ca_{1-x}La_xFeAsH$. The analysis of powder neutron diffraction pattern of CaFeAsH verified that hydrogen fully occupies the anion site in the block layer.[10] Therefore, the oxygen observed by EPMA in $x = 0$ mainly derived from surface contamination during sample preparation procedures for EPMA analysis (probed depth of EPMA operation at 10kV is ~3 μm) such as surface polishing. By assuming the amount of surface oxygen is constant among all samples, the oxygen content in the bulk was estimated by subtracting the oxygen content at $x_{\mathrm{nom}} = 0$ from the observed oxygen content (y: blue closed square and line in Fig 2(b)). The total amount of hydrogen and internal oxygen, $x + y$, is always close to unity, implying that the hydrogen site in the CaH blocking layer is partially occupied by oxygen. The oxygen in the hydrogen site should act as an electron acceptor ($\mathrm{H}^{-} = \mathrm{O}^{2-} + h^{+}$), in contrast to La^{3+} substituting the Ca^{2+} site that acts as electron donor ($\mathrm{Ca}^{2+} = \mathrm{La}^{3+} + e^{-}$). Therefore, the total number of doped electron per iron (N_e) can be expressed as $x - y$.

5.3.3. Electron transport property

Figure 3(a) shows the temperature dependence of the electrical resistivity (ρ) in $\mathrm{Ca}_{1-x}\mathrm{La}_x\mathrm{FeAsH}$ with $x = 0$, 0.08, 0.23 and 0.33. For $x = 0$, an anomaly due to the structural and the magnetic transitions was seen around ~100 K. As x is increased, the anomaly was suppressed (small kink remain around 100 K in $x = 0.08$) and zero resistivity was observed. The resistivity determined onset T_c ($T_\mathrm{c}^{\mathrm{onset}}$) remained almost constant (47.4 K) and ΔT_c were ~10 K ($x = 0.08$), 6 K ($x = 0.23$), 10 K ($x = 0.33$), respectively. The exponent n, which is obtained by fitting the data to $\rho\ (T) = \rho_0 + AT^n$ (ρ_0: residual component of resistivity) in the temperature region between T just above T_c and 95 K, decrease with increasing x. The temperature dependent electrical resistivity of the normal conducting state changed even though T_c^{onset} remains nearly unchanged with x. Non-Fermi liquid behavior ($n \sim 1$) is observed in the entire doped region. Figure 3(a) shows magnetic susceptibility ($4\pi\chi$) vs T plots of samples with x = 0.08, 0.23 and 0.33 under zero field cooled (ZFC) and field cooled (FC) with a magnetic field of 10 Oe. The diamagnetism due to superconductivity was clearly observed below T_c^{mag}, 29.8 K (x = 0.08), 41.3 K (x = 0.23) and 35.8 K (x = 0.33) and the values of $-4\pi\chi$ over 0.66 at 10 K show bulk superconductivity.

5.3.4 Electron phase diagram

Figure 4(a) summarizes the electronic phase diagram of $Ca_{1-x}La_xFeAsH_{1-y}O_y$ as function of the number of doped electron ($N_e = x - y$), superimposed by on the data of $CaFe_{1-x}Co_xAsH$.[1] The maximum T_c^{onset} of 47.4 K at N_e = 0.16 is almost double as high as that of Co-substitution (T_c = 23 K). Although T_c^{onset} remains constant with N_e, T_c^{mag} shows a dome -like structure. The difference between T_c^{onset} and T_c^{mag} indicates the inhomogeneity of N_e within the samples i.e., T_c^{onset} is dominated by domains with a maximum T_c.

Figure 4 (b) shows T_c of indirectly electron doped 1111-type iron arsenides as a function of α,[6,10–17] the so called Lee-plot.[18] The T_c increases with change in Ln from La to Sm, reaches the maximum in *Ln* = Sm or Gd (where α is near the regular tetrahedron angle of ~109.5°), and then decreases for *Ln* = Tb, Dy. The maximum superconducting transition temperature, T_c^{max} = 47 K in $Ca_{1-x}La_xFeAsH$ is comparable to that of indirectly electron doped *Ln*FeAsO. The present material falls well on the master curve of the Lee-plot, indicating that superconductivity in $Ca_{1-x}La_xFeAsH$ is caused by indirect electron doping.

Here we discuss the possibility that the superconductivity observed here was caused by $Ca_{1-x}La_xFeAs_2$ (T_c = 45 K)[19,20] or $Ca_{1-x}La_xFe_2As_2$ (T_c = 47 K)[21] which were contained as impurity phase in the $Ca_{1-x}La_xFeAsH$ because their constituent elements and T_c are similar to those of $Ca_{1-x}La_xFeAsH$. First, we consider the possibility of superconductivity derived from $Ca_{1-x}La_xFeAs_2$. The results of Rietveld analysis indicate that the $Ca_{1-x}La_xFeAs_2$ content was 0.04 wt. % or less. It is thus impossible that such a tiny amount of $Ca_{1-x}La_xFeAs_2$ yields the large values of $-4\pi\chi$ over 0.66. Next considered is the possibility of superconductivity derived from $Ca_{1-x}La_xFe_2As_2$. It is reported that $Ca_{1-x}La_xFe_2As_2$ contain two superconducting phases; the higher T_c phase (T_c = 47 K) shows filamentary superconductivity and the lower T_c (T_c = 20 K) phase does bulk superconductivity. The observed ZFC and FC curves clearly separated at over 20 K and the superconductivity observed at > 20 K (values of $-4\pi\chi$ over 0.15 at 20 K) are not filamentary. Moreover, the results of Rietveld analysis indicate that the $Ca_{1-x}La_xFe_2As_2$

content are 5.1 wt. % at $x_{\mathrm{nom}} = 0.1$, and 0.02 or less wt. % at $x_{\mathrm{nom}} = 0.2$ and 0.3. Such small fractions cannot cause the observed large values (> 0.66) of $-4\pi\chi$. Therefore, we conclude that the observed superconductivity here is not derived from $Ca_{1-x}La_xFeAs_2$ or $Ca_{1-x}La_xFe_2As_2$.

Finally we discuss the oxygen incorporated in the samples. This oxygen probably occurs in the hydrogen source during high pressure synthesis, since we dealt with the starting materials inside the glove box filled with Ar gas and used the stainless capsule to isolate the starting materials from an external atmosphere. As already mentioned in the experimental section, $Ca(OH)_2$ in the hydrogen source generates H_2O at ~573K. Although the majority of generated H_2O reacts with $NaBH_4$, a trace of H_2O can be supplied to the samples through the BN separator. The oxygen contamination raises a doubt that superconductivity was maybe caused by the $LaFeAsO_{1-x}H_x$ phase.[11] However, this possibility can be excluded by two experimental results: First, XRD demonstrates that there is no peak derived from $LaFeAsO_{1-x}H_x$. $Ca_{1-x}La_xFeAsH$ and $LaFeAsO_{1-x}H_x$ have the same crystal structure, but we can easily distinguish their peaks, since their peaks do not overlap with each other due to distinct difference in the lattice constants c between CaFeAsH (~825 pm) and LaFeAsO (~875 pm). Second, the observed maximum T_c (~47 K) is significantly higher than that of $LaFeAsO_{1-x}H_x$ (~36 K).

5.4 Summary

In summary, indirect electron-doped $Ca_{1-x}La_xFeAsH$ was synthesized by the solid state reaction at 1173K under pressure of 2.5GPa. The maximum solubility of La in CaFeAsH was $x \sim 0.3$. Rietveld analysis revealed that La substitutes the Ca sites in the CaH layers and the site occupancy of La equals almost as the nominal x. The elemental composition analysis shows that La concentration was comparable to the nominal x and a small amount of oxygen (0.02-0.05) was incorporated in the samples. An anomaly derived from a structural and a magnetic transition in the ρ-T curve is suppressed by increasing La-substitution and superconductivity was observed at $x \geq 0.08$. A maximum T_c is 47.4K at $x = 0.23$ where $4\pi\chi$ is close to -1.0. The maximum T_c (47 K) in La-substituted CaFeAsH are much higher than that (23 K) of direct electron doped $CaFe_{1-x}Co_xAsH$. This is the first iron-based 1111-type superconductor except *Ln*FeAsO in which superconductivity is induced by indirect carrier doping.

References

1. Y. Muraba, S. Matsuishi, and H. Hosono, arXiv:1312.5818.

2. S. Matsuishi, Y. Inoue, T. Nomura, H. Yanagi, M. Hirano, and H. Hosono, J. Am. Chem. Soc. **130**, 14428 (2008).

3. P. Cheng, B. Shen, G. Mu, X. Zhu, F. Han, B. Zeng, and H.-H. Wen, EPL Europhys. Lett. **85**, 67003 (2009).

4. G. Wu, Y.L. Xie, H. Chen, M. Zhong, R.H. Liu, B.C. Shi, Q.J. Li, X.F. Wang, T. Wu, Y.J. Yan, J.J. Ying, and X.H. Chen, J. Phys. Condens. Matter **21**, 142203 (2009).

5. S.V. Chong, S. Hashimoto, H. Yamaguchi, and K. Kadowaki, J. Supercond. Nov. Magn. **23**, 1479 (2010).

6. S. Matsuishi, T. Hanna, Y. Muraba, S.W. Kim, J.E. Kim, M. Takata, S. Shamoto, R.I. Smith, and H. Hosono, Phys. Rev. B **85**, 014514 (2012).

7. H. Hosono and S. Matsuishi, Curr. Opin. Solid State Mater. Sci. **17**, 49 (2013).

8. TOPAS, version 4.2 (Bruker AXS, Karlsruhe, Germany, (2009)).

9. T. Nomura, Y. Inoue, S. Matsuishi, M. Hirano, J.E. Kim, K. Kato, M. Takata, and H. Hosono, Supercond. Sci. Technol. **22**, 055016 (2009).

10. T. Hanna, Y. Muraba, S. Matsuishi, N. Igawa, K. Kodama, S. Shamoto, and H. Hosono, Phys. Rev. B **84**, 024521 (2011).

11. S. Iimura, S. Matuishi, H. Sato, T. Hanna, Y. Muraba, S.W. Kim, J.E. Kim, M. Takata, and H. Hosono, Nat. Commun. **3**, 943 (2012).

12. Z.-A. Ren, G.-C. Che, X.-L. Dong, J. Yang, W. Lu, W. Yi, X.-L. Shen, Z.-C. Li, L.-L. Sun, F. Zhou, and Z.-X. Zhao, EPL Europhys. Lett. **83**, 17002 (2008).

13. Z.A. Ren, J. Yang, W. Lu, W. Yi, G.C. Che, X.L. Dong, L.L. Sun, and Z.X. Zhao, (2013).

14. X. Wang, S.R. Ghorbani, G. Peleckis, and S. Dou, Adv. Mater. **21**, 236 (2009).

15. J. Yang, Z.-C. Li, W. Lu, W. Yi, X.-L. Shen, Z.-A. Ren, G.-C. Che, X.-L. Dong, L.-L. Sun, F. Zhou, and Z.-X. Zhao, Supercond. Sci. Technol. **21**, 082001 (2008).

16. C. Wang, L. Li, S. Chi, Z. Zhu, Z. Ren, Y. Li, Y. Wang, X. Lin, Y. Luo, S. Jiang, X. Xu, G. Cao, and Z. Xu, EPL Europhys. Lett. **83**, 67006 (2008).

17. J.-W.G. Bos, G.B.S. Penny, J.A. Rodgers, D.A. Sokolov, A.D. Huxley, and J.P. Attfield, Chem. Commun. 3634 (2008).

18. C.-H. Lee, A. Iyo, H. Eisaki, H. Kito, M.T. Fernandez-Diaz, T. Ito, K. Kihou, H. Matsuhata, M. Braden, and K. Yamada, J. Phys. Soc. Jpn. **77**, 083704 (2008).

19. N. Katayama, K. Kudo, S. Onari, T. Mizukami, K. Sugawara, Y. Sugiyama, Y. Kitahama, K. Iba, K. Fujimura, N. Nishimoto, M. Nohara, and H. Sawa: J. Phys. Soc. Jpn. **82**, 123702 (2013).

20. H. Yakita, H. Ogino, T. Okada, A. Yamamoto, K. Kishio, T. Tohei, Y. Ikuhara, Y. Gotoh, H, Fujihisa, K. Kataoka, H. Eisaki, J. Shimoyama: J. Am. Chem. Soc. **136**, 846 (2014).

21. S.R. Saha, N.P. Butch, T. Drye, J. Magill, S. Ziemak, K. Kirshenbaum, P.Y. Zavalij, J.W. Lynn, and J. Paglione: Phys. Rev. B **85**, 024525 (2012).

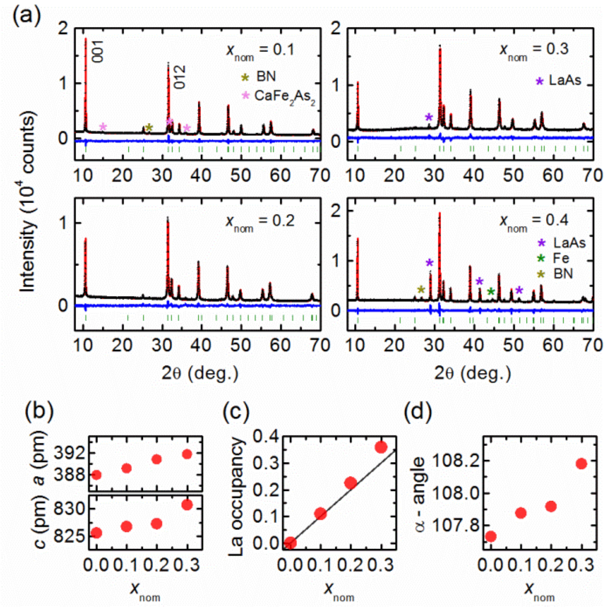

Fig.1. Crystal structure information of Ca$_{1-x}$La$_x$FeAsH. (a) Powder XRD patterns of Ca$_{1-x}$La$_x$FeAsH. nominal composition (x_{nom}) = 0.1 (top left), 0.2 (bottom left), 0.3 (top right) and 0.4 (bottom right). Red and black traces indicate observed and Rietveld-fitted patterns, respectively. The differences between them (blue) and Bragg positions of the main phase (green) are also shown. (b) Lattice parameters a (top) and c (bottom). (c) La contents obtained through Rietveld analysis. (d) As-Fe-As bond angle (α).

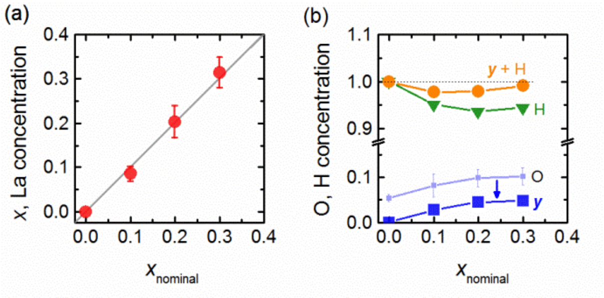

Fig.2. Composition analysis of $Ca_{1-x}La_xFeAsH$. (a) Analyzed x value of $Ca_{1-x}La_xFeAsH$ as function of x_{nom}. The value of x was determined by EPMA. (b) Oxygen concentration determined by EPMA (O : smaller blue closed square and line) and hydrogen concentration determined by TDS (H : green closed triangle and line). The oxygen concentration subtracted by that of $x = 0$ (y : larger blue closed square and line). The total of H and oxygen incorporated in the bulk (H + y : orange closed circle and line).

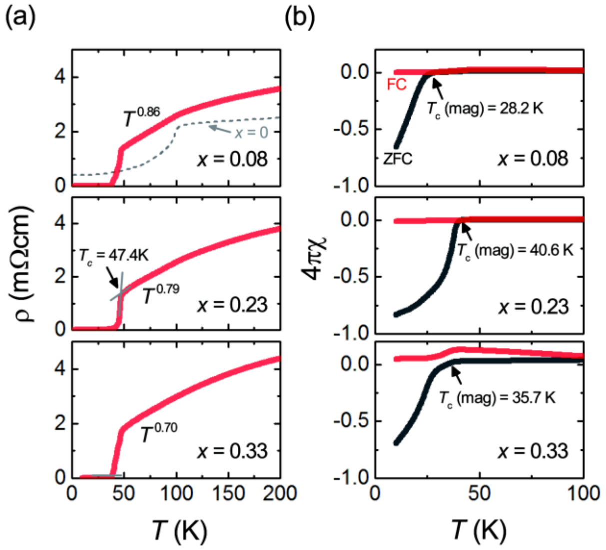

Fig.3 Electrical and magnetic properties of $Ca_{1-x}La_xFeAsH$. (a) ρ-T profiles. (b) Zero-field cooling (ZFC) and field cooling (FC) $4\pi\chi$-T curves measured under the magnetic field (H) of 10 Oe.

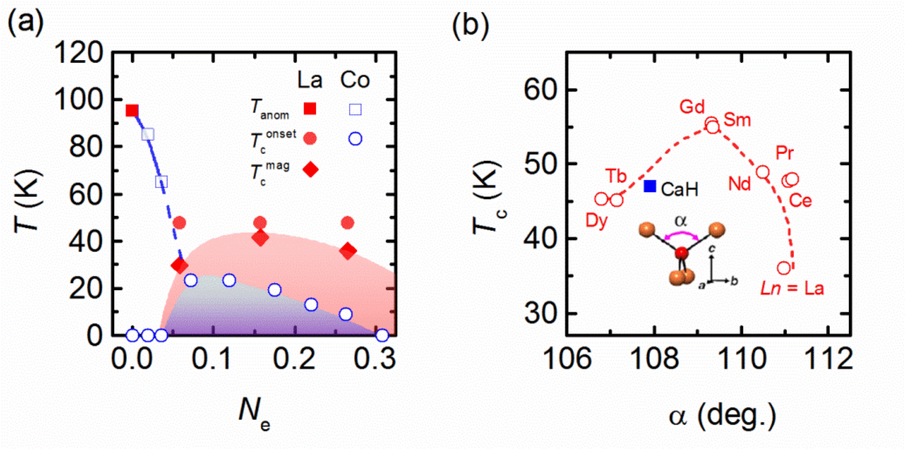

Fig.4 (a) Electronic phase diagram of $Ca_{1-x}La_xFeAsH_{1-y}O_y$ as a function of the total number of doped electron per iron ($N_e = x - y$), superimposed on that of $CaFe_{1-x}Co_xAsH$. (Ref. 23) (b) T_c vs. As-Fe-As bond angle (α). The selected T_c values and structural date are those in (Ref. 27, 31-38)

Chapter 6: General Conclusion

In this study, three new iron-based superconductors were successfully synthesized by high pressure synthesis technique and the effect of the electron-doping mode, the crystal structure and the electronic structure on superconducting properties was investigated. Indirectly electron doped $Sr_{1-x}La_xFe_2As_2$, which have not been reported due to difficulty of synthesis under ambient pressure, was successfully fabricated by high pressure synthesis. In 122–system, T_c for indirectly electron doped case (La) is comparable to that for directly electron doped case (Co). The reason for this small difference between electron doping mode, either direct or indirect is probably that even the element substitution to blocking layer provides the perturbation for conducting layer due to 3-dimensional electronic structure in 122-system. In addition, CaFeAsH in which block layer are fully occupied by H^- are successfully synthesized as new parent material for iron-based superconductor and electron doped $Ca_{1-x}La_xFeAsH$ and $CaFe_{1-x}Co_xAsH$ were synthesized by high pressure synthesis. The maximum T_c (47 K) in La-substituted CaFeAsH are two times higher than that (23 K) of direct electron doped $CaFe_{1-x}Co_xAsH$. Although CaFeAsH has the same structure as 1111-type *Ln*FeAsO and CaFeAsF with two-dimensional electronic structures, the calculated Fermi surface of CaFeAsH is a small three dimensional hole pocket due to weak covalent bonding. Considering the dimensionality of electronic structure in iron-based superconductor, in the order of $AeFe_2As_2$, CaFeAsH, and

*Ln*FeAsO (CaFeAsF), two dimensionality of electronic structure in $AeFe_2As_2$, CaFeAsH, and *Ln*FeAsO (CaFeAsF) is increased. With increasing two-dimensionality, T_c for indirectly electron doped case to that for directly electron doped case ratio become large. In other words, difference in T_c between indirectly electron doped case and directly electron doped case become larger with increasing two-dimensionality. In this study, I concluded that the difference in superconducting properties between indirectly electron doped and directly electron doped case is caused by the dimensionality of the electronic structure.

System	122	1111	
Compound	$AeFe_2As_2$	CaFeAsH	*Ln*FeAsO CaFeAsF
Fermi surface	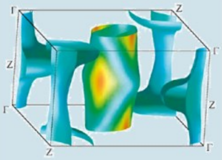 D.J.Singh *et al.* PRB (2008)	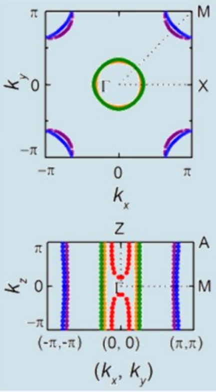	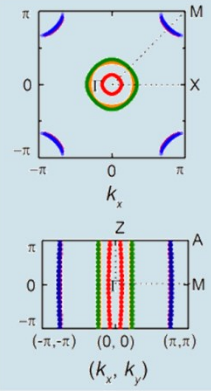
2-dimensionality	Small		Large
$T_c^{\text{indirect}} / T_c^{\text{direct}}$	0.9	2.0	3.2

The present study is summarized as follows:

Chapter 2

Compounds of $Sr_{1-x}La_xFe_2As_2$ were synthesized by solid-state reaction at 1273 K, under pressures of 2 or 3 GPa. The $Sr_{1-x}La_xFe_2As_2$ phase was dominant up to $x = 0.5$ and superconductivity was observed at $x > 0.2$. A maximum critical temperature T_c of 22 K and a maximum shielding volume fraction of ~ 70% were obtained at $x = 0.4$. This is the first experimental demonstration of electron-doped superconductivity in 122-type iron pnictides, where electrons were doped through aliovalent substitution at the site of the alkaline-earth metal. The optimal T_c was slightly higher than that for the Co-doped (directly electron-doped) samples (19 K) and much lower than that for the hole-doped case (37 K_). The bulk superconductivity range was narrower than that for the Co-substituted case and both ranges were much narrower than that for the hole-doped case. These observations revealed that differences in the electron-doping mode (direct or indirect) did not have a prominent effect on the optimal T_c or superconductivity range, compared with differences in carrier polarity.

Chapter 3

The 1111-type CaFeAsH were synthesized by the high-pressure technique with an excess hydrogen source. Substitution of H^- into the F^- site in CaFeAsF and the structural transition from tetragonal (space group: *P*4/*nmm*) to orthorhombic structure (space group: *Cmma*) was confirmed by NPD analysis. DFT calculation indicates that the most stable spin configuration in CaFeAsH is stripe-type antiferromagnetic ordering. In addition, energy bands located around the Fermi level are mainly composed of Fe-3*d* states. These behaviors are observed in parent compounds of 1111- and 122-type iron arsenides. Consequently, CaFeAsH is a possible candidate for a parent compound of the iron arsenide superconductors.

Chapter 4

The 1111-type iron arsenide hydride $CaFe_{1-x}Co_xAsH$ was synthesized by high-pressure solid-state reaction, and its electronic structure and superconducting properties were investigated. Bulk superconductivity was observed at x = 0.07–0.26. A maximum superconducting critical temperature (T_c^{max}) of 23 K was observed at x = 0.07. These values are in agreement with those of $CaFe_{1-x}Co_xAsF$. The calculated Fermi surface of CaFeAsH has a small three-dimensional (3D) hole pocket around the Γ point. This is a result of weak covalent bonding between the As 4*p* and H 1*s* orbitals. No such covalency exists in CaFeAsF, because the energy level of the F 2*p* orbital is sufficiently deep to inhibit overlap with the As 4*p* orbital. The similar superconductivities of $CaFe_{1-x}Co_xAsH$ and $CaFe_{1-x}Co_xAsF$ are explained on the nesting scenario. The small 3D hole pocket of $CaFe_{1-x}Co_xAsH$ does not significantly contribute to electron excitation. These findings encourage exploration of hydrogen-containing 1111-type iron-based materials with lower anisotropies and higher T_c applicable to superconducting wires and tapes.

Chapter 5

La-substituted CaFeAsH, $(Ca_{1-x}La_x)FeAsH$, were synthesized by the solid state reaction at 1173 K under high pressure of 2.5 GPa. The $\rho-T$ anomaly corresponding to tetragonal to orthorhombic structural transition was suppressed by La-substitution and then the superconductivity was observed at an electron doping content of $N_e > 0.05$. The maximum onset T_c of 47.4 K was reached for $N_e = 0.18$, which is significant increase compared to 23 K achieved by direct electron doping to the FeAs-layer via Co-substitution to the Fe-site. This value of T_c value fits well to the phenomenological relation between T_c and the bond angle of As-Fe-As in indirectly electron doped *Ln*FeAsO (*Ln* = Lanthanide). These results indicate that the electron was doped via the indirect mode through the aliovalent ion substitution to CaH-layer ($Ca^{2+} \rightarrow La^{3+} + e^{-}$).

Acknowledgements

This study was carried out in Hosono, Kamiya & Hiramatsu Laboratory at the Tokyo Institute of Technology from April 2008 to March 2014. Numerous people have contributed to this study.

First of all, I would like to express gratitude from bottom of my heart to Prof. ***Hideo Hosono*** for his advice and continuous encouragement. Also, I would like to express my sincere thanks to Prof. ***Toshio Kamiya***, Associate Prof. ***Hidenori Hiramatsu***, Associate Prof. ***Hiroshi Yanagi*** (currently at Yamanashi university), Associate Prof. ***Satoru Matsuishi***, Associate Prof. ***Sung-Wng Kim*** (currently at Sungkyunkuwan university), and Assistant Prof. ***Soshi Iimura*** for their kind guidance, discussions, and important suggestions.

I learned a lot from them such as a sense of materials research. I wish to express my gratitude to Prof. ***Tomofumi Susaki***, Associate Prof. ***Toshiyuki Atou*** for their critical reading of this thesis and for their useful comments regarding this study.

I am deeply grateful to honorary Professor ***Osamu Fukunaga*** for active collaboration with belt-type high pressure apparatus and fruitful discussions.

I am also much indebted to Funding Program for World-Leading Innovative R&D on Science and Technology (FIRST) project members including Prof. ***Satoru Fujitsu***, Associate Prof. ***Hiroshi Mizoguchi***, Assistant Prof. ***Yoshitake Toda***, Assistant Prof. ***Fuji Funabiki***, Dr.

Naoki Imamura, Dr. ***Kimoon Lee*** (currently at *Samsung Electronics Co., Ltd*), Dr. ***Fumitaka Hayashi***, Dr. ***Jiangang Guo***, Dr. ***Yanpeng Qi***, Dr. ***Lei Hechang***, Mr. ***Yuji Kondo***, and Mr. ***Shizuo Hayashi***, for their kind supports and suggestions.

I wish to express my gratitude to researchers on Fe-based superconductors, Dr. ***Takatoshi Nomura*** (currently at *Denso Co.*), Assistant Prof. ***Takayoshi Katase*** (currently at *Hokaido* university), Dr. ***Gifun Ryu*** (currently at *Max Planck Institute*), Dr. ***Taku Hanna*** (currently at), Mr. ***Yasunori Inoue*** (currently at), Ms. ***Saki Matsuo*** (currently at *Fujitsu Co.*), Mr. ***Ryo Date*** (currently at), Mr.***Toshinori Kuroda*** (currently at *Sumitomo Chemical.*), Mr. ***Atsushi Nakamura*** (currently at *Taiheiyou cement corp.*), Mr. ***Takuya Maruyama***, Mr. ***Sang Won Park***, Mr. ***Yoshiyasu Sato*** and Mr. ***Takashi Muramoto*** for their fruitful information exchanges and kind experimental supports.

I also would like to thank Mr. ***Sehoon Jeong***, Mr. ***JoonHo Bang***, Mr. ***Yudai Tomota***, Mr. ***Shogo Matsuda***, Ms. ***Yue Wang***, Mr. ***Jun-ichi Ishida***, Ms. ***Yukiko Obata***, Mr. ***He Yingdi***, Mr. ***Toshihiro Kobayashi*** and other members of the S2 bldg. for meaningful discussions.

In addition, I would like to acknowledge Secretaries Ms., Ms. ***Kanako Ochiai***, Ms. ***Mayumi Nakano***, and Ms. ***Hanae Murayama***.

Finally, I express appreciation to my family and friends.

March 2014

Yoshinori Muraba

Publication List

Papers included in the thesis

1. "High-pressure synthesis of the indirectly electron-doped iron pnictide superconductor $Sr_{1-x}La_xFe_2As_2$ with maximum T_c = 22 K"
   Yoshinori Muraba, Satoru Matsuishi, Sung-Wng Kim, Toshiyuki Atou, Osamu Fukunaga, and Hideo Hosono,
   Phys. Rev. B **82**, 180512(R) (2010).

2. "Enhancing the three-dimensional electronic structure in 1111-type iron arsenide superconductors by H-substitution"
   Yoshinori Muraba, Satoru Matsuishi, and Hideo Hosono,
   Phys. Rev. B (accepted).

3. "La-substituted CaFeAsH superconductor with 47 K"
   Yoshinori Muraba, Satoru Matsuishi, and Hideo Hosono,
   J. Phys. Soc. Jpn (accepted).

Other papers

1. "Hydrogen in layered iron arsenides: Indirect electron doping to induce superconductivity"
   Taku Hanna, **Yoshinori Muraba**, Satoru Matsuishi, Naoki Igawa, Katsuaki Kodama, Shin-ichi Shamoto, and Hideo Hosono,
   Phys. Rev. B ***84***, 024521 (2011)

2. "Structural analysis and superconductivity of $CeFeAsO_{1-x}H_x$"
   Satoru Matsuishi, Taku Hanna, **Yoshinori Muraba**, Jung-Eun Kim, Masaki Takata, Shin-ich Shamoto, Ronald I. Smith, and Hideo Hosono,
   Phys. Rev. B ***85***, 014514 (2012).

3. "Two-dome structure in electron-doped iron arsenide superconductors"
   Soshi Iimura, Satoru Matuishi, Hikaru Sato, Taku Hanna, **Yoshinori Muraba**, Sung-Wng Kim, Jung-Eun Kim, Masaki Takata, and Hideo Hosono,
   Nat. Commun. **3**, 943 (2012).

4. "Hydrogen substitution effect on the superconductivity of *Ln*NiAsO (*Ln* = La-Nd)"
   Satoru Matsuishi, Atsushi Nakamura, **Yoshinori Muraba**, and Hideo Hosono,
   Supercond. Sci. Technol. **25**, 084017, (2012)

5. “Superconductivity in 1111-type $CaFeAsF_{1-x}H_x$ induced by selective hydrogen elimination”
   Taku Hanna, **Yoshinori Muraba**, Satoru Matsuishi, and Hideo Hosono,
   Appl. Phys. Lett. **103**, 142601, (2013)

Presentation List

International presentations

1. “High Pressure Synthesis of Indirectly electron-doped 122 Iron Superconductor $Sr_{1-x}La_xFe_2As_2$with a maximum T_c = 22 K” (Poster)
   Y.Muraba, S.Matsuishi, H.Hideo
   23rd International Symposium On Superconductivity (ISS2010), Tsukuba, Japan, Norbember 1-3, 2010.

2. “Comparison electronic structure and properties between hydrogen and fluorine substituted1111-type iron pnictide superconductors” (Poster)
   Y.Muraba, S.Matsuishi, H.Hideo
   Novel Superconductors and Super Materials 2013 ($NS^2$2013), Shinagawa, Japan, November 21-22, 2013.

Domestic Presentations

1. “層状化合物 $SrFe_2As_2$ の Sr サイト La 置換による超伝導” (ポスター)
   村場善行, 松石聡, 金聖雄, 阿藤敏行, 福長脩, 細野秀雄
   特定領域研究「配列ナノ空間を利用した新物質科学ユビキタス元素戦略」第 3 回若手研究会 (2010/8/31-9/1, 山形)

2. **“$CaFe_{1-x}Co_xAsH$ の電子構造と超伝導”**
   村場善行, 松石聡, 細野秀雄
   日本物理学会 2013 年秋季大会 徳島大学 (2013/9/25-28, 徳島)

3. “$Ca_{1-x}La_xFeAsH$ の超伝導”
   村場善行, 松石聡, 細野秀雄
   日本高圧力学会 第 54 回高圧討論会 新潟コンベンションセンター(2013/11/14-16)

4. “Superconductivity of Cobalt-doped CaFeAsH: Enhancement of 3-dimensinality in 1111-type iron arsenide via hydrogen substitution” (ポスター)
   村場善行, 松石聡, 細野秀雄
   The Workshop on Education and Research Center for Materials Innovation (2014/02/06, 東京工業大学)